Neutron stars as gravitational wave emitters and detectors

By

BORIS GONCHAROV

School of Physics and Astronomy
MONASH UNIVERSITY

A dissertation submitted to MONASH UNIVERSITY in accordance with the requirements of the degree of DOCTOR OF PHILOSOPHY in the FACULTY OF SCIENCE.

JUNE 2020

Advisors:
Prof. Eric Thrane
Dr. Xing-Jiang Zhu

COPYRIGHT NOTICE

This thesis must be used only under the normal conditions of "fair dealing" under the Copyright Act. It should not be copied or closely paraphrased in whole or in part without the written consent of the author. Proper written acknowledgement should be made for any assistance obtained from this thesis. I certify that I have made all reasonable efforts to secure copyright permissions for third-party content included in this thesis and have not knowingly added copyright content to my work without the owner's permission.

© Boris Goncharov (2020)

Abstract

Neutron stars are the most dense astrophysical objects where electromagnetic radiation from the surface can still reach a remote observer. It makes them unique astrophysical laboratories that provide means to study nuclear matter under extreme conditions. Rapid rotation and strong magnetic fields make some neutron stars to appear as pulsars, beacons of electromagnetic radiation visible in our Galaxy. In fact, the most rapidly rotating pulsars reach periods of a few milliseconds and become promising tools to search for nanohertz-frequency gravitational waves, perturbations of space-time propagating at the speed of light, emitted by supermassive black hole binaries in the universe. Experiments that perform long-term monitoring of pulse arrival times from millisecond pulsars are called pulsar timing arrays. On time scales on the order of years to decades, spin period of millisecond pulsars fluctuates, introducing the so-called spin noise in pulsar timing experiments. While limiting the sensitivity of pulsar timing arrays to the gravitational-wave background, spin noise provides an opportunity to probe neutron star physics. Additionally, at some level, neutron stars are predicted to deform themselves into a spherically-asymmetric shape. This will inevitably make neutron stars sources of gravitational waves on their own. These gravitational waves, searched for with ground-based interferometers, will carry otherwise-inaccessible information about neutron star interiors. In this thesis, we contribute to world's efforts to probe neutron stars with ground-based interferometers and pulsar timing arrays, as well as to improve the precision of searches for nanohertz gravitational waves.

Firstly, we improve the radiometer, the method to search for gravitational waves from spherically-asymmetric spinning neutron stars. The radiometer method complements continuous-wave searches, which aim to model time evolution of a gravitational-wave frequency, i.e. due to binary companion or intrinsic spin-down. The main advantage of the radiometer is its robustness, which can be helpful when detecting sources that might be missed by the dedicated continuous-wave techniques. Whereas previously radiometer has only been used to search for gravitational waves across the observing band from a few selected sky locations, in this work we extend the radiometer to all sky locations through developing the appropriate detection statistic. We built our method upon the previous work by Ain et al. (2015) and Thrane et al. (2015), where sidereal data folding was suggested to reduce computational and data-storage costs. We also developed the technique to remove non-stationary noise present in the real data.

Secondly, with pulsar timing arrays, we perform model selection for stochastic spin noise, associated with pulsar rotational irregularities. Pulsar spin noise power spectrum is usually modeled with the phenomenological power-law model. Sometimes the power-law model is supplied with a corner frequency parameter, below which the spin noise power spectrum plateaus. The corner frequency was introduced to account for the effects of data handling and there was no confirmed evidence for its existence in real data. Recently, a physical model of pulsar spin noise has been suggested by Melatos and Link (2014), with nearly power-law spectrum and a corner frequency. The model suggests that the superluid turbulence in a neutron star core is the origin of

spin noise. In our work, we perform Bayesian model selection for pulsar spin noise and we find no evidence of a spectral turnover. Our analysis also shows that the data from pulsars J1939+2134, J1024−0719 and J1713+0747 prefers the power-law model to the superfluid turbulence model.

Finally, we characterize time-correlated noise processes in the second data release of the Parkes Pulsar Timing Array. We identify and discuss new sources of noise with amplitude that depends on radio-frequency, we find steep spectra of spin noise and we discover new exponential events that we attribute to magnetospheric disturbances. Additionally, we outline a methodology to complement Bayesian inference with an independent metric to evaluate the performance of noise models and to characterize previously-unknown signals.

Dedication and acknowledgements

First of all, I would like to thank Eric Thrane for providing me with an opportunity to carry out this exciting research in the emerging field of gravitational-wave astronomy, as well as for the excellent professional and personal guidance. Eric kindly supported me during the ups and downs of my research and helped me to become the scientist I am today. Furthermore, I would like to thank my associate supervisor Xing-Jiang Zhu and my former associate supervisor Yuri Levin for useful discussions and for the hospitality during my arrival and stay in Melbourne. In particular, I thank Xing-Jiang for the great support during my first steps in pulsar timing. I also appreciate the opportunity to work with Daniel Reardon and Ryan Shannon, my informal supervisors at Swinburne University. I learned a lot from Daniel and Ryan and I thank them for being great people to work with. My special thanks go to Daniel, whom I spent the most time working with.

I am lucky to have a wonderful family that helped me to walk this path from the beginning to the end. I immensely appreciate the love and support of my parents, Valeriy Goncharov and Elena Goncharova, and my wife, Anastasia Goncharova. My family always inspires me to strive for excellence in what I am doing. Anastasia was by my side during the course of my Ph.D. and helped me to be better organized and to have an optimal work-life balance. We had a wonderful time travelling around Australia, exploring Melbourne, so that I returned back to work in good mood and with fresh ideas. I specially thank my parents for encouraging my interest in arts and sciences from an early age, for providing me with the top-quality well-rounded education, and for helping me to find my way in life. In fact, my dad told me the first fact I remember about neutron stars even before I went to school! He mentioned that a matchbox of neutron star matter weighs like a big train. This puzzled me for years to come.

I also would like to thank my colleagues from the School of Physics and Astronomy and OzGrav for creating an encouraging and friendly environment, for providing feedback on my work, and for organizing various informal social meetings, which made the Ph.D. life more fun.

At last, I would like to thank my former teachers and supervisors who helped me to get to the point of engaging into the Ph.D. program in the first place. My first school physics teacher, Natalya Vyacheslavovna Senatorova, always made lessons interesting and encouraged me to participate in “olympiads” in physics. I also thank my teachers at the Kolmogorov School and the Moscow State University, as well as my former supervisors, Vitaliy Vladimirovich Bogomolov and Bruce Grossan.

AUTHOR'S DECLARATION

I, Boris Goncharov, hereby declare that this thesis contains no material which has been accepted for the award of any other degree or diploma at any university or equivalent institution and that, to the best of my knowledge and belief, this thesis contains no material previously published or written by another person, except where due reference is made in the text of the thesis.

This thesis includes one paper published in the peer reviewed journal and two papers submitted to the peer reviewed journal. The core theme of the thesis is the understanding of gravitational-wave and timing properties of neutron stars. The ideas, development and writing up of all the papers in the thesis were the principal responsibility of myself, the student, working within the School of Physics and Astronomy under the supervision of Associate Professor Eric Thrane.

The inclusion of co-authors reflects the fact that the work came from active collaboration between researchers and acknowledges input into team-based research. In the case of Chapters 2, 3, and 4 my contribution to the work involved the following, shown on the following page.

SIGNED: ..... DATE: JUNE 12, 2020

I, Associate Professor Eric Thrane, hereby certify that the above declaration correctly reflects the nature and extent of the student's and co-authors' contributions to this work. In instances where I am not the responsible author I have consulted with the responsible author to agree on the respective contributions of the authors.

SIGNED: ..... DATE: JUNE 12, 2020

Declaration of published works contained in this thesis and acknowledgement of co-author contributions. No co-authors are students of Monash University.

Thesis chapter	**Publication title**	**Status**	**Nature and % of student contribution**	**Nature and % of co-author contributions**
2	All-sky radiometer for narrow-band gravitational waves using folded data	Accepted	80%: concept, method, analysis, writing	20%: Eric Thrane, concept, method, manuscript input
3	Is there a spectral turnover in the spin noise of millisecond pulsars?	Submitted	80%: concept, method, analysis, writing	10%: Xingjiang Zhu, concept, method, manuscript input; 10%: Eric Thrane, concept, method, manuscript input
4	Identifying and mitigating noise sources in precision pulsar timing data sets	Submitted	75%: concept, method, analysis, writing	10%: Daniel Reardon, concept, manuscript input, coding; 6%: Ryan Shannon, concept, manuscript input, coding; 2%: Eric Thrane, concept, manuscript input; 2%: Xing-Jiang Zhu, concept, manuscript input; 5% Parkes Pulsar Timing Array (PPTA) collaboration, observing and manuscript input

You take the blue pill – the story ends, you wake up in your bed and believe whatever you want to believe. You take the red pill – you stay in Wonderland and I show you how deep the rabbit-hole goes.

— Larry and Andy Wachowski, The Matrix

Table of Contents

List of Tables

List of Figures

CHAPTER 1

INTRODUCTION

We provide background information about neutron stars and pulsars and emphasise their importance in gravitational-wave astronomy. While doing this, we explain how our work fits into the global efforts to better understand the physics of neutron stars and to detect new sources of gravitational waves.

1.1 Neutron stars and pulsars: an overview

Shortly after the discovery of a neutron by Chadwick (1932), Baade and Zwicky (1934) proposed the existence of neutron stars as remnants of the cosmic supernovae explosions. Around the same time, Landau (1932) suggested that high stellar densities can cause atomic nuclei of a star to form one giant nucleus, which summarizes the basic idea of a neutron star. Eventually, it became clear that neutron stars are collapsed cores of stellar remnants, in the state of equilibrium between the repulsive strong force and self-gravitation. Stellar cores may also collapse into two other remnant equilibrium states, known as the white dwarf and the black hole.

The fate of a stellar core will depend primarily on its mass. For masses lower than $\approx 1.4\ M_\odot$, the self gravity of a collapsed remnant will remain in equilibrium with the electron degeneracy pressure. This state is known as the white dwarf. Initial calculations for the maximum mass of white dwarfs, known as the Chandrasekhar limit, were performed in the framework of degenerate Fermi gas by Anderson (1929, $0.7\ M_\odot$), Stoner (1930, $1.1\ M_\odot$), Chandrasekhar (1931, $0.9\ M_\odot$) and Landau (1932, $1.5\ M_\odot$). For non-rotating masses higher than $\approx 2.3\ M_\odot$, the self gravity of a stellar core will surpass the repulsive strong force, prompting a collapse into a black hole. Following the work by Tolman (1939) on static solutions of Einstein's field equations for spheres of fluid, Oppenheimer and Volkoff (1939) were first to calculate the maximum mass of nonrotating neutron stars in the framework of degenerate Fermi gas, obtaining the value of $0.7\ M_\odot$. The

Tolman-Oppenheimer-Volkoff limit has later been pushed above $\geq 2.0\ M_\odot$ by taking the strong nuclear force into account (see e.g. Cameron, 1959, 1970). The maximum nonrotating neutron star mass depends on the equation of state of nuclear matter, which remains the subject of active research.

As stellar cores collapse, their rotational velocities increase, according to the law of conservation of angular momentum. From conservation of the magnetic field flux, Woltjer (1964) estimated that neutron stars can contain magnetic fields with enormous strengths up to $10^{14} - 10^{16}$ G. Shortly after it has been predicted by Pacini (1967) that spinning neutron stars with strong magnetic fields will emit electromagnetic radiation, Hewish et al. (1968) discovered the first pulsating radio source in the sky. From the stable pulse period of 1.3 s, they identified the source of radio emission as a neutron star. Gold (1968) argued in favor of this hypothesis, suggesting that the observed neutron star emits electromagnetic radiation, powered by rotation, which brings the plasma in the magnetosphere up to relativistic velocities. The relativistic plasma directs electromagnetic radiation away from a neutron star along its magnetic field axis. The misalignment between the rotational axis and the magnetic field axis is what makes radio emission to be seen as a pulsating "lighthouse beam". Neutron stars that are observed in this way are called pulsars. A year earlier, Shklovsky (1967) substantiated that the origin of the X-ray emission from Scorpius-X1, the brightest source of such emission in the sky after the Sun, is accretion of matter onto a neutron star. These and following discoveries transformed neutron stars from purely theoretical entities to real astronomical objects that can be observed and studied.

1.1.1 Population of galactic neutron stars

Although several galactic neutron stars are observed as non-pulsating sources of electromagnetic radiation (see e.g. Klochkov et al., 2013; Viganò and Pons, 2012), most of the galactic neutron stars observed by today are pulsars. The ATNF pulsar catalogue (Manchester et al., 2005) contains more than 2800 pulsars. To discuss the evolution of pulsars, it is convenient to present the data from the pulsar catalogue on the so-called "P - $\dot{P}$" diagram, where P is the pulsar spin period and $\dot{P}$ is its time-derivative. We show this diagram in Figure 1.1. The characteristic age of a pulsar is estimated as in Lorimer and Kramer (2004):

$$\tau_c \equiv \frac{P}{2\dot{P}}, \tag{1.1}$$

assuming that the pulsar spin period at birth was much lower than the present spin period and that the spin down mechanism is purely a magnetic dipole radiation. The magnetic field strength on the surface of a pulsar is given by Lorimer and Kramer (2004) as:

$$B_{\rm S} = \sqrt{\frac{3c^3}{8\pi^2}\frac{I}{R^6 \sin^2\alpha} P\dot{P}}, \tag{1.2}$$

where R is the radius of a neutron star and α is the angle between the magnetic field axis and the rotational axis. As a pulsar gets older, the magnetic field becomes weaker and the spin period

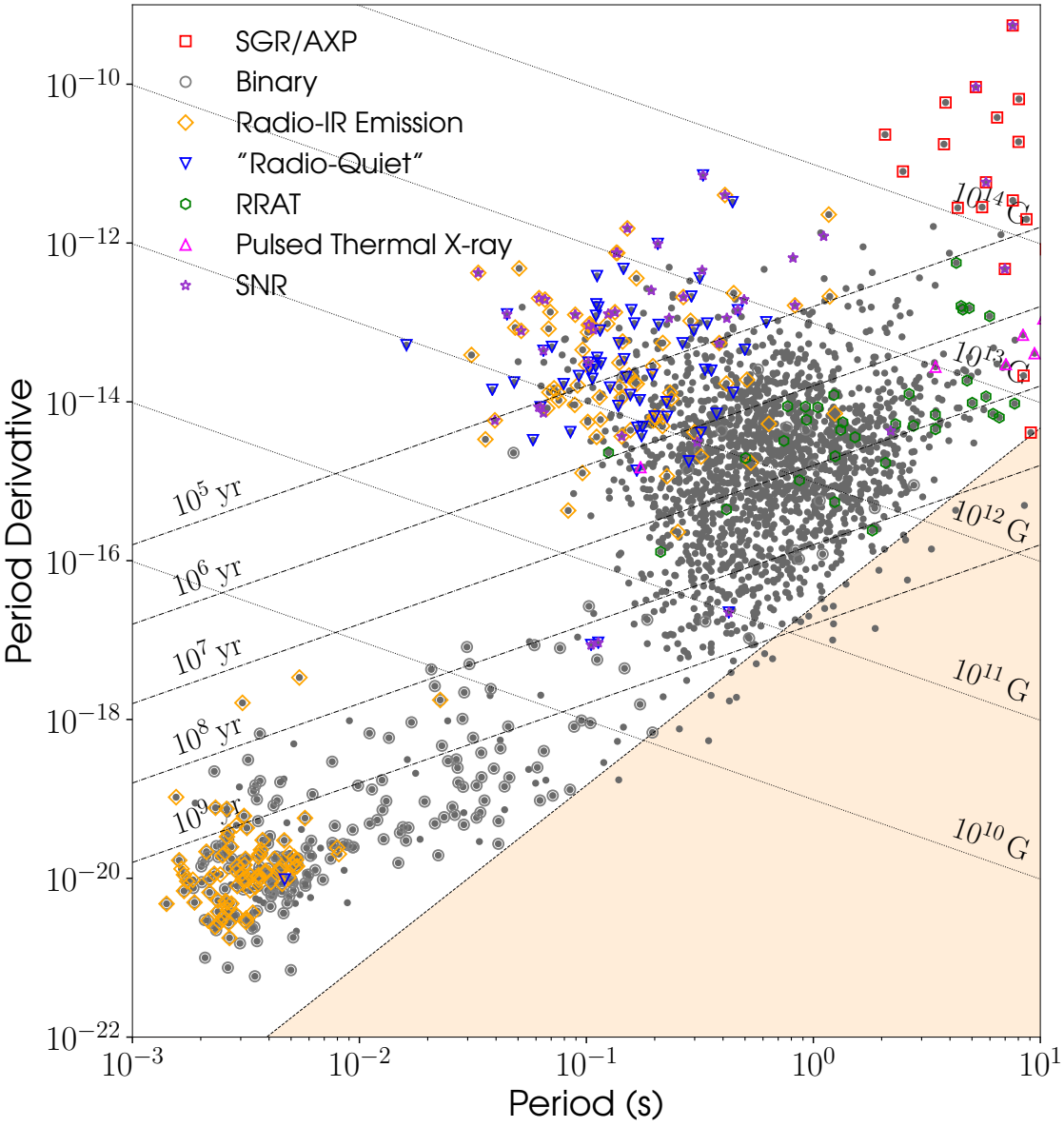

FIGURE 1.1. The "P - $\dot{P}$" diagram for pulsars from the ATNF Pulsar Catalogue (Manchester et al., 2005). For each pulsar, denoted by a grey dot, the diagram provides the spin period (horizontal axis) and its time-derivative (vertical axis). The orange shaded region represents the pulsar "graveyard", according to Equation 4 in Zhang et al. (2000), where radio emission is expected to stop due to inability of pulsar's inner magnetosphere to generate electron-positron pairs. SGR stands for "soft gamma repeaters", AXP stands for "anomalous X-ray pulsar", IR stands for "infrared", RRAT stands for "rotating radio transient sources" (intermittent pulsars), "SNR" stands for "supernovae remnants". Dashed lines represent characteristic ages, dotted lines represent estimates of surface magnetic fields. The plotting code is developed by Pitkin (2018).

becomes longer. This is demonstrated in Figure 1.1. Pulsars are expected to exhaust their energy up to the point where the electromagnetic emission mechanism stops. At this point, a neutron star is no longer a pulsar. It will appear in the bottom-right orange-shaded region in Figure 1.1, referred to as the graveyard. The border of the graveyard is referred to as the death line. In the P - $\dot{P}$ diagram in Figure 1.1, the graveyard is represented by Equation 4 from Zhang et al. (2000). It determines the case where the electromagnetic field in the inner magnetosphere of a pulsar is no longer strong enough to support the vacuum gap, the region where electron-positron pairs are born, with a size larger than the mean electron free path. Electrons are an essential fuel for the electromagnetic emission. The fact that some pulsars are still observed within the graveyard on Figure 1.1 demonstrates that determination of pulsar emission mechanisms remains as one of the goals of pulsar astronomy. One of the interesting phenomena in pulsar observations is nulling, which has been first observed by Backer (1970). During nulling, pulse energy significantly decreases. Coincidentally, nulling is more likely to occur in pulsars near the graveyard (Ritchings, 1976). Given the life span of an average pulsar of around a billion years, in $\sim 10^{10}$ year old Universe the vast majority of neutron stars are not expected to emit electromagnetic pulses.

Pulsars in the P - $\dot{P}$ diagram appear to be concentrated in three areas. The first area, with estimated surface magnetic fields around 10^{10} - 10^{13} G, contains normal pulsars. Pulsars clustered around the second area, with estimated surface magnetic fields around 10^{13} - 10^{15} G, are called magnetars. Duncan and Thompson (1992) suggested that they are neutron stars where the seed helical magnetic field has been amplified under dynamo action. The third area, with surface magnetic fields below 10^{10} G, contains recycled pulsars, which have been spun up by accretion from their binary companions (Bisnovatyi-Kogan and Komberg, 1974). They are also referred to as millisecond pulsars, as their spin periods can be as low as ~ 1 ms. At very high rotation rates, centrifugal force is expected to break neutron stars apart. The breakup rotation period depends on the equation of state of nuclear matter, but estimated to be on the order of 0.1 ms (Haensel et al., 1999). The most rapidly rotating pulsars known today do not reach these limits. PSR J1748−2446ad has the lowest observed spin period of 1.4 ms (Hessels et al., 2006). Among pulsars, which are known to accrete matter, IGR J00291+5934 has the lowest spin period of 1.7 ms (Patruno and Watts, 2012). Wagoner (1984) proposed that accreting neutron stars will eventually acquire enough angular momentum to become unstable to the emission of gravitational waves. Later, Bildsten (1998) suggested that for rapidly rotating neutron stars with the highest spin frequencies, angular momentum acquired by accretion is lost through the emission of gravitational waves. This is known as the torque-balance hypothesis. It provides a motivation to search for gravitational radiation from neutron star interiors.

1.1.2 Pulsar timing

The clock-like nature of pulsar electromagnetic emission enables studies of every physical aspect that affects its generation and propagation. In Section 1.1.1 we discussed that measurements of

pulse arrival times allow us to calculate pulsar spin period and its time-derivative and hence to estimate the pulsar age and its surface magnetic field. This is only the tip of the iceberg of pulsar timing array science. Here we will mostly discuss applications relevant to this thesis. For more information, please refer to Lorimer and Kramer (2004); Lyne and Graham-Smith (2012).

The first step in measuring the pulse time of arrival is de-dispersion, the process of correcting for time delays at different radio-frequencies caused by dispersion of a radio pulse in the interstellar medium (Lorimer and Kramer, 2004). Dispersion induces time delays $\Delta t_{\rm DM} \sim \nu^{-2}$, where ν is a radio frequency. Inhomogeneities in the interstellar medium cause pulse multi-path scattering and scintillation. Pulse scattering broadens the observed pulse shape, which causes non-stationary time delays $\Delta t_{\rm SC} \sim \nu^{-4}$ (Lyne and Graham-Smith, 2012, Equation 3.9). Scintillation appears as non-stationary pulse intensity variations.

Pulsar timing also provides unique opportunities to study the dynamics of binary systems. The delay in light travel times between astronomical objects, associated with a change in position of these objects due to orbital motion, is called the Roemer delay. The Roemer delay includes the effect of Doppler shifting of the pulse train due to the binary motion. It allows us to constrain Keplerian parameters of the binary: the orbital period, the eccentricity, the projected semi-major axis, the longitude of periastron, the epoch of periastron, the longitude of the accending node. Yet pulsar timing goes beyond the classical Newtonian formalism. Like many other binary systems with pulsars, the first one discovered by (Hulse and Taylor, 1975), PSR B1913+16 (PSR J1915+1606), is highly relativistic. The period of the binary system is only ~ 8 hr. Stellar masses in such tight orbits with high velocities enable precise tests of General Relativity. The Roemer delay for a binary is modified for the relativistic case, to account for relativistic deformations of the orbit. Additionally, the Einstein delay is introduced to account for redshift and time dilation in strong gravitational fields and the Shapiro delay is introduced to account for time delays along the curved path of null geodesic between the pulsar and the observer. Most importantly, general relativity predicts the evolution of Keplerian parameters in time. In particular, the advance of periastron and the orbital decay due to the emission of gravitational waves. By observing PSR J1915+1606, Taylor and Weisberg (1982) reported that the orbital decay is consistent with the emission of gravitational waves, predicted by general theory of relativity. This discovery has significantly increased the overall confidence in the existence of gravitational radiation in nature, providing more motivation to directly detect it. Relativistic frame dragging around a rapidly-rotating massive object, known as the Lense-Thirring precession, is another general relativistic effect that has been observed by Krishnan et al. (2020) in a binary system that contains the white dwarf and the neutron star PSR J1141−6545.

It has also been pointed out by Detweiler (1979); Sazhin (1978) that pulsar timing can be employed to search for nanohertz gravitational waves from supermassive black hole binaries. To achieve this, Foster and Backer (1990b) proposed to establish pulsar timing arrays that would look for quadrupole spatial correlations between millisecond pulsars, expected from the nanohertz

stochastic gravitational-wave background (Hellings and Downs, 1983). Millisecond pulsars are best suited for this purpose because they provide the best timing precision. For example, in the second data release of the Parkes Pulsar Timing Array (Kerr et al., 2020), the timing precision achieved with PSR J2241−5236 over an 8-year period is 270 ns. Current upper limits on the amplitude of the nanohertz stochastic background from pulsar timing arrays are already in tension with some theoretical models (Shannon et al., 2015). According to Zhu et al. (2019), current limits are consistent with the supermassive black hole number density inferred from electromagnetic observations. Taylor et al. (2016) predicts that the detection can be made within the next decade of observations, even considering the scenarios where supermassive black hole binary evolution stalls.

Pulsar timing precision is limited by various stochastic processes. On the time scales of under a week, the uncertainty of a pulse arrival time is mostly affected by pulse shape variability, known as the jitter noise, and instrumental measurement errors, known as the radiometer noise. On the longer time scales, normal pulsars experience the timing noise, which includes glitches and spin noise. Spin noise manifests as ever-lasting stochastic drift of pulse arrival times. A glitch is a sudden change in the rotation period of a pulsar, usually followed by an exponential recovery. An example of a pulsar that is known to glitch a lot is the Vela pulsar PSR B0833−45 (McCulloch et al., 1983). Analyses of the data from high time resolution observations of Vela glitches indicated that there is a presence of additional rotational frequency "overshoot" (Dodson et al., 2001) and possibly the precursor slow down (Ashton et al., 2019b). Both the glitches and the timing noise provide exciting prospects of studying neutron star physics, which we will discuss in more details in Section 1.3 and in Chapter 3. For millisecond pulsars, timing noise levels significantly drop (Parthasarathy et al., 2019), which is the main reason why millisecond pulsar timing is so precise. Overall noise properties of millisecond pulsars will be discussed in Chapter 4.

1.1.3 Neutron stars in gravitational-wave astronomy

Albert Einstein discovered that the field equations in the general theory of relativity contain radiative solutions, predicting the existence of gravitational waves, space-time metric perturbations h propagating at the speed of light. The gravitational wave can be represented as a combination of two modes, the plus polarization (h_+) and the cross polarization ($h_\times$), which can be interchanged by the 45-degree rotation around the propagation axis. Einstein calculated the Newtonian-limit approximation for the luminosity of an isolated source of gravitational waves (Camenzind, 2007, Equation 2.332):

$$-\frac{dE}{dt} = \frac{G}{5c^5}\sum_{i,j=1}^{3}\frac{d^3Q_{ij}}{dT^3}\frac{d^3Q_{ij}}{dT^3}, \tag{1.3}$$

where G is the gravitational constant, c is the speed of light, $(\mathbf{x}, T)$ is the coordinate system in the frame of a source, and

$$Q_{ij}(t) = \int \rho(\mathbf{x}, t)\left(x^i x^j - \frac{1}{3}\delta^{ij}\mathbf{x}^2\right)d^3x \tag{1.4}$$

is the observed quadrupole moment of inertia of a source, with $\rho(\mathbf{x}, t)$, the Newtonian mass density. Non-zero quadrupole moment is thus the main requirement and "fuel" for the gravitational-wave emission. It is clearly seen from the above two equations that the energy carried away from the source by gravitational radiation is a factor of G/c^5, which is very small. So, in order to produce measurable gravitational radiation, astrophysical sources have to compensate that factor by large masses and rapid rotation. Inspiraling compact objects, black holes, neutron stars and white dwarfs, were put forward as the most promising targets for gravitational wave detection. For binaries with masses M_1 and M_2, in orbits with semi-major axis a and eccentricity e, treated as point particles, gravitational-wave luminosity of the binary is (Peters and Mathews, 1963):

$$-\frac{dE}{dt} = \frac{32}{5}\frac{G^4 M_1^2 M_2^2 (M_1 + M_2)}{a^5 c^5 (1-e^2)^{7/2}}\left(1 + \frac{73}{24}e^2 + \frac{37}{96}e^4\right). \tag{1.5}$$

The luminosity depends on a^{-5}, which means that the amount of energy drawn from the binary orbit into the gravitational radiation keeps increasing until the collision. This results in a so-called "chirp" signal, as both the intensity and the frequency of a gravitational-wave signal keeps increasing as the binary inspirals and reaches its maximum at the moment of collision. The observer can measure the gravitational-wave strain, the relative displacement of massless free falling point particles, as a gravitational wave passes by. The strain amplitude of gravitational waves from binary neutron star system is (Press and Thorne, 1972):

$$h(t) \approx 10^{-23}\left(\frac{\mu}{M_\odot}\right)\left(\frac{M}{M_\odot}\right)^{2/3}\left(\frac{R}{30\ \mathrm{Mpc}}\right)^{-1}\left(\frac{P}{1\ \mathrm{s}}\right)^{-2/3}\frac{1}{(1-e^2)^{7/2}}\left(1 + \frac{73}{24}e^2 + \frac{37}{96}e^4\right), \tag{1.6}$$

where $M_\odot$ is the mass of the Sun, $M = M_1 + M_2$ is the total mass, $\mu = M_1 M_2/M$ is the reduced mass, P is the orbital period, R is the distance from the observer.

Unlike white dwarfs and black holes, neutron stars are predicted to produce measurable gravitational radiation as they spin due to axial asymmetry. The physical mechanisms are discussed in Section 1.2. Within the order of magnitude, gravitational-wave luminosity of an asymmetric neutron star is (Press and Thorne, 1972):

$$-\frac{dE}{dt} \sim \frac{G}{c^5}\varepsilon^2 I_{zz}^2 \nu^6. \tag{1.7}$$

Parameter ε is the non-axisymmetric fraction of the moment of intertia, also known as the ellipticity. The moment of interia along the rotational axis is I_{zz}. The rotation frequency of a neutron star is ν. The measured gravitational-wave strain is (Becker et al., 2009, Equation 24.9):

$$h(t) \sim 10^{-25}\left(\frac{\varepsilon}{10^{-6}}\right)\left(\frac{I_{zz}}{10^{38}\ \mathrm{kg\ m^2}}\right)\left(\frac{\nu}{100\ \mathrm{Hz}}\right)^2\left(\frac{100\ \mathrm{pc}}{R}\right). \tag{1.8}$$

The values for R, ε, I_{zz} and ν in Equation 1.6 and Equation 1.8 are the values that a theorist would expect to occur in nature. Whereas pulsar timing provides some estimates on I_{zz}, the value of ε remains purely theoretical. Still, the main point here is that the gravitational-wave strain produced by asymmetric neutron stars in our Galaxy is several orders of magnitude smaller than the strain produced by extragalactic inspiraling binary neutron stars.

The current and proposed gravitational-wave detectors are interferometer-based. They can be attributed to three classes, based on gravitational wave frequencies they are most sensitive to. The first class of experiments are ground-based interferometers, which are most sensitive at $\sim$ 10 – 1000 Hz, the domain of asymmetric neutron stars and stellar-mass compact object mergers. The Advanced Laser Interferometer Gravitational-Wave Observatory (Advanced LIGO, Harry et al., 2010) was the first one to directly detect gravitational waves. It was a binary black hole merger signal (Abbott et al., 2016b). The fourth such signal (Abbott et al., 2017d) has been simultaneously detected by the Advanced LIGO and the Advanced Virgo detectors (Acernese et al., 2014). The second class are space-based experiments (Amaro-Seoane et al., 2012), which are proposed for the future and designed to be sensitive to gravitational-wave frequencies around 0.1 – 100 mHz, where massive black holes merge and stellar-mass binaries coalesce. The third class of experiments are pulsar timing arrays (Hobbs et al., 2010a), operating in the nHz band, where supermassive binary black holes emit gravitational waves. Pulsar timing arrays are galactic-scale interferometers, with arms stretching from the Solar System to the pulsars in the Milky Way. Among other kinds of compact objects in gravitational-wave astronomy, neutron stars are unique. They are not only sources of gravitational waves, but also a part of the nature-built detector. We explore both sides of this duality in our work.

1.2 Gravitational-wave emission from neutron stars

Gravitational wave emission from neutron stars would provide a unique observational perspective to these astronomical objects. Several physical mechanisms have been proposed to be responsible for the development of axial asymmetry in neutron stars, required for the gravitational wave emission. We only provide a short summary of the theory of the generation of persistent gravitational waves and discuss the cases for which the long observation time can outweigh the relatively small strain amplitudes experienced by an observer. For more details, please refer to Lasky (2015); Riles (2017); Sieniawska and Bejger (2019).

1.2.1 Theoretical perspective

In addition to the surface poloidal magnetic field, which is responsible for pulsar emission mechanism, it is predicted that a neutron star contains even stronger internal toroidal magnetic field (Bransgrove et al., 2018). It has been predicted that the internal magnetic field can deform a neutron star, causing a non-zero ellipticity (Haskell et al., 2008). The gravitational-wave fre-

quency will be emitted at twice the rotational frequency of a neutron star. This mechanism is expected to deform magnetars the most because of their extreme magnetic fields. However, due to low rotational frequencies of magnetars of $\lessapprox 1$ Hz, gravitational waves from these sources are below the observing band of ground-based interferometers. Thus, the hopes of detecting gravitational waves from these pulsars with LIGO and Virgo instruments lie mostly on normal young pulsars. The good news is that if a neutron star contains matter in the colour superconductor state, which is expected, the colour-magnetic interaction is expected to increase the star's ellipticity (Glampedakis et al., 2012). Neutron star ellipticity can also develop through unstable oscillation modes. The most prominent example are r-modes, caused by the Coriolis force. Andersson and Kokkotas (2001) found that r-modes of rotating neutron stars can be unstable to gravitational radiation, providing another possible channel for an emission of gravitational waves. The frequency of gravitational waves from r-modes is 4/3 of the star's rotational frequency (Riles, 2017). R-mode oscillations can be supported through the accretion (Lasky, 2015). Furthermore, following the structure of an external magnetic field, the matter accreted by neutron stars can form magnetically-confined mountains (Melatos and Payne, 2005b), providing a non-zero ellipticity. In fact, the quadrupole moment developed though this process is expected to be larger than the quadrupole moment from the deformations of non-accreting neutron star's toroidal magnetic field (Vigelius and Melatos, 2009). Moreover, Bildsten (1998) showed that temperature gradients in the crust of a neutron star can also sustain a non-zero quadrupole moment. This mechanism is also referred to as the elastic deformations. It is worth noting that the quadrupole moment of an asymmetric neutron star can also be developed through the precession (Alpar and Pines, 1985). The gravitational-wave signal is then emitted at frequencies of 2ν and $\nu + \nu_{\rm P}$, where ν is the rotation frequency and $\nu_{\rm P} << \nu$ is the precession frequency (Sieniawska and Bejger, 2019). Pinned superfluid in the neutron star core also causes a gravitational wave emission at ν (Jones, 2010). The variety of theoretical scenarios and observational signatures, even in terms of a gravitational-wave frequency, would provide extremely valuable information about the neutron star physics, once gravitational waves from neutron stars are detected.

1.2.2 Observational perspective

Electromagnetic observations of neutron stars, including pulsar timing, provide opportunities to directly or indirectly estimate the loss of their rotational energy. We discuss the three models, which provide limiting-case empirical estimates on the gravitational-wave strain expected from pulsars. Firstly, we can place a theoretical upper limit on the gravitational-wave strain from neutron stars, if we assume that all energy that is lost during the pulsar spin down is emitted as gravitational waves. This way, we obtain (Riles, 2017):

$$h_{\rm SD} = 2.5 \times 10^{-25} \left(\frac{1\ \text{kpc}}{R}\right) \sqrt{\left(\frac{1\ \text{kHz}}{\nu}\right)\left(\frac{-\dot{\nu}}{10^{-10}\ \text{Hz/s}}\right)\left(\frac{I_{zz}}{10^{38}\ \text{kg m}^2}\right)}. \tag{1.9}$$

Similarly, Wette et al. (2008) derived a theoretical upper limit on the gravitational-wave strain based on the neutron star age T_{NS}, for the case when the spin period and the spin down rate are unknown:

$$h_{\mathrm{AGE}} = 2.2 \times 10^{-24} \left(\frac{1\ \mathrm{kpc}}{R}\right)\left(\frac{I_{zz}}{10^{38}\ \mathrm{kg\ m^2}}\right)\left(\frac{1000\ \mathrm{yr}}{T_{\mathrm{NS}}}\right). \tag{1.10}$$

In the third model, we assume that the extra angular momentum from an accretion in millisecond pulsars is radiated away only in a form of gravitational waves. For this case, when the observed accretion-driven X-ray flux is $\mathscr{F}_{\text{X-ray}}$, Bildsten (1998) obtained:

$$h_{\mathrm{TB}} = 3.5 \times 10^{-27} \sqrt{\left(\frac{600\ \mathrm{Hz}}{\nu}\right)\left(\frac{\mathscr{F}_{\text{X-ray}}}{10^{-8}\ \mathrm{erg/cm^2 s}}\right)}. \tag{1.11}$$

Whereas the gravitational-wave emission from the inspiral of compact binaries is more theoretically straightforward to calculate and observe indirectly (Hulse and Taylor, 1975), the situation with neutron stars is much less certain. Nevertheless, the detection of a gravitational-wave signal from a neutron star would be rewarding. The searches for long-lasting gravitational-wave signals are called the continuous-wave searches. In general, the continuous-wave searches aim to detect long-lasting signals from neutron stars, buried within the noise of a ground-based interferometer. Their aim is to model frequency evolution and Doppler modulation of a signal. This becomes a harder problem when the search involves neutron stars in binaries with unknown orbital parameters. Theoretical unknowns, such as irregularities in neutron star rotation (Ashton et al., 2017), observed in the field of pulsar timing, introduce even more uncertainty to modelling the gravitational-wave emission. This motivated the development of the radiometer method (Ballmer, 2006), which is designed to be robust, only assuming the signal is persistent and approximately monochromatic. Thus, searches for gravitational waves using the radiometer are referred to as searches for persistent gravitational waves, in order to distinguish them from continuous-wave searches. Previous narrowband radiometer searches (Abadie et al., 2011; Abbott et al., 2017b, 2019) targeted specific directions on the sky. In Chapter 2, we demonstrate the techniques that allow to perform the radiometer search over all sky locations.

1.3 Timing irregularities of pulsars

The smooth time evolution of pulsar rotation is often affected by the two stochastic processes, known as the glitch and the spin noise. These processes are considered to be intrinsic to pulsars and provide interesting opportunities to study neutron star physics.

1.3.1 Pulsar glitches

Pulsar glitches appear as sudden boosts $\delta\nu$ of pulsar spin frequency ν. Melatos et al. (2008) suggested that glitches are examples of scale-invariant self-organized critical systems, as described

by Jensen (1998), with power-law probability distribution for $\delta\nu/\nu$. This process can be thought of as self-adjustments of a neutron star, following changes in the equilibrium state, analogous to sand pile avalanches occurring as more sand is added on the top. The frequency of glitch appearance follows a Poisson distribution. The standard glitch model is based on the superfluid nature of the neutron star core, coupled to the neutron star crust where the magnetic field is produced (Alpar et al., 1981). It is believed that the sudden change in pulsar rotational frequency, through the moment of intertia, can be related to the sudden change in the ellipticity due to the sudden cracking of the solid crust (Lyne and Graham-Smith, 2012). The superfluid cooper-paired neutron fluid rotates only in the form of vortices, angular momentum quanta (Ruderman et al., 1998). The standard glitch model, proposed by Anderson and Itoh (1975), states that the glitch happens when the vortices, pinned to the core, get unpinned, move outward and transfer the angular momentum from the core to the crust, which is what we observe through electormagnetic radiation. The pinning-breaking Magnus force develops through the differential rotation inside a star. Unless the neutron star is observed in gravitational waves, neutron star core remains hidden from the observer, revealing itself only indirectly, through its influence on the crust.

1.3.2 Pulsar spin noise

Pulsar spin noise appears as a slow drift of pulse arrival over years of observations, with amplitude of that drift diminishing as pulsar becomes older (Hobbs et al., 2010b). The old population of millisecond pulsars eventually ends up with little or no spin noise, which makes their timing so precise. The observation-driven hypothesis for pulsar spin noise, brought up by Lyne et al. (2010), links the origin of the noise to the switching between the two spin down rates in pulsars. Timokhin (2010) proposed that each spin down rate corresponds to the certain quasi-stable state of the pulsar magnetosphere. Observations also suggest that spin noise can the result of micro-glitches (Cordes and Downs, 1985; D'Alessandro et al., 1995) and post-glitch recoveries (Johnston and Galloway, 1999b). From the theoretical point of view, pulsar spin noise is expected to be the effect of the same neutron star physics that gives rise to glitches. Melatos and Link (2013) suggested that the superfluid turbulence in neutron star cores can exert torque on the crust, which results in the stochastic rotational irregularities. In this thesis, we perform the first statistically-rigorous observational test of this model.

Various external effects, including the influence of planets and asteroids, can affect the non-zero $\ddot{\nu}$ and hence to appear as spin noise. These effects, as well as various stochastic processes that depend on a radio frequency (i.e., variations in electron column density towards the line of sight to a pulsar), have to be taken into account to properly model spin noise. It is also important to correctly characterize all these systematic effects in millisecond pulsars to carry out searches for the nanohertz-frequency stochastic gravitational-wave background. We perform this analysis in Chapter 4 and discover new effects that appear as the stochastic time of arrival fluctuations and the sudden changes in pulse arrival times, with some or no dependence on radio frequency.

CHAPTER 2

ALL-SKY RADIOMETER FOR NARROWBAND GRAVITATIONAL WAVES USING FOLDED DATA

Published as:
Goncharov, B., & Thrane, E. (2018). Physical Review D, 98(6), 064018.

We demonstrate an all-sky search for persistent, narrowband gravitational waves using mock data. The search employs radiometry to sidereal-folded data in order to uncover persistent sources of gravitational waves with minimal assumptions about the signal model. The method complements continuous-wave searches, which are finely tuned to search for gravitational waves from rotating neutron stars, while providing a means of detecting more exotic sources that might be missed by dedicated continuous-wave techniques. We apply the algorithm to simulated Gaussian noise. We project the strain amplitude sensitivity assuming circularly polarized signals for the LIGO network in the first observing run to be $h_0 \approx 1.2 \times 10^{-24}$ (1% false alarm probability, 10% false dismissal probability). We include a treatment of instrumental lines and detector artifacts using time-shifted LIGO data from the first observing run.

2.1 Introduction

With the first observations of a binary neutron star inspiral GW170817 (Abbott et al., 2017e) and multiple black hole mergers (Abbott et al., 2016a,b, 2017d,g,h) by Advanced LIGO (Harry et al., 2010) and Advanced Virgo (Acernese et al., 2014), it is clear that nature provides us with a unique way to study electromagnetically invisible processes using gravitational radiation. The discovery

of persistent gravitational-wave emission remains an interesting prospect for gravitational-wave astronomy. In this work, we develop a method for detecting quasi-monochromatic (narrowband), persistent gravitational waves from unknown sources using data from advanced detectors.

Searches for continuous gravitational waves are designed to be as sensitive as possible to rotating neutron stars. However, to achieve this, they employ a highly tuned signal model. If neutron stars emit gravitational waves in a way that does not match standard models, or if there are exotic sources of persistent gravitational waves, the signal could be missed by current continuous-wave searches. The radiometer (Abadie et al., 2011; Abbott et al., 2007d, 2017b; Ballmer, 2006; Thrane et al., 2009) provides a solution. By cross-correlating data from two or more detectors, it is possible to discover weak signals without a model for the signal phase evolution. Due to computational limitations, previous radiometer searches were either targeted (pointing in one direction) and narrowband (considering many different frequencies) or all-sky (looking in all directions) but broadband (averaging over all frequencies). Since it seems unlikely that point sources of persistent gravitational waves would be broadband, it is desirable to carry out an all-sky narrowband search[1]. In (Thrane et al., 2015b) it was pointed out that sidereal folded data (Ain et al., 2015) can be used to carry out a computationally cheap search that is both all-sky and narrowband. In this paper, we employ the method from (Thrane et al., 2015b) to demonstrate the technique on an end-to-end study of Monte-Carlo noise. Using limited data from LIGO's first observing run (O1), we show how vetoes can be used to manage instrumental artifacts found in real data.

The rest of the paper is organized as follows. Section 2.2 provides the motivation for a search for unmodeled persistent sources. In Section 2.3, we provide an overview of the narrowband radiometer with folded data. Section 2.4 describes how we handle instrumental artefacts and other data quality issues. In section 2.5, we demonstrate the detection of simulated signals. In Section 2.6, we calculate the sensitivity of the search.

2.2 Motivation

2.2.1 Astrophysical sources

Accreting neutron stars in binaries are considered to be promising candidate sources of persistent gravitational waves. Optimistic models predict for such systems to have an asymmetrical quadrupole moment of inertia $Q_{ij}(t)$ (Equation 1.4) due to either deformation of the stellar interior (Melatos and Payne, 2005a) or localized mass accumulation (Vigelius and Melatos, 2009). In either scenario, the quadrupole moment of inertia evolves through accretion and the influence of the neutron star magnetic field. The quadrupole moment may be sustained even when accretion

[1]After this paper was submitted for publication, a preprint appeared proposing gravitational waves from networks of primordial black holes connected by strings (Vilenkin et al., 2018). It seems possible to us that such a network could produce broadband point sources.

has abated. Gravitational-wave driven instabilities of r-mode oscillations are another source of a quadrupole moment (Reisenegger and Bonačić, 2003; Ushomirsky, 2001). If accretion is persistent, and neglecting torque from gravitational waves emission, neutron stars are expected to eventually spin up to their break up frequency $f \approx 1400$ Hz (Chakrabarty et al., 2003). However, the highest yet observed frequency is $f \approx 716$ Hz for a millisecond pulsar (Hessels et al., 2006) and $f \approx 600$ Hz for an accreting millisecond pulsar (Patruno and Watts, 2012), which is consistent with a hypothesis that emission of persistent gravitational waves prevents further spin up of neutron stars. This is known as the torque balance hypothesis (Bildsten, 1998; Wagoner, 1984).

Searches for continuous gravitational waves specifically target neutron stars. However, in certain circumstances these searches can be sub-optimal. For example, when a neutron star is in a binary system, it is computationally challenging to search the full signal parameter space. Another example is a neutron star glitch, a sudden increase in the rotation frequency, a phenomenon observed in the timing of many radio pulsars (Espinoza et al., 2011). It has been shown that neutron star glitches can cause a loss of a substantial fraction of a signal-to-noise ratio in continuous wave searches (Ashton et al., 2017).

Another motivation for the method discussed here is to explore the possibility of unknown persistent and narrowband signals. One such theoretical scenario is gravitational waves from super-radiance of massive clouds of ultralight axions around a Kerr black hole (East and Pretorius, 2017). The frequency of gravitational waves from this long-lived resonance depends on the mass of a hypothetical axion particle. Thus, a narrowband emission is expected. Axions with a mass of $\sim 10^{-11} - 10^{-14}$ eV could possibly be detected by Advanced LIGO (Brito et al., 2017).

2.2.2 Searches for persistent gravitational waves

Currently there are several methods for persistent gravitational wave searches. In this section of the paper, we outline what niche the narrowband radiometer search occupies. A comprehensive overview of current searches for persistent gravitational waves can be found in (Riles, 2017).

One of the main difficulties in searches for persistent gravitational wave is the amount of computational resources that are required to probe the parameter space of possible gravitational-wave frequencies and their time derivatives. Searches have to account for Doppler modulations of the gravitational-wave signal due to motion of the Earth. Moreover, torque exerted on a neutron star by accretion from a companion star may change with time, resulting in wandering of the neutron star spin frequency (Ghosh and Lamb, 1979).

Knowing orbital parameters for some sources of persistent gravitational wave emission eliminates the problem of searching over gravitational-wave frequencies and their derivatives. Using the data from radio and gamma-ray observations, recent searches placed upper limits on gravitational-wave strain from 200 known pulsars (Abbott et al., 2017a). If the target is an accreting neutron star in a binary system, it may be possible to narrow down a parameter space by looking at X-ray pulsations (Galloway et al., 2013).

There are three kinds of searches. Searches for neutron stars with known sky position and known frequency are referred to as targeted searches. Directed searches target specific sky locations without assumptions about the gravitational wave frequency. All-sky searches employ no assumptions for either sky location or frequency. Targeted searches can employ matched filtering (Jaranowski, 1998), a Bayesian approach (Dupuis and Woan, 2005), and the "Five-vector" method (Astone et al., 2010).

In a directional search one faces a problem of exploring a vast parameter space of frequency and its derivatives. Fully coherent searches are too computationally expensive for all-sky searches, and are adapted to limited observation time and/or specific sky directions (Dhurandhar et al., 2008; Wette et al., 2008). In semi-coherent searches one instead sums results from coherent analysis over much shorter time intervals, for longer observation time (Wette, 2015). Semi-coherent methods are less computationally expensive than fully coherent ones, and sometimes they are used for all-sky searches. TwoSpect is an example of a template-based semi-coherent all-sky search, which tracks Earth's rotation-induced modulations of gravitational waves in doubly Fourier transformed data (Goetz and Riles, 2011). Polynomial algorithm uses a bank of frequency polynomials for matched filters (van der Putten et al., 2010). Hidden Markov model tracking method using a Viterbi algorithm (Suvorova et al., 2016) for matched filtering. Other semi-coherent searches include "Stack Slide" (Brady et al., 1998), the Hough approach (Antonucci et al., 2008; Hough, 1959; Krishnan et al., 2004), Powerflux (Dergachev, 2010), and Einstein@Home (Abbott et al., 2009), a volunteer-distributed computing project. These semi-coherent search strategies rely on signal models of gravitational-wave emission from neutron stars. They are in some sense limited by computational resources.

A different approach to the problem of a frequency modulated signal is to formulate a model-independent search. The radiometer technique is used to identify signals with the cross-correlation of Fourier-transformed strain from two or more gravitational wave detectors (Ballmer, 2006), and it underpins the method described in this paper. Cross-correlation contains information about the source sky location. The radiometer works with minimum assumptions about a signal, only presuming it is persistent and narrowband.

Scorpius X-1 is the second brightest persistent X-ray source in the sky (Giacconi et al., 1962). It is believed to be an accreting neutron star. According to the torque balance hypothesis, this system is a source of persistent gravitational waves. Using simulated Scorpius X-1 signals, it has been estimated that the *targeted* radiometer algorithm has less sensitivity than CrossCorr, a comparable sensitivity to TwoSpect, while at the same time it uses less than 1% of computational resources of these pipelines (Messenger et al., 2015). It has been demonstrated that a lossless data compression technique called folding can complement the narrowband radiometer, further reducing a computational cost and solving a data storage problem (Thrane et al., 2015b). By combining folding with radiometry, we seek to extend the radiometer to carry out a computationally efficient all-sky search.

2.3 Method

In this section we describe a procedure of transforming a gravitational wave strain $s_{1,2}(t)$ measured by two interferometers into the radiometer signal-to-noise ratio, which will serve as the basis for our detection statistic. In subsection 2.3.1 we explain the process of cross-correlation. Subsection 2.3.2 describes an implementation of data folding. In subsection 2.3.3 we apply the directional narrowband radiometer on a folded dataset.

2.3.1 Cross-correlation

Following the procedure from (Thrane et al., 2015b), we divide the data into discrete segments indexed by start time t[2]. There are important considerations that determine a suitable choice of segment duration. On one hand, longer time segments lead to a better frequency resolution. On the other hand longer segment duration decreases search sensitivity at high frequencies due to the rotation of the Earth; see Eq. 12 and the surrounding discussion in (Thrane et al., 2015a). The overall range of frequencies we consider is between 20 Hz and 1800 Hz. In this analysis we pick a segment duration time for the Fourier transformation to be 32 s. This choice guarantees $< 5\%$ decrease in the signal to noise ratio at 1800 Hz due to the rotation of the Earth.

For each segment, we calculate the Fourier transform of the strain time series $\tilde{s}_{1,2}(t,f)$. The subscript refers to the detector number. Noise power spectral densities for each individual detector $P_{1,2}$ are calculated for the background estimation using adjacent time segments. Next, complex-valued estimators $v(t,f)$ and $\sigma(t,f)$ are computed for each sidereal day of the observation:

$$v(t,f) \equiv \frac{1}{N}\tilde{s_1}^*(t,f)\tilde{s_2}(t,f) \in \mathbb{C} \tag{2.1}$$

$$\sigma(t,f) \equiv \frac{1}{2}\sqrt{P_1'(t,f)P_2'(t,f)} \in \mathbb{R} \tag{2.2}$$

$$\rho(t,f) \equiv \frac{v(t,f)}{\sigma(t,f)} \in \mathbb{C} \tag{2.3}$$

The relative difference between the real and the complex part of $v(t,f)$ represents the signal phase information, the absolute value of $v(t,f)$ is the signal strength. Because the background changes with time, $v(t,f)$ is divided by $\sigma(t,f)$ in Equation 2.3.

In Eq 2.1, N is a normalization constant defined in (Ballmer, 2006). It is introduced so that $v(t,f)$ has units of power spectral density. Note that $v(t,f)$ is equivalent to $\mathcal{Y}$ in (Thrane et al., 2015b).

[2]We use the variable t to denote both segment start time and sampling time. The meaning of any particular t should be clear by context.

Next, we apply a coarse-graining operation (Thrane et al., 2015a) by combining neighboring frequency-domain points of $v(t,f)$ and $P^{'}_{1,2}$:

$$v(t,f_{\rm CG}) = \frac{1}{q}\sum_{i=p}^{p+q-1} v(t,f_i) \tag{2.4}$$

$$P^{'}_{1,2}(t,f_{\rm CG}) = \frac{1}{q}\sum_{i=p}^{p+q-1} P^{'}_{1,2}(t,f_i), \tag{2.5}$$

where

$$f_{\rm CG} = \frac{1}{2}\left(f_i + f_{i+q-1}\right). \tag{2.6}$$

Choosing the degree of coarse-graining is a balancing act like choosing the segment duration. If we make the coarse-grained bins too wide, we needlessly add noise on top of the signal. If the coarse-grained bins are too small, the signal may wander outside of the bin. In this analysis, we coarse-grain power spectra from an intrinsic frequency resolution of 1/32 Hz to 1 Hz. When we assume that the signal is narrowband, we mean that the size of the frequency bin is wider than the signal spectrum over the observation time. Spectrum broadening may be caused by Doppler modulation from relative motion of a source of gravitational waves with respect to an observer. Following Dhurandhar and Vecchio (2001), a Doppler shift associated with an orbital motion can be expressed as:

$$\Delta f_{\rm D} \approx \frac{2\pi a \sin\iota}{cP} f_0, \tag{2.7}$$

where f_0 is the gravitational-wave frequency of a source, ι is the orbit inclination angle, a is the semi-major axis, P is the orbital period, c is the speed of light. The Doppler shift associated with sidereal motion of the Earth is then $\Delta f_{\rm D} \sim 10^{-6} f_0$ and the Doppler shift associated with the motion of the Earth around the Sun is $\Delta f_{\rm D} \sim 10^{-4} f_0$. For a neutron star PSR J0636+5129 with a short orbital period of 96 minutes, the data from Manchester et al. (2005) yields $\Delta f_{\rm D} \sim 10^{-6} f_0$. Even for the highest frequency in our analysis $f_0 = 1800$ Hz, $\Delta f_{\rm D}$ discussed above are smaller than the chosen width of the frequency bin of 1 Hz. Spectrum broadening may also be caused by the drift of a gravitational-wave frequency over time. One example is pulsar spin down. Crab pulsar is a neutron star that formed following a supernova that went off back in the year 1024. It has one of the largest measured spin downs $\dot{f}$ of -3.8×10^{-10} Hz/s. The gravitational-wave frequency will shift by around 10^{-2} Hz over the year, which is still smaller than the frequency bin width. Varying the coarse-grained resolution to consider a variety of scenarios is possible, but this lies outside our present scope.

2.3.2 Data folding

Due to the rotation of the Earth, the expectation value of $\rho(t|f)$ for a persistent narrowband signal at a frequency f is a periodic function, with a period equal to one sidereal day. Folding is

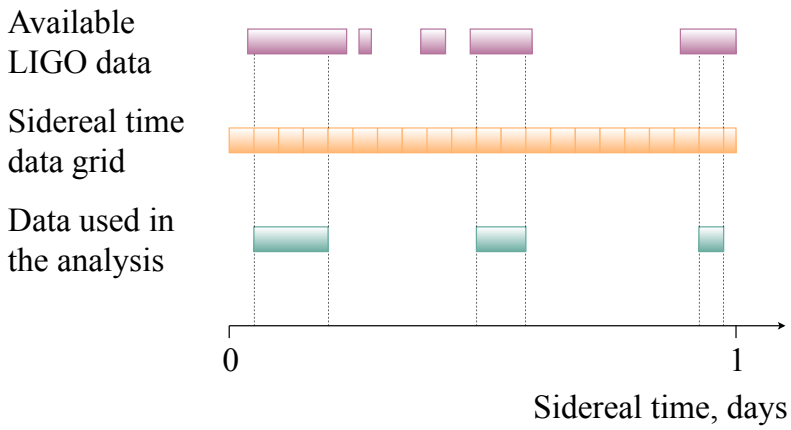

FIGURE 2.1. An illustration of how LIGO data is arranged into segments prior to the folding operation.

a data compression technique that uses this symmetry to transform any dataset into only one sidereal day of data (Ain et al., 2015).

First, we select a GPS time that corresponds to sidereal time = 0 for the first sidereal day. We define an array of evenly-spaced, 32 s segments starting from this zero time. Segments that overlap between sidereal days are removed. The first complete segment in a sidereal day becomes the first segment of that day.

Fragments of data that do not fit into the new time segments are truncated (Figure 2.1). Interferometer lock segments shorter than 700 seconds are removed as well. Applying these cuts to data from LIGO's first observing run, approximately 6% of the data is removed.

Next, following (Thrane et al., 2015b), we sum over sidereal days k in order to fold the data into just one sidereal day $\rho_{\rm fold}(f,t|k)$, using $\sigma(f,t)$ as weight coefficients:

$$v_{\rm fold}(t,f|k) = \frac{\sum_k v_k(t,f)\sigma_k^{-2}(t,f)}{\sum_k \sigma_k^{-2}(t,f)} \tag{2.8}$$

$$\sigma_{\rm fold}(t,f|k) = (\sum_k \sigma_k^{-2}(t,f))^{-\frac{1}{2}} \tag{2.9}$$

$$\rho_{\rm fold}(t,f|k) \equiv \frac{v_{\rm fold}(t,f)}{\sigma_{\rm fold}(t,f)} \tag{2.10}$$

2.3.3 Radiometry

Gravitational-wave radiometry (Ballmer, 2006) has been used in searches for persistent gravitational waves (Abadie et al., 2011; Abbott et al., 2007c, 2017b). The first LIGO radiometer

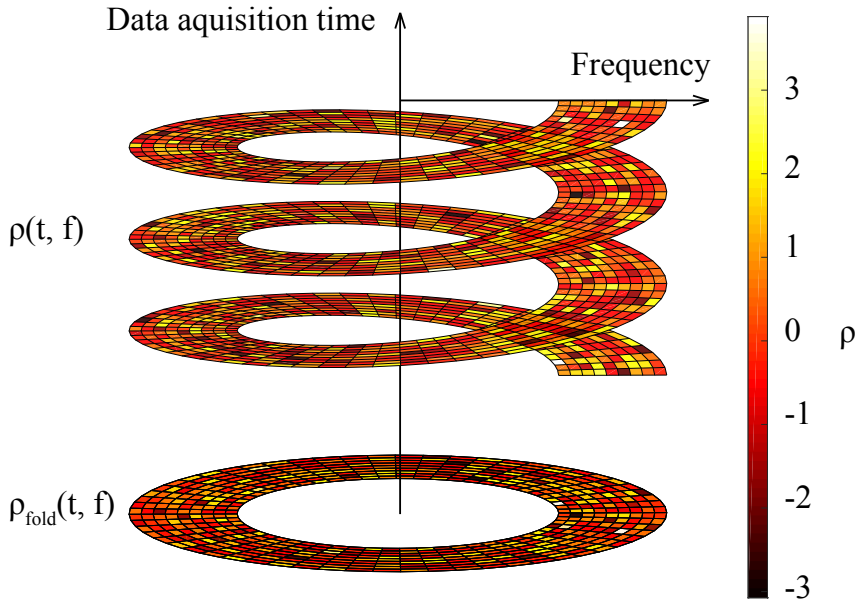

FIGURE 2.2. Representation of data folding. Each element of the helix with a fixed radius represents a real part of the $\rho_{\text{fold}}(t|f)$ data set at a fixed frequency, while each revolution of the helix represents one sidereal day of observations. The ring below the helix represents a folded dataset $\rho_{\text{fold}}(t, f|k)$, where each element is calculated on a basis of the above cells of the helix.

analysis was carried out in 2007 (Abbott et al., 2007c). Narrowband radiometry provides us with a spectrum of a gravitational wave strain data at each sky location. Following (Ballmer, 2006; Thrane et al., 2015b), the signal-to-noise ratio is given by:

$$\text{SNR}(f|\hat{\Omega}) = \frac{\sum_t \text{Re}(\rho_{\text{fold}}(t;f)e^{2\pi i f \hat{\Omega}\cdot\Delta\vec{\mathbf{x}}(t)/c})\epsilon_{12}(t|\hat{\Omega})}{\sqrt{\sum_t \epsilon_{12}^2(t|\hat{\Omega})}} \tag{2.11}$$

Here $\hat{\Omega}$ is the unit vector pointing to the sky position of the source, $\Delta\vec{x}(t)$ is the separation vector of detectors, c is the speed of light, and $\epsilon_{12}(t|\hat{\Omega})$ is the sidereal-time-dependent efficiency factor.

$$\epsilon_{12}(t|\hat{\Omega}) \equiv \frac{1}{2}\sum_A F_1^A(t|\hat{\Omega})F_2^A(t|\hat{\Omega}) \tag{2.12}$$

Here $F_{1,2}^A(t|\hat{\Omega})$ are antennae factors (Hawking and Israel, 1989) for two interferometers; $A = [+, \times]$ are polarization states. The exponential part in Equation 2.11 and $\epsilon_{12}(t|\hat{\Omega})$ are periodic functions of time with a period of one sidereal day.

Previous studies using Monte-Carlo data showed that radiometry with 20 days of folded data can be used to recover persistent gravitational wave signal with a strain amplitude $h_0 = 1.5\times10^{-24}$ at 600 Hz at the LIGO design sensitivity using two detectors with SNR $\approx$ 50 (Thrane et al., 2015b).

2.3.4 Simulated signals

To test the sensitivity of the algorithm, we simulate persistent gravitational waves. Our simulated signals are circularly polarized with a fixed strain amplitude and a sinusoidally evolving phase. The amplitude of the strain measured in each detector is modulated by the antenna factors, which change over the course of the sidereal day due to the rotation of the Earth; see, e.g., (Thrane et al., 2015b). Injections are performed at an arbitrary fixed sky position $(\mathrm{ra}, \mathrm{dec}) = (21\ \mathrm{hr},\ 9^\circ)$. According to Figure 7b from (Thrane et al., 2009), the radiometer sensitivity to strain power, averaged over a sidereal day, varies by about 40% depending on the sky location. Therefore we expect strain amplitude sensitivity to vary by about 20% for different sky locations. The simulated signals are injected into Gaussian noise corresponding to Advanced LIGO at design sensitivity (Harry et al., 2010). Technically, in order to simulate a signal with the characteristics of a continuous wave source in a binary, one ought to include time-dependent Doppler modulation. However, we ignore this effect in our simulation since our frequency bins are typically much wider than the expected Doppler modulation from binary motion.

2.4 Data quality

Advanced LIGO comprises two detectors at Hanford and Livingston in the USA, and its first observing run (O1) took place between September 12, 2015 and January 19, 2016. It is necessary to remove instrumental lines to avoid false positives. We provide a three-step technique to remove noise artifacts without accidentally removing an astrophysical signal.

The first step is to remove known instrumental lines from the frequency domain. We employ a list of lines from the recent directed search for persistent gravitational waves using radiometry (Abbott et al., 2017b).

The second step is to remove times associated with non-stationary noise (glitches). Since we are looking for a weak, persistent signal, we employ a relatively robust time-domain cut without fear of throwing out the signal. Our time-domain cut eliminates any times that contain $N_\rho = 6$ or more $\rho(t,f)-$spectrogram pixels with $\rho > (\rho_{\mathrm{max}} = 7)$. This cut removes on average 0.5% of O1 data (Figure 2.6(a)) and none of Monte-Carlo data.

While the first cut eliminates known lines (instrumental artifacts with known origins), there are additional "unknown" lines that we remove because they do not match our signal model. The next step is to remove these unknown lines. We apply an additional cut that eliminates any $\rho(t,f)-$spectrogram pixels with $\rho > \rho_{\mathrm{max}}$. This cut removes on average 0.3% of the remaining O1 data and 0.1% of the remaining Monte-Carlo data. The values of N_ρ and ρ_{max} are chosen to produce real-data distributions of $\rho(t,f)$ that are comparable to distributions generated from Gaussian noise.

Next, we look at the standard deviation of $\rho_{\text{fold}}(t|f,k)$ with respect to sidereal time,

$$\text{std}_t[\rho_{\text{fold}}(t|f,k)]. \tag{2.13}$$

While high values of ρ_{fold} can be evidence of a signal, large *scatter* in the values of $\rho(t,f)$ is more likely to be due to a detector artifact. We calculate the standard deviation in for each frequency bin as per Eq. 2.13. Using injection studies, we set a maximum threshold on the standard deviation, which we denote σ_{crit}. We determine that $\sigma_{\text{crit}} = 1.7$ is a suitable choice for vetoing instrumental artifacts while preserving signals. This is illustrated in Fig. 2.3 and Fig. 2.6(b). We plot the signal-to-noise ratio, maximized over all sky directions

$$\text{SNR}(f) = \max_{\hat{\Omega}} \text{SNR}(f|\hat{\Omega}), \tag{2.14}$$

versus the standard deviation of ρ_{fold} defined in Eq. 2.13. Dots represent data from different frequency bins. Red represents time-shifted O1 data, blue represents Monte-Carlo noise, and green represents injected signals in Monte-Carlo noise. The time-shifted data is obtained by assuming the measurements from the Livingston detector took place 1 second later than in reality. This way, we capture features of real noise processes in the data, while removing any information about astrophysical signals that may be present. If the data falls into the red zone on the plot, it gets vetoed.

In addition to the above veto test using circularly-polarized signals, we perform an additional veto test using a linearly-polarized signal with an inclination angle of $\iota = 90°$ and a polarization angle of $\psi = 0°$. By varying the integration time, we recover the signal multiple times with an SNR between 4 and 50 at the injection frequency and sky location. The veto threshold σ_{crit} for the linearly-polarized signal is not exceeded.

2.5 Detection statistic

The goal of this section is to design a statistic for identifying the brightest point source on the sky and determining the associated statistical significance.

First, we find the brightest patch in the sky for all frequency bins, which we denoted SNR(f). In this work we probe 360 equally-spaced azimuthal components of angle $\hat{\Omega}$ times 180 equally-spaced polar components for a a total of 64800 sky locations.

Next, we look for the frequency bin with the most significant SNR(f). Naively, one might expect that this is accomplished by choosing the maximum of SNR(f) over all frequencies. However, this naive method for finding the loudest frequency bins presumes that the noise distribution of SNR(f) is independent of frequency. In reality, the distribution changes as a function of frequency due to the fact that the diffraction limited resolution δ_θ is a function of frequency:

$$\delta_\theta \approx \frac{c}{f}\frac{1}{\Delta\vec{x}(t)} \approx \left(\frac{1000\text{ Hz}}{f}\right) 5° \tag{2.15}$$

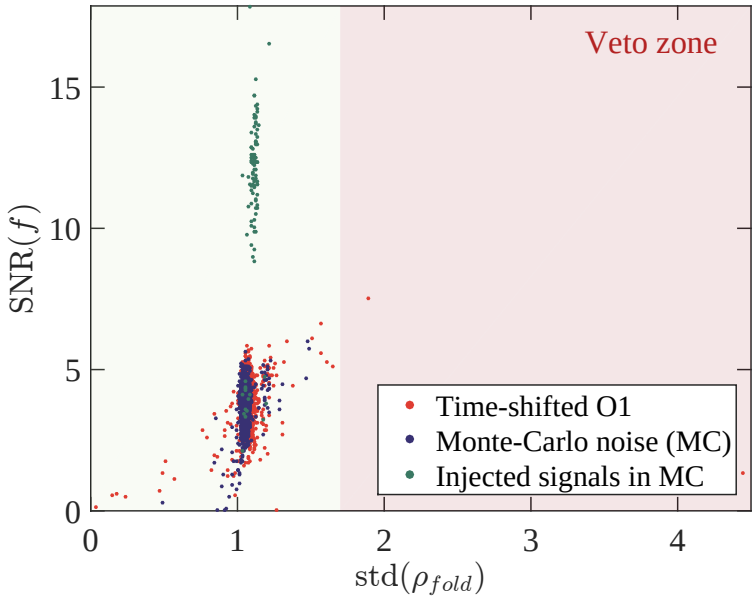

FIGURE 2.3. The standard deviation of $\rho_{\text{fold}}(t|f,k)$ on the x-axis is used to veto frequency-domain data. The signal-to-noise ratio SNR(f) on the y-axis quantifies significance. Some frequency bins in the time-shifted O1 data (red) with a high $\rho_{\text{fold}}(t|f,k)$ in the veto zone of the plot would provide a great SNR($f|\hat{\Omega}$) if the veto were not applied.

At high frequencies, there is a relatively higher number of effective sky locations. Since there are more effective sky locations, fluctuations in the noise lead to greater SNR(f) due to a trial factor effect. We therefore must define a new statistic in order to avoid a preference for higher frequency signals.

Our solution is to define a new statistic $\lambda(f)$, which rescales SNR(f) to take into account the frequency dependence of the diffraction limited resolution:

$$\lambda(f) \equiv \frac{\max_{\hat{\Omega}} \text{SNR}(f,\hat{\Omega}) - \mu_{\text{fit}}(f)}{\sigma_{\text{fit}}(f)}. \tag{2.16}$$

The functions $\sigma_{\text{fit}}(f)$ and $\mu_{\text{fit}}(f)$ are measured empirically with simulations so that $\lambda(f)$ is approximately flat in frequency when we analyze noise. The final detection statistic is

$$\lambda \equiv \max_{f} \lambda(f). \tag{2.17}$$

To assign a statistical significance to λ, we perform background simulations to generate a distribution of $\{\lambda_i\}$. For each realization, we simulate an array of folded data $\rho^i_{\text{fold}}(t,f)$. Every (t,f) pixel is drawn from a normal distribution with mean=zero and with a variance determined from time-shifted data. While individual segments of data are known to exhibit non-Gaussian noise, we expect that folded data to be nearly Gaussian distributed due to the central limit theorem. This assumption is supported by previous cross-correlation analyses, e.g., (Aasi et al.,

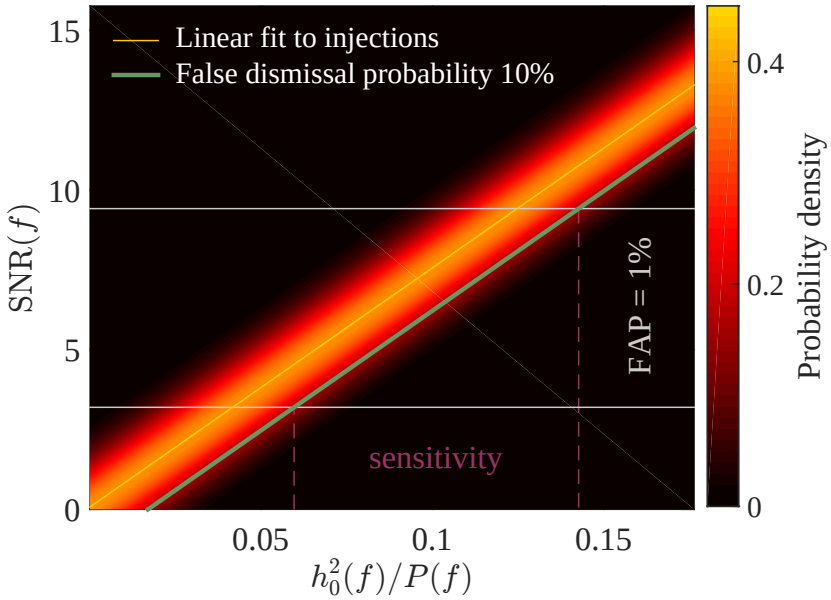

FIGURE 2.4. Signal-to-noise ratio at the sky location where the signal was injected as a function of the effective injected signal to noise ratio.

2014; Abadie et al., 2011, 2012; Abbott et al., 2004, 2007a,d, 2017b,c). We carry out $N_{\rm sim} = 10^5$ background realizations. The false alarm probability (FAP) of λ is given by:

$$\mathrm{FAP}(\lambda) = \frac{N(\lambda_i \geq \lambda)}{N_{\rm sim}}, \tag{2.18}$$

where $N(\lambda_i \geq \lambda)$ is the number of simulated backgrounds that exceed λ (the measured detection statistic). In the remainder of the paper, we set FAP = 1% as a fiducial threshold for identification of a statistically interesting signal. We find that FAP = 1% corresponds to a lambda value of $\lambda_0 = 7.6$.

2.6 Sensitivity calculation

In this section, we estimate the gravitational-wave strain amplitude $h_0(f)$ that we can detect with false alarm probability FAP = 1% and false dismissal probability FDP = 10%. Our simulated signals are described in Section 2.3.4. For each frequency bin, we vary h_0 and determine the value such that we exceed the FAP = 1% threshold λ_0 at least $1 - \mathrm{FDP} = 90\%$ of the time.

In Figure 2.4, we plot the recovered signal-to-noise ratio $\mathrm{SNR}(f|\hat{\Omega}_0)$ as a function of the effective injected signal-to-noise ratio $h_0^2(f)/P(f)$. The recovered signal-to-noise ratio is linearly proportional to the injected signal-to-noise ratio:

$$\mathrm{SNR}_m(f) = a\frac{h_0^2(f)}{P(f)}, \tag{2.19}$$

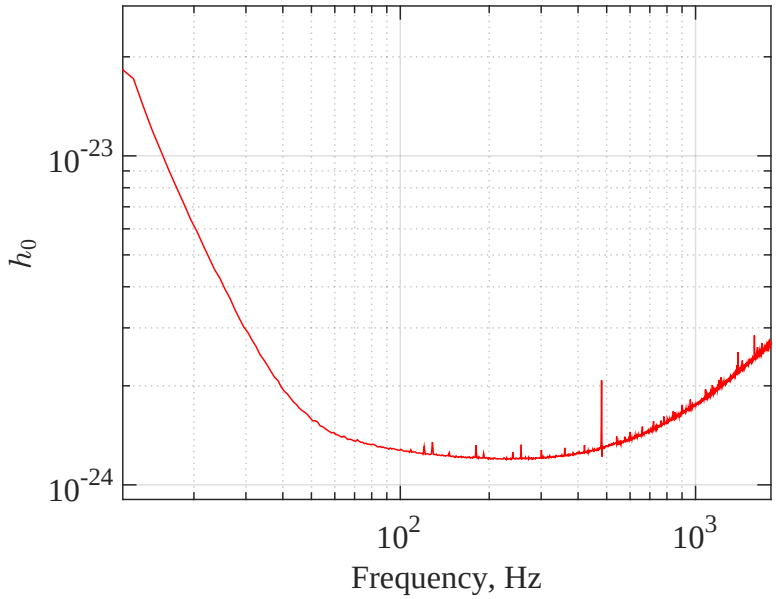

FIGURE 2.5. Sensitivity to the strain amplitude $h_0(f)$ for 2 folded days of the Monte-Carlo background $\rho_{\text{fold}}(t, f|k)$ for LIGO at design sensitivity. We assume 1% FAP and 10% FDP.

where a depends on details of the windowing procedure, but for our choice of parameters, $a = 74.9$. For a fixed *injected* signal-to-noise ratio, there is a distribution of *recovered* signal-to-noise ratios, the width of which is indicated in Fig. 2.4 by the yellow-orange band. The requirement that the false dismissal probability is FDP = 10% can be visualized using the green line, below which 10% of the injections are recovered for a fixed value of h_0^2/P. We define Δ as the vertical distance between the yellow and green lines; it is the difference in SNR required to go from FDP = 50% to FDP = 10%. The strain amplitude sensitivity is

$$h_0 = \sqrt{\frac{P(f)}{a}\Big(\text{SNR}_0(f) - \Delta\Big)}, \tag{2.20}$$

where $\text{SNR}_0(f)$ is the threshold for a statistically significant signal-to-noise ratio given λ_0. That is,

$$\text{SNR}_0(f) = \sigma_{\text{fit}}(f)\lambda_0 + \mu_{\text{fit}}. \tag{2.21}$$

Our results are summarized in Fig. 2.5. At the most sensitive frequency bin, corresponding to $f = 245$Hz, the strain amplitude sensitivity is $h_0 = 1.3 \times 10^{-24}$. For the current analysis with ≈ 2 sidereal days of Monte-Carlo noise at the level of LIGO design sensitivity we used a total of 4650 time segments 32 seconds long. The signal-to-noise ratio scales like $\text{SNR}(f|\hat{\Omega}) \propto \sqrt{t_{\text{obs}}}$ (Thrane et al., 2015b). At $f = 600$Hz we project the strain amplitude sensitivity $h_0 \approx 3.9 \times 10^{-25}$, for a two-detector network operating at the level of LIGO design sensitivity for one year. This prediction is the same order of magnitude as in (Thrane et al., 2015b) ($h_0 \approx 2 \times 10^{-25}$). For analysis of LIGO's

O1 run we project a strain amplitude sensitivity $h_0 \approx 1.2 \times 10^{-24}$ at $f = 245$ Hz. The expected sensitivity for linearly-polarized signals is expected to be worse by a factor of approximately 2.6 (Messenger, 2010).

We compare this result to upper limits from recent searches for continuous and persistent gravitational radiation with LIGO's O1 data. All-sky searches for continuous, nearly-monochromatic circularly-polarized gravitational waves in the 20-475 Hz band reported 95% confidence upper limits that reach $h_0 \approx 1.5 \times 10^{-25}$ in the 150 - 250 Hz region (Abbott et al., 2017f). Directional radiometer search using LIGO's O1 data provides 90% confidence upper limits on persistent gravitational waves, reaching $h_0 \approx 4.0 \times 10^{-25}$ (Abbott et al., 2017b).

2.7 Conclusion

We apply an all-sky radiometer algorithm to simulated Gaussian noise, which has been compressed using sidereal-day folding. The data are cleaned using a data-quality procedure developed with time-shifted data from LIGO's first observing run. We project that the algorithm achieves a strain amplitude sensitivity of $\approx 1.2 \times 10^{-24}$ (1% false alarm probability, 10% false dismissal probability) for a two-detector network operating at design sensitivity for the time of the LIGO first observing run O1. This corresponds to a sensitivity to neutron star ellipticity of (Abbott et al., 2007b)

$$\epsilon \approx 6 \times 10^{-5} \left(\frac{0.4}{\beta}\right) \left(\frac{10^{45}\ \mathrm{g\ cm^2}}{I}\right) \left(\frac{r}{10\ \mathrm{kpc}}\right) \left(\frac{600\ \mathrm{Hz}}{f}\right)^2, \tag{2.22}$$

where β is an orientation factor, G is the gravitational constant, r is the distance to the source, and I is the moment of inertia. Because the radiometer works with a simplified signal model with no regard to distance parameters, binary parameters and neutron star spin frequency derivatives, it is always less sensitive to classical continuous-wave signals than matched-filter searches. On the other hand, it is not clear to what extent these theoretical models represent real neutron-star gravitational waves.

At some point in the future, the amount of collected data will make even the directional radiometer computationally challenging. So, data folding may be the only convenient way to perform these searches. Data folding can also be applied to searches for the stochastic gravitational-wave background. With that, several improvements for narrowband searches with folded data can be implemented in the future. Varying the coarse-grained frequency bin width can be used to achieve an optimal sensitivity for simulated signals. Computational improvements for data folding have been suggested (Ain et al., 2018) as well.

2.8 Acknowledgements

We appreciate the help of Sharan Banagiri, Patrick Meyers and Michael Coughlin during the process of data analysis software development. We also thank Anirban Ain, Jishnu Suresh,

Andrew Matas, and Sanjit Mitra for discussions regarding data folding. The authors thank to the LIGO Scientific Collaboration for access to the data and gratefully acknowledge the support of the United States National Science Foundation (NSF) for the construction and operation of the LIGO Laboratory and Advanced LIGO as well as the Science and Technology Facilities Council (STFC) of the United Kingdom, and the Max-Planck-Society (MPS) for support of the construction of Advanced LIGO. Additional support for Advanced LIGO was provided by the Australian Research Council. BG and ET are supported by ARC CE170100004. ET is additionally supported by ARC FT150100281. This manuscript is LIGO-P1800105.

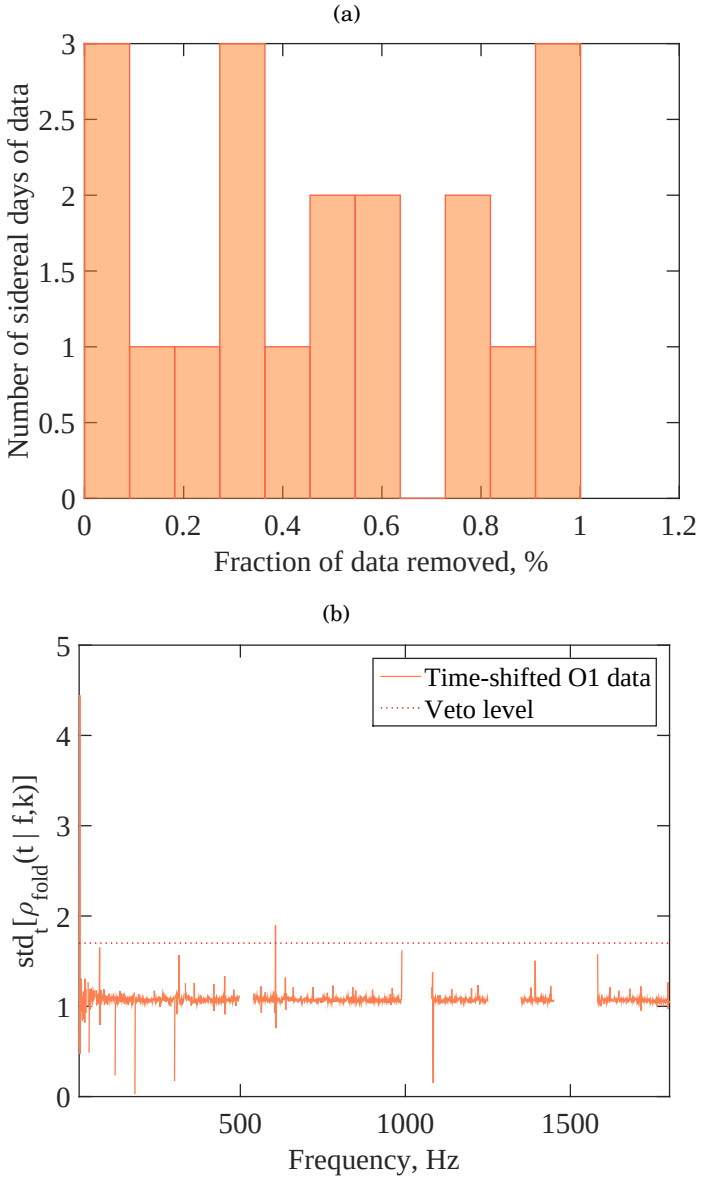

FIGURE 2.6. Figure 2.6(a) represents amounts of data removed from 14 days of time-shifted LIGO O1 data on the second data quality cut, described in Section 2.4, that removes time segments. Figure 2.6(b) represents the standard deviation of $\rho_{\text{fold}}(t|f,k)$ for time-shifted data from LIGO's O1 run.

CHAPTER 3

Is there a spectral turnover in the spin noise of millisecond pulsars?

Submitted manuscript:
Goncharov, B., Zhu, X. J., & Thrane, E. (2019). Monthly Notices of the Royal Astronomical Society.

Pulsar timing arrays provide a unique means to detect nanohertz gravitational waves through long-term measurements of pulse arrival times from an ensemble of millisecond pulsars. After years of observations, some timing array pulsars have been shown to be dominated by low-frequency red noise, including spin noise that might be associated with pulsar rotational irregularities. The power spectral density of pulsar timing red noise is usually modeled with a power law or a power law with a turnover frequency below which the noise power spectrum plateaus. If there is a turnover in the spin noise of millisecond pulsars, residing within the observation band of current and/or future pulsar timing measurements, it may be easier than projected to resolve the gravitational-wave background from supermassive binary black holes. Additionally, the spectral turnover can provide valuable insights on neutron star physics. In the recent study by Melatos and Link, the authors provided a derivation of the model for power spectral density of spin noise from superfluid turbulence in the core of a neutron star, from first principles. The model features a spectral turnover, which depends on the dynamical response time of the superfluid and the steady-state angular velocity lag between the crust and the core of the star. In this work, we search for a spectral turnover in spin noise using the first data release of the International Pulsar Timing Array. Through Bayesian model selection, we find no evidence

of a spectral turnover. Our analysis also shows that data from pulsars J1939+2134, J1024−0719 and J1713+0747 prefers the power-law model to the superfluid turbulence model.

3.1 Introduction

It has long been proposed that pulsars can be used to detect gravitational waves in the nHz band (Detweiler, 1979; Hellings and Downs, 1983; Sazhin, 1978). Millisecond pulsars, first discovered in 1982 (Backer et al., 1982), provide promising prospects for gravitational wave detection thanks to their exceptional rotational stability. The concept of a pulsar timing array (PTA), long-term monitoring of pulse arrival times from a spatial array of millisecond pulsars, was conceived three decades ago (Foster and Backer, 1990a; Romani, 1989). Currently, several collaborations are conducting PTA observations, including the Parkes Pulsar Timing Array (PPTA) (Manchester et al., 2013), the European Pulsar Timing Array (EPTA) (Kramer and Champion, 2013) and the North American Nanohertz Observatory for Gravitational Waves (NANOGrav) (McLaughlin, 2013a). A consortium of these collaborations is called the International Pulsar Timing Array (IPTA) (Hobbs et al., 2010a; Perera et al., 2019).

The first gravitational-wave signal detected with PTAs is likely to be a stochastic gravitational-wave background, formed by a cosmic population of supermassive binary black holes (Rosado et al., 2015). Apart from the detection of gravitational waves, PTAs also offer the opportunity to establish a pulsar-based time standard (Hobbs et al., 2012), to study the Solar System (Caballero et al., 2018), the interstellar medium (Coles et al., 2015) and the Solar wind (Madison et al., 2019), and to constrain ultralight dark matter candidates (Porayko et al., 2018).

The science output of PTA data relies on how well we model noise. Incorrect noise models can also lead to false detection in gravitational-wave searches (Arzoumanian et al., 2018a; Hazboun et al., 2020). At low frequencies, where we are most sensitive to the stochastic gravitational-wave background, some millisecond pulsars, primarily studied in the PTA context, have measureable levels of red noise (Arzoumanian et al., 2015a, 2018b; Caballero et al., 2016; Coles et al., 2011; Lentati et al., 2016; Reardon et al., 2016). The red noise power spectrum is modelled by either a power law, or the broken power law, which introduces a corner frequency below which the noise power spectrum plateaus. Additional opportunities also include the free spectral model (see, e.g., Lentati et al., 2013) and the power-law model with deviations at each frequency bin (Caballero et al., 2016). One particular source of red noise is the spin noise, which might be associated with pulsar rotational irregularities (see, e.g., Shannon and Cordes, 2010). While some young pulsars show hints of a spectral turnover at low frequencies (Parthasarathy et al., 2019), it has not yet been found for millisecond pulsars. If the typical time scale of a spectral turnover for millisecond pulsars is on the order of years or shorter, it reduces the red noise in the most sensitive frequency band of PTAs, yielding a faster detection of a stochastic gravitational-wave background. Implications of how a spectral turnover will affect times to detection of a stochastic

background were discussed in Lasky et al. (2015). One of the conclusions of Lasky et al. (2015) is that the gravitational wave power spectrum will only surpass the steeper timing noise spectrum if the latter flattens below some frequency.

Moreover, pulsar timing red noise provides interesting prospects for studying neutron star physics. A range of mechanisms have been proposed to explain pulsar red noise, including switching between two different spin-down rates (Lyne et al., 2010), recovery from a glitch – a sudden increase in the rotational frequency (Johnston and Galloway, 1999a), a cumulative effect of frequent micro-glitches (Cordes and Downs, 1985; D'Alessandro et al., 1995; Melatos et al., 2008), variable coupling between the crust and liquid interior (Alpar et al., 1986; Jones, 1990), influence of planets (Cordes, 1993) and asteroids (Shannon et al., 2013). Nevertheless, there are not many models that link power spectral density model parameters to physical features. One such model by Melatos and Link (2013), which we explore in this paper, predicts a superfluid turbulence in neutron star interiors as the origin of red noise. The turbulent process exerts a torque on the star's crust, where the external magnetic field of the star is produced. The model features a spectral turnover.

In this work we employ Bayesian inference to search for evidence of spectral turnover in pulsar spin noise in the first data release (DR1) of the IPTA (Verbiest et al., 2016). We discuss our data analysis methods in Section 3.2. Our simulation study is presented in Section 3.3. We describe the noise processes of the first IPTA data release in Section 3.4. We present the results in Section 3.5, and discuss our conclusions in Section 3.6.

3.2 Method

3.2.1 Bayesian methodology in pulsar timing

First, following Van Haasteren et al. (2009), we assume a multivariate Gaussian likelihood function to describe pulsar timing residuals $\boldsymbol{\delta t}$ after fitting for the timing model:

$$\mathscr{L}(\boldsymbol{\delta t}|\boldsymbol{\theta},\boldsymbol{\xi}) = \frac{1}{\sqrt{(2\pi)^n \det(\boldsymbol{C})}} \exp\left(-\frac{1}{2}(\boldsymbol{\delta t}-\boldsymbol{s}-\boldsymbol{M}\boldsymbol{\xi})^{\mathrm{T}}\boldsymbol{C}^{-1}(\boldsymbol{\delta t}-\boldsymbol{s}-\boldsymbol{M}\boldsymbol{\xi})\right). \tag{3.1}$$

Stochastic signals are modeled using a covariance matrix $\boldsymbol{C}$, while $\boldsymbol{s}$ is a deterministic signal vector. For n pulse times of arrival, $\boldsymbol{s}$ has dimensions of $1 \times n$ and $\mathbf{C}$ has dimensions of $n \times n$. Thus, values of $\boldsymbol{s}$ are expected amplitudes of a signal in seconds at observation times. Values of $\boldsymbol{C}$ effectively represent stochastic process amplitudes at different time scales. Parameters of our models are $\boldsymbol{\theta}$. The vector $\boldsymbol{\xi}$ contains timing model parameters and $\boldsymbol{M}$ is a design matrix, describing the contribution of m timing model parameters to n times of arrivals (ToA). Among timing model parameters are pulsar barycentric rotation frequency (F0) and its time derivatives

(F1, F2), dispersion measure (DM) and its time derivative (DM1), distance parameters and binary parameters, if pulsar is in a binary system. Timing model parameters are obtained with least-squares fitting prior to the analysis. Estimates of timing model parameters are contained in data files with .par extension. Pulse times of arrival at the observatory are contained in data files with extension .tim. Throughout our study, we work with ToAs and residuals, referenced to the Solar System Barycenter. Assuming uniform prior on timing model parameters, the likelihood is marginalized over these parameters (Van Haasteren et al., 2009):

$$\mathscr{L}(\boldsymbol{\delta t}|\boldsymbol{\theta}) = \frac{\sqrt{\det(\boldsymbol{M}^{\mathrm{T}}\boldsymbol{C}^{-1}\boldsymbol{M})^{-1}}}{\sqrt{(2\pi)^{n-m}\det(\boldsymbol{C})}} \exp\left(-\frac{1}{2}(\boldsymbol{\delta t}-\boldsymbol{s})^{\mathrm{T}}\boldsymbol{C}'(\boldsymbol{\delta t}-\boldsymbol{s})\right), \tag{3.2}$$

where we have defined

$$\boldsymbol{C}' = \boldsymbol{C}^{-1} - \boldsymbol{C}^{-1}\boldsymbol{M}(\boldsymbol{M}^{T}\boldsymbol{C}^{-1}\boldsymbol{M})^{-1}\boldsymbol{M}^{T}\boldsymbol{C}^{-1}\,. \tag{3.3}$$

To speed up the calculation, we employ the singular value decomposition of the design matrix in the form $\boldsymbol{M} = \boldsymbol{USV}^*$, where $\boldsymbol{S}$ contains singular values of $\boldsymbol{M}$, $\boldsymbol{U}$ and $\boldsymbol{V}$ are unitary matrices with dimensions $n \times n$ and $m \times m$ respectively. Then we obtain the likelihood function in a form (van Haasteren and Levin, 2013)

$$\mathscr{L}(\boldsymbol{\delta t}|\boldsymbol{\theta}) = \frac{1}{\sqrt{(2\pi)^{n-m}\det(\boldsymbol{G}^{T}\boldsymbol{C}\boldsymbol{G})}} \exp\left(-\frac{1}{2}(\boldsymbol{\delta t}-\boldsymbol{s})^{T}\boldsymbol{G}(\boldsymbol{G}^{T}\boldsymbol{C}\boldsymbol{G})^{-1}\boldsymbol{G}^{T}(\boldsymbol{\delta t}-\boldsymbol{s})\right), \tag{3.4}$$

so that $\boldsymbol{U} = \boldsymbol{U_1}\boldsymbol{G}$ with $\boldsymbol{U_1}$ and $\boldsymbol{G}$ consisting of the first m and remaining $n-m$ columns of $\boldsymbol{U}$.

Some timing model processes are covariant with red noise. In particular, in analyses by Coles et al. (2011) and Reardon et al. (2016), the least-squares timing model fit absorbs some red noise. This absorption of power causes an apparent visible turnover in the measured spectra of red post-fit residuals, which is why the model with the broken power law was used for these analyses. In Caballero et al. (2016), the regular power-law was used, as the effects of timing model fitting were taken into account. In our analysis, we employ analytical marginalization over the uncertainty of timing model parameters in Equation 3.4, which is equivalent to the simultaneous fitting of the timing model parameters and the red noise parameters, under the assumption that non-linear dependencies of the likelihood on the timing model parameters are negligible. This avoids the problem of detecting a spectral turnover that is actually due to the timing model fit, and makes it possible to target the spectral turnover in the spin noise itself. During marginalization, one loses sensitivity at low frequencies, especially at frequencies $\leq 1/T_{\mathrm{obs}}$, due to taking the uncertainty of the timing model into account.

Our prior probability distribution is $\pi(\boldsymbol{\theta})$. The integral of the likelihood times the prior over the prior parameter range is the Bayesian evidence for our model:

$$\mathscr{Z}(\boldsymbol{\delta t}) = \int \mathscr{L}(\boldsymbol{\delta t}|\boldsymbol{\theta})\pi(\boldsymbol{\theta})d\boldsymbol{\theta}. \tag{3.5}$$

To infer our model parameters $\boldsymbol{\theta}$, given observational data, we employ the Bayes' theorem:

$$\mathscr{P}(\boldsymbol{\theta}|\boldsymbol{\delta t}) = \frac{\mathscr{L}(\boldsymbol{\delta t}|\boldsymbol{\theta})\pi(\boldsymbol{\theta})}{\mathscr{Z}(\boldsymbol{\delta t})}. \tag{3.6}$$

Using two different models A and B with parameters $\boldsymbol{\theta}_{\rm A}$ and $\boldsymbol{\theta}_{\rm B}$, we employ the Bayes factor as a measure of which model better fits the data:

$$\mathscr{B}^{\rm B}_{{\rm A},i} = \frac{\mathscr{Z}^{\rm B}_i(\boldsymbol{\delta t})}{\mathscr{Z}^{\rm A}_i(\boldsymbol{\delta t})},\ i \in [1, N_{\rm psr}]\,, \tag{3.7}$$

where $N_{\rm psr}$ is the number of pulsars. In Bayesian model selection, it is advised to use the posterior odds ratio as the decisive criterion for model comparison. Posterior odds ratio is equal to the Bayes factor times the prior odds ratio. In our model selection, we do not know a-priori whether the spectral turnover will ever be detected in millisecond pulsars. So, we choose prior odds to be equal to one. Thus, the posterior odds ratio is equal to the Bayes factor. For simulation studies, we calculate the Bayes factors from evidence, which is obtained with nested sampling (Skilling, 2004). To save on computational cost, we adopt the product-space sampling method (Carlin and Chib, 1995; Hee et al., 2015) to calculate Bayes factors for the real data[1]. Both methods are mathematically equivalent. Assuming timing data for each pulsar are independent measurements, we combine all available data:

$$\mathscr{B}^{\rm B}_{\rm A} = \prod_{i=1}^{N_{\rm psr}} \mathscr{B}^{\rm B}_{{\rm A},i}\,, \tag{3.8}$$

which provides a metric to determine whether the spectral turnover is a real physical feature of millisecond pulsar spin noise. For a discussion of how Bayes factors are combined through multiplication, see, for example, Zimmerman et al. (2019). The authors argued that this approach is a limiting case of the inference of hyper-parameters that characterize the underlying distributions of parameters of individual events (pulsars), under the assumption that measurements of these parameters are independent. We interpret Bayes Factors, as in Kass and Raftery (1995), where $0 \leq \log\mathscr{B} < 1$ is not worth more than a bare mention, $1 \leq \log\mathscr{B} < 3$ is positive, $3 \leq \log\mathscr{B} < 5$ is strong, and $\log\mathscr{B} \geq 5$ is very strong.

3.2.2 Modelling stochastic processes

We model stochastic red noise processes as a power-law power spectral density $P(f)$. We include $P(f)$ in our likelihood function using the Fourier-sum method from Lentati et al. (2013), described briefly below. We represent the covariance matrix as $\boldsymbol{C} = \boldsymbol{N} + \boldsymbol{K}$, where $\boldsymbol{N}$ is a diagonal matrix for white noise component, and $\boldsymbol{K}$ is a red noise component. A Woodbury lemma is used to simplify

[1]The technical inconvenience of this method - one has to choose the set of compared models before the sampling starts - is the main reason to adopt nested sampling for our simulation studies.

the inversion of a covariance matrix, decomposed into $\boldsymbol{N}$ and $\boldsymbol{K}$ (Hager, 1989; van Haasteren and Vallisneri, 2014). We define a Fourier basis $\boldsymbol{F}$ with elements:

$$F_{i,j} = \begin{cases} \kappa_j \, a_i \, \sin\left(2\pi f_i \Delta t_j\right), & i \text{ is even} ; \\ \kappa_j \, b_i \, \cos\left(2\pi f_i \Delta t_j\right), & i \text{ is odd} ; \end{cases} \tag{3.9}$$

$$i \in [1, 2N_{\rm F}], \; j \in [1, N_{\rm ToA}] \, .$$

The parameter κ is a constant, which we reserve to model chromatic red noise that depends on a radio frequency. For spin noise, κ is equal to one. The multiplicative factors a_i and b_i are Fourier coefficients which follow the standard Gaussian distribution. Each $\Delta t_j = (t_j - t_1)$ is the difference between the first ToA and the $j^{\rm th}$ ToA. The elements f_i are components of a frequency vector that depend on the total observation span $T_{\rm obs}$. They are defined as

$$f_i = \begin{cases} \frac{i+1}{2T}, & i \text{ is odd} ; \\ \frac{i}{2T}, & i \text{ is even} . \end{cases} \tag{3.10}$$

The variable $N_{\rm F}$ determines the number of Fourier basis components in the frequency domain, with a minimum of $1/T_{\rm obs}$ and spacing $\Delta f = 1/T_{\rm obs}$. Next, we obtain a diagonal matrix $\boldsymbol{\Phi}(\boldsymbol{\theta}_{\rm red})$ with elements $\Phi_i = P(f_i)$, which depends on our red noise model with parameters $\boldsymbol{\theta}_{\rm red}$. Note, the minimum f_i is sometimes referred to as the low-frequency cut-off, although it is not necessarily assumed that there is no red noise power below this frequency. Essentially, the data are just not analyzed below f_i. In principle, the low-frequency cut-off can become a free parameter of our model (see, e.g., Lentati et al., 2014). This approach could potentially reveal the sudden drop of power at low frequencies. The red noise component in our likelihood function, marginalized over Fourier coefficients a_i and b_i (van Haasteren and Vallisneri, 2014), is

$$\boldsymbol{K} = \boldsymbol{F}\boldsymbol{\Phi}\boldsymbol{F}^{\rm T} \, \Delta f \, . \tag{3.11}$$

The white-noise covariance matrix $\boldsymbol{N}$ is diagonal with elements

$$\sigma_j^2 = (\text{EFAC} \, \sigma_j^{\rm ToA})^2 + \text{EQUAD}^2 \, , \tag{3.12}$$

where EFAC and EQUAD are factors to account for the excess of white noise, in addition to ToA error bars, $\sigma_j^{\rm ToA}$. When $\sigma_j^{\rm ToA}$ represent white noise well, EFAC is one and EQUAD is zero.

3.2.3 Red noise models

Some millisecond pulsars in real data do not show evidence of red noise (e.g., Lentati et al., 2016). We refer to the model without red noise as "Model ∅". Next, we employ the two following phenomenological models for red noise. The power-law model

$$P_{\rm PL}(f) = \frac{A^2}{12\pi^2} \text{yr}^3 (f \text{ yr})^{-\gamma}, \tag{3.13}$$

which we refer to as the "Model PL". And the broken power-law model

$$P_{\rm BPL}(f) = \frac{A^2}{12\pi^2}{\rm yr}^3(\sqrt{f^2+f_{\rm c}^2}\ {\rm yr})^{-\gamma}, \tag{3.14}$$

which we refer to as "Model BPL". In the above two equations, model parameters are: the red noise amplitude A, the slope γ, the corner frequency $f_{\rm c}$.

We also study the superfluid turbulence model from (Melatos and Link, 2013)

$$P_{\rm M}(f) = \frac{15p^2}{8\pi\lambda^2\eta(R^{-1})}\int_{2\pi}^{\infty}\frac{x^4+3x^2+9}{[\frac{2\pi f}{\eta(R^{-1})}]^2+x^{4/3}}x^{-31/3}dx, \tag{3.15}$$

which we refer to as "Model M". The model depends on parameters $\eta(R^{-1})$ and λ. Our Equation 3.15 is obtained by multiplying the power spectral density defined in Equation 16 of Melatos and Link (2013) with pulsar spin period squared p^2. This way, we obtain the power spectral density in units of $[s^3]$, to be consistent with Equations 3.13 and 3.14. Parameter λ is a non-condensate fraction of the moment of inertia, which affects the amplitude of red noise. Parameter $\eta(R^{-1})$ is a decorrelation frequency, which determines the spectral turnover. Whereas theory provides some predictions for λ (see, e.g., Van Eysden and Melatos, 2010), $\eta(R^{-1})$ is poorly understood. Thus, the amplitude of spin noise remains very loosely constrained by theory. For convenience, we reparametrize Equation 3.15, in the form of parameters M and $t_{\rm c}$, using Equation A.1. The integral in Equation 3.15 yields an analytical solution, given by Equation A.2. It is possible that only certain values of the (λ, $\eta(R^{-1})$) parameters are allowed by neutron star physics, which could motivate a different prior for (λ, $\eta(R^{-1})$) in future work.

In Figure 3.1, we plot examples of models of spin noise power spectral density. Note, at high frequencies, Model M with two parameters asymptotically approaches Model PL with fixed $\gamma = 2$ and only one free parameter (amplitude), so parameters $\eta(R^{-1})$ and λ of Model M become degenerate. In order to break this degeneracy, and to distinguish models PL and M, one must observe a spectral turnover. This conclusion will be important later when we find pulsars that prefer Model M over Model PL, but realize that at the current stage of observations the performance of Model M is largely determined by the consistency of Model PL's estimate of γ with 2.

In our analysis, we model $N_{\rm F} = 30$ Fourier components of red noise processes. For power-law $P(f)$, the fraction of the signal power above $1/T_{\rm obs}$ that is fit with $N_{\rm F}$ components is equal to $1-N_{\rm F}^{1-\gamma}$ when $\gamma > 1$. As an example, for a typical $\gamma = 3$, with 30 Fourier components we take into account 99.9% of the red noise power above $1/T_{\rm obs}$. Below $\gamma = 1.5$, where 30 Fourier components take into account 81.7% of the red noise power above $1/T_{\rm obs}$, it is better to use more Fourier components. In reality, after we calculate this fraction for the power up to the sampling frequency, this fraction will be greater. Nevertheless, for pulsar J2145−0750, where in Lentati et al. (2016) it has been estimated that $\gamma = 0.6 \pm 0.2$, we use 100 Fourier components (107 components were used in Lentati et al. (2016)). We model remaining pulsars with 30 Fourier components, which is

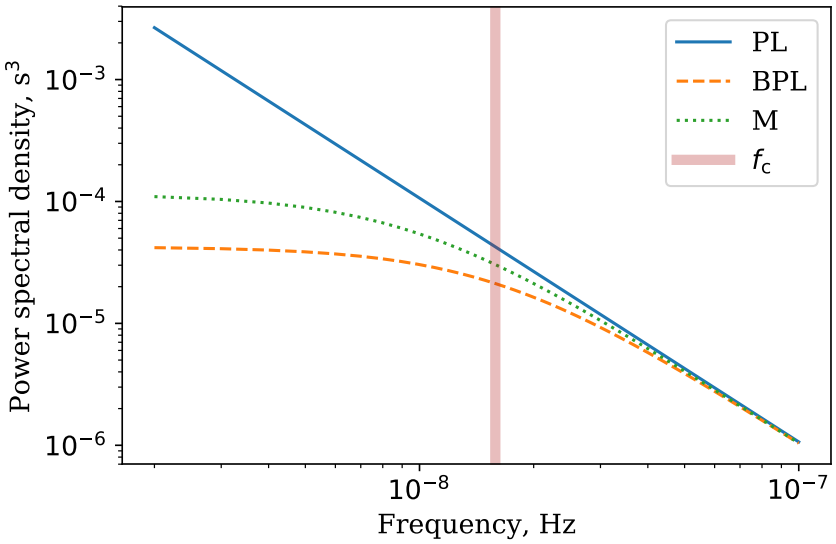

FIGURE 3.1. Models for pulsar red noise power spectral density. The blue solid line represents Model PL (Equation 3.13) and the orange dashed line represents Model BPL (Equation 3.14). For both of them we chose $A = 2 \times 10^{-13}$ and $\gamma = 2$. For the orange dashed line $f_c = 0.5$ yr^{-1}. The green dotted line represents Model 3.15 (Equation 3.15) with $\eta(R^{-1}) = 0.5$ yr^{-1}, $\lambda = 0.5$, assuming pulsar spin period of 1 ms.

a reasonable and computationally-cheap approximation. More comments on the consequences of this choice are provided in Section 3.5.

3.2.4 Software

We estimate the design matrix using the `designmatrix` plugin in `TEMPO2` (Hobbs et al., 2006). We simulate data and access `TEMPO2` using `libstempo` (Vallisneri, 2013). We construct our models and likelihood, and do parameter estimation using `Enterprise` (Ellis et al., 2019). We perform likelihood sampling using the `PTMCMCSampler` (Ellis and van Haasteren, 2017) for IPTA DR1 data. For simulations we use a nested sampler `Dynesty` (Speagle and Barbary, 2018), and we use `Bilby` (Ashton et al., 2019a) to access the Dynesty sampler.

3.3 Simulation study

We perform a simulation study to demonstrate our ability to do Bayesian model selection. We also demonstrate some potential subtleties in recovering a low-frequency turnover. We simulate ToAs, ToA errors, and timing residuals for the pulsar J0711−6830, using ephemerides from the ATNF Pulsar Catalogue (Manchester et al., 2005). We simulate ToAs evenly sampled once every 30 days

between MJD 53000 and 56650, which is roughly consistent with the average cadence of a typical IPTA observatory (see Verbiest et al., 2016, Table 1). We assume ToA errors to be 0.5 μs, which is within the range of ToA errors as found in the first data release of the IPTA. These parameters are applied to all simulations described in this section of the paper. In our noise simulations we only assume one observing system, one observed radio frequency, and only red and white noise. The red noise parameters chosen for simulations are described in the following subsections. We choose them, so that they are approximately consistent with noise parameters of the real data (see, e.g., Lentati et al., 2016, Table 6). The parameter values recovered from simulations in this section have been confirmed to be consistent with injected values.

3.3.1 Red noise in an ensemble of pulsars

We simulate 50 mock pulsars with different random realisations of Model PL red noise and white noise. Then we perform model selection between Model PL and Model BPL. The simulated white noise parameters throughout the subsection are EFAC = 1 and EQUAD = 0.1 μs. According to Section 3.3 of Verbiest et al. (2016), these are the typical EFAC and EQUAD values found in IPTA DR1. The simulated red noise amplitude is different for the three cases we describe in this subsection, while the priors for red noise power-law index and corner frequency are $\pi(\gamma) = \mathcal{U}(2,5)$ and $\pi(f_c) = \log_{10}\mathcal{U}(10^{-10}, 10^{-6})$. Here $\mathcal{U}$ stands for a uniform distribution, and $\log_{10}\mathcal{U}$ stands for a uniform in $\log_{10}$ distribution. We use the same red noise priors for A and γ for models PL and BPL, for both injection and recovery.

First, we simulate Model PL with a prior $\pi(A) = \log_{10}\mathcal{U}(10^{-14}, 10^{-11})$. The prior range for noise amplitude is chosen such that red noise is overall stronger than white noise. As a result, with all simulated pulsars, we obtain $\log \mathcal{B}^{\rm BPL}_{\rm PL} = -30.8$. Hence, Model PL is correctly preferred over Model BPL.

Second, we demonstrate that we do not prefer the wrong model if the red noise is overall much weaker than white noise. The prior for simulation and recovery of red noise amplitude is reduced to $\pi(A) = \log_{10}\mathcal{U}(10^{-17}, 10^{-14})$. Now, $\log \mathcal{B}^{\rm BPL}_{\rm PL} = 1.0$. Therefore, if the red noise is too weak, we cannot distinguish between two models, as expected.

Finally, we demonstrate that, when the data from multiple pulsars are injected with Model BPL, our algorithm prefers Model BPL over Model PL. To do this, we use the following prior on red noise amplitude $\pi(A) = \log_{10}\mathcal{U}(10^{-14}, 10^{-11})$. Now we obtain $\log \mathcal{B}^{\rm BPL}_{\rm PL} = 96$ favouring the correct model. Our results for this subsection are summarized in Table 3.1. All injected signals were successfully recovered.

3.3.2 Prior mismatch in simulations

Most of the IPTA pulsars from DR1 are dominated by white noise Lentati et al. (2016). In this subsection, we perform simulations that demonstrate that model selection for red noise in data, dominated by white noise, can lead to the false detection of a spectral turnover, if we do not

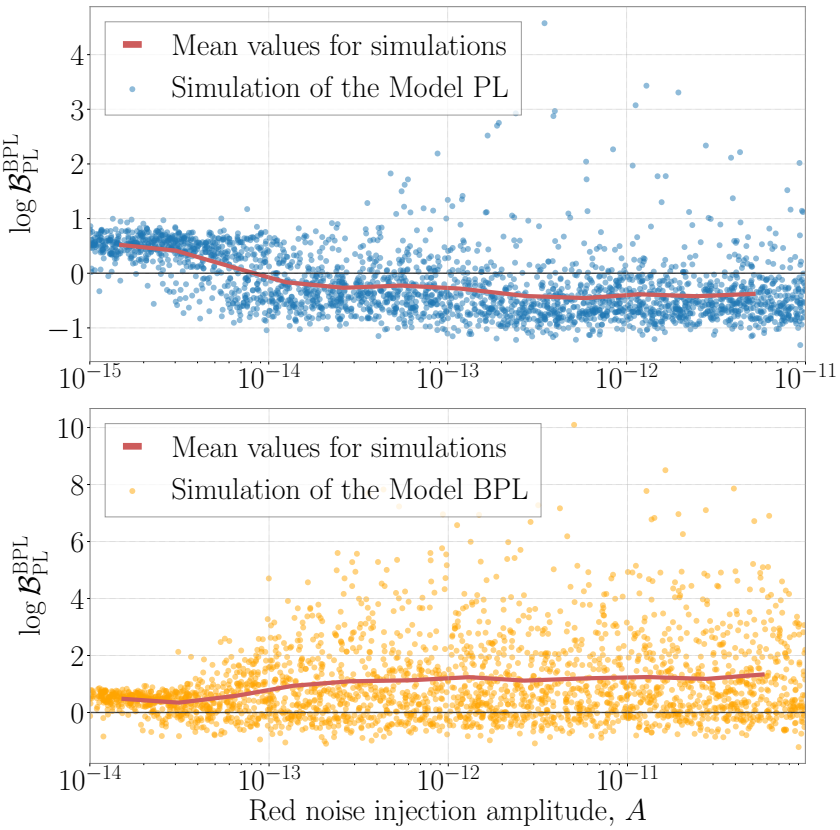

FIGURE 3.2. The demonstration of the effect of sample variance on the recovery of a spectral turnover. Each point represents $\log \mathscr{B}^{\mathrm{BPL}}_{\mathrm{PL},i}$. The top plot with blue points is for different realisations of a power law, Model PL (Equation 3.13), while the bottom plot with orange points is for different realisations of a broken power law, Model BPL (Equation 3.14). The injection parameters, except red noise injection amplitude A (horizontal axes), are the same for both plots. As the amplitude of the red noise is increased, the evidence in favour (bottom plot) and against (top plot) the spectral turnover plateaus. Red lines are mean values for every 200 simulations.

carefully choose our prior. We perform simulations of only white noise with EFAC = 1 and EQUAD = 0.1 μs. We perform model selection between models BPL and PL. We observe that evidence for the absence of red noise (Model $\varnothing$) is always the strongest, while either Model PL or BPL may be preferred, depending on our prior on f_{c} parameter. As we allow our prior on f_{c} to include only low values less than around $1/T_{\mathrm{obs}}$, we can not distinguish models PL and BPL. As we allow our prior on f_{c} to include only frequencies higher than our sampling frequency, we cannot distinguish between models BPL and $\varnothing$, and model selection between PL and BPL prefers BPL. This is not surprising, as white noise and Model PL are limiting cases of Model BPL. Therefore, for the case of the DR1 analysis, when the true distribution of spin noise parameters is unknown, we propose to account for this effect by including in Equation 3.8 only pulsars having $\log \mathscr{B}^{\mathrm{PL}}_{\varnothing,i} \geq 5$

Table 3.1: Priors for the injection study in Section 3.3.1. Here $\mathcal{U}$ stands for a uniform distribution, and $\log_{10}\mathcal{U}$ stands for a uniform in $\log_{10}$ distribution.

Injected model	$\pi(A)$	$\log\mathcal{B}^{\rm BPL}_{\rm PL}$	Preferred model
PL	$\log_{10}\mathcal{U}(10^{-14},10^{-12})$	−30.8	PL
PL	$\log_{10}\mathcal{U}(10^{-17},10^{-14})$	1.0	N/A
BPL	$\log_{10}\mathcal{U}(10^{-14},10^{-12})$	95.6	BPL

or $\log\mathcal{B}^{\rm BPL}_{\varnothing,i} \geq 5$. This way we exclude pulsars with no evidence of any spin noise and do not obtain false positives in favor of either a spectral turnover or its absence. Another solution to this problem is to fit the priors using the hierarchical inference (MacKay, 2003), which we defer to a future work.

3.3.3 The effect of sample variance in recovery of high amplitude red noise

In this subsection we find that with a PTA observation time of 10 years, we are unlikely to resolve a turnover in the red noise process of any particular pulsar, assuming a fiducial $f_{\rm c} = 10$ nHz. This is because factors a_i and b_i in Equation 3.9 become a source of noise themselves, and we do not have a data span long enough to effectively probe residuals spectra at frequencies around the turnover.

To demonstrate this, we simulate 1000 pulsars with red noise Model PL amplitude $\pi(A) = \log_{10}\mathcal{U}(10^{-15};10^{-11})$ and $\gamma = 3$, and simulate additional 1000 pulsars with red noise Model BPL with the same parameters and a corner frequency $f_{\rm c} = 10$ nHz. As the amplitude of the red noise in the set of simulated pulsars increases, the average $\log\mathcal{B}_i$ in favor of the correct model plateaus. This is demonstrated in Figure 3.2. We can see that, at some point, increasing $\log\mathcal{B}(f)$ starts slightly favouring the correct model, but then saturates, so that increasing the amplitude of the red noise does not help to resolve a low-frequency turnover. In this medium-to-strong red noise regime, some realisations of Model PL may favour the Model BPL hypothesis, and vice versa. However, the mean $\log\mathcal{B}^{\rm BPL}_{{\rm PL},i}$ (red line in Figure 3.2) favours the correct model.

3.4 Sources of noise in the first IPTA data release

In this Section, we describe sources of noise in the IPTA DR1 dataset. We use Lentati et al. (2016) as a guide for choosing what noise terms to include in our model. In Table 3.2, we list the prior distributions for parameters used in our models. Then we perform Bayesian inference of these parameters and model selection for millisecond pulsar spin noise.

Table 3.2: Priors used for model selection analyses between models PL (Equation 3.13) and BPL (Equation 3.14), and between models PL and M (Equation 3.15). Column 2 indicates whether the prior has been used in all model comparison analyses, or in model comparison between specific models.

Parameter $\boldsymbol{\theta}$	Model comparison	Prior $\pi(\boldsymbol{\theta})$
EFAC	all	$\mathcal{U}(0,10)$
EQUAD [s]	all	$\log_{10}\mathcal{U}(10^{-10},10^{-4})$
ECORR [s]	all	$\log_{10}\mathcal{U}(10^{-10},10^{-4})$
$A_{\rm SN}$	PL-BPL	$\log_{10}\mathcal{U}(10^{-20},10^{-8})$
	PL-M	$\log_{10}\mathcal{U}(10^{-17},10^{-10})$
$\gamma_{\rm SN}$	all	$\mathcal{U}(0,10)$
$f_{\rm c}$ [Hz]	PL-BPL	$\log_{10}\mathcal{U}(10^{-12},10^{-6})$
$M_{\rm SN}$	PL-M	$\log_{10}\mathcal{U}(10^{-1},10^{6})$
$t_{\rm c}$ [s]	PL-M	$\log_{10}\mathcal{U}(2\pi\times10^{8},10^{22})$
$A_{\rm DM}$	all	$\log_{10}\mathcal{U}(10^{-20},10^{-8})$
$\gamma_{\rm DM}$	all	$\mathcal{U}(0,10)$
$A_{\rm BS}$	all	$\log_{10}\mathcal{U}(10^{-16},10^{-10})$
$\gamma_{\rm BS}$	all	$\mathcal{U}(0,10)$
$A_{\rm E}$	all	$\log_{10}\mathcal{U}(10^{-10},10^{-2})$
$t_{\rm E}$ [MJD]	all	$\mathcal{U}(54500,54900)$
$\tau_{\rm E}$ [MJD]	all	$\log_{10}\mathcal{U}(5,100)$
$A_{\rm G}$	all	$\log_{10}\mathcal{U}(10^{-6},10^{-1})$
$t_{\rm G}$ [MJD]	all	$\mathcal{U}(53710,54070)$
σ_G [MJD]	all	$\mathcal{U}(20,140)$

3.4.1 White noise

IPTA pulsars are often monitored by several radio observatories. The raw voltages from each telescope are processed by different hardware. Each observing system has different measurement errors, contributing to measured white noise. Noise parameter EFAC, introduced in Equation 3.12, accounts for ToA uncertainty, associated with errors during the process of cross-correlation of pulse profile templates with observed pulse profiles. Parameter EQUAD is introduced to account for stochastic variations in both phase and amplitude of radio pulse profiles. These variations are called "pulse jitter" (Osłowski et al., 2011a; Shannon et al., 2014). Parameters EFAC and EQUAD are introduced for each backend system that processes raw telescope data, in accordance with Equation 3.12. In NANOGrav data, one epoch of observations with wide-band receivers is split into multiple ToAs, corresponding to different radio-frequencies, or sub-bands. Thus, for NANOGrav data, ECORR parameters are introduced to account for correlations between sub-banded ToAs at each epoch (Arzoumanian et al., 2018a).

3.4.2 DM noise

Dispersion measure (DM) is the electron column density, integrated along the line of sight to a pulsar. Stochastic variations in dispersion measure result in DM noise. We model DM noise as a power law with $A_{\rm DM}$ and $\gamma_{\rm DM}$, where $\kappa_j = K^2 \nu_j^{-2}$ in Equation 3.9. So, both κ_j and $F_{i,j}$ depend on the radio frequency ν_j (Hz) of the j'th ToA. A constant $K = 1400$ MHz can be thought of as a reference radio frequency. We account for DM variations for every pulsar in IPTA analysis.

3.4.3 Band noise and system noise

Lentati et al. (2016) found that specific IPTA pulsars show evidence of band noise and system noise, which introduces additional red noise in some observing systems and radio frequency bands. Lentati et al. (2016) suggested polarization calibration errors as a possible origin for system noise. Radio-frequency interference and the interstellar medium were proposed as possible origins of band noise. In order to separate band noise and system noise from spin noise, we add a separate power law with $A_{\rm BS}$ and $\gamma_{\rm BS}$ on specific radio frequency bands and systems for specific pulsars where band and system noise for IPTA data release 1 has been found (see Table 4 in Lentati et al., 2016, for details).

3.4.4 Spin noise

We model spin noise as a common red noise process between all observing systems and radio frequencies. Model PL depends on parameters $A_{\rm SN}$ and $\gamma_{\rm SN}$, Model BPL depends on an additional parameter $f_{\rm c}$. We refer to a hypothesis that no spin noise is present in the data, as to Model $\varnothing$. In this work, we are mostly interested in resolving a spectral turnover in spin noise, characterized by the parameter $f_{\rm c}$ in Model BPL. We are also interested in Model M with parameters $M_{\rm SN}$ and $t_{\rm c}$. As always, one must exercise caution when choosing suitable priors, as the Bayes factor depends on the choice of prior (Kass and Raftery, 1995). When carrying out model selection between Model M and Model PL, we chose our prior on Model PL amplitude A to match the range of spin noise amplitudes that is allowed by our priors for $\eta(R^{-1})$ and λ in Model M. Otherwise, the model with a wider prior range on spin noise amplitude would be incorrectly penalized when calculating a Bayes factor.

3.4.5 Transient noise events

Pulsars J1713+0747 and J1603−7202 show evidence of a sudden change in dispersion measure (Coles et al., 2015; Desvignes et al., 2016; Keith et al., 2013; Zhu et al., 2015). We take these events into account using the same empirical models that were used in Lentati et al. (2016). For J1713+0747 we model the event as a frequency-dependent sudden decrease followed by an exponential increase in timing residuals:

Table 3.3: Results for IPTA DR1 pulsars where we found $\log \mathscr{B}^{\rm BPL}_{\varnothing,i} > 0$ and $\log \mathscr{B}^{\rm PL}_{\varnothing,i} > 0$. Columns 3 ($A_{\rm SN}$) and 4 ($\gamma_{\rm SN}$) are the red noise parameter estimates for Model PL. Columns 5 ($\log \mathscr{B}^{\rm PL}_{\varnothing,i}$) and 6 ($\log \mathscr{B}^{\rm BPL}_{\varnothing,i}$) show whether pulsar data favours Models BPL (Equation 3.14) and PL (Equation 3.13) against no spin noise. Columns 7 ($\log \mathscr{B}^{\rm BPL}_{{\rm PL},i}$) and 8 ($\log \mathscr{B}^{\rm M}_{{\rm PL},i}$) show how specific pulsars favors Models BPL and M (Equation 3.15) over Model PL. The exact values of Bayes factors for some pulsars were hard to calculate using the product-space sampling method, so we only provided lower limits. Here we assume a Solar System ephemeris model DE421, which is a default option for IPTA DR1.

Pulsar	$T_{\rm obs}$ (yr)	$\log_{10} A_{\rm SN}$	$\gamma_{\rm SN}$	$\log \mathscr{B}^{\rm PL}_{\varnothing,i}$	$\log \mathscr{B}^{\rm BPL}_{\varnothing,i}$	$\log \mathscr{B}^{\rm BPL}_{{\rm PL},i}$	$\log \mathscr{B}^{\rm M}_{{\rm PL},i}$
J0613−0200	13.7	$-14.62^{+0.60}_{-1.20}$	$4.70^{+2.88}_{-0.92}$	10.7	10.2	−0.5	−2.0
J0621+1002	14.3	$-12.10^{+0.12}_{-0.13}$	$2.50^{+0.72}_{-0.43}$	4.6	6.5	1.9	1.5
J1713+0747	21.2	$-14.81^{+0.39}_{-0.83}$	$4.55^{+1.90}_{-0.69}$	>11.7	>11.6	−0.2	−4.8
J1824−2452A	5.8	$-12.80^{+0.56}_{-3.05}$	$2.30^{+4.44}_{-0.32}$	19.0	18.8	−0.2	1.3
J1939+2134	27.1	$-14.33^{+0.24}_{-0.40}$	$6.31^{+0.80}_{-0.54}$	>12.5	>11.4	−1.1	−109.8
J2145-0750	17.5	$-13.03^{+0.09}_{-0.06}$	$0.44^{+0.57}_{-0.14}$	>11.6	>12.5	0.8	−2.0
J1024−0719 *	15.9	$-13.94^{+0.22}_{-0.41}$	$5.41^{+1.00}_{-0.53}$	>12.4	>11.8	−0.6	−29.0

$$s_{\rm E}(t|A_{\rm E}, t_{\rm E}, \tau_{\rm E}) = K^2 \nu^{-2} \begin{cases} 0, & t < t_{\rm E}\ ; \\ A_{\rm E}\, e^{-\frac{t-t_{\rm E}}{\tau_{\rm E}}}, & t \geq t_{\rm E}\ ; \end{cases} \tag{3.16}$$

where ν is a radio frequency, and $K = 1400$ MHz is the same reference frequency as we use to model DM noise. We model the DM event in pulsar J1603−7202 as a Gaussian function in the time domain:

$$s_{\rm G}(t|A_{\rm G}, t_{\rm G}, \sigma_{\rm G}) = K^2 \nu^{-2} A_{\rm G}\, e^{-\frac{(t-t_{\rm G})^2}{2\sigma^2_{\rm G}}}. \tag{3.17}$$

DM event models in Equation 3.16 and Equation 3.17 are added to the signal vector $\boldsymbol{s}$ in the likelihood. Event $s_{\rm G}$ corresponds to an overdensity in the interstellar medium, whereas $s_{\rm E}$ corresponds to an underdense region in the interstellar medium.

3.5 Results

We perform parameter estimation and model selection for pulsars from the first IPTA data release. A summary of our analysis for individual pulsars is given in Table 3.3. The first column contains pulsar names and the second column contains observation spans. The next two columns, $\log_{10} A_{\rm SN}$ and $\gamma_{\rm SN}$, represent parameter estimates for Model PL with errors, based on 16% and 84% levels of marginalized posteriors. The last two columns contain the results of spin noise model selection. From the seventh column, we see that specific pulsars do not show support in favour of a spectral turnover because $|\log \mathscr{B}^{\rm BPL}_{{\rm PL},i}| < 2$ for all pulsars.

Next, we employ Equation 3.8, in order to use all available data for model selection. We perform our analysis with five different Solar System ephemeris models, as it has been found that errors in Solar System ephemerides contribute to pulsar red noise (Arzoumanian et al., 2018a; Caballero et al., 2018; Guo et al., 2019). We find that data favours neither Model PL, nor Model BPL. This result is summarized in Table 3.4.

Note, Tables 3.3 and 3.4 contain only results from seven pulsars where $\log \mathscr{B}^{\rm PL}_{\varnothing} > 5$ or $\log \mathscr{B}^{\rm BPL}_{\varnothing} > 5$. In Table 6 in Lentati et al. (2016), authors present eight pulsars that show evidence for spin noise in their analysis. Seven of them can be found in our Table 3.4: J0613−0200, J0621+1002, J1713+0747, J1824−2452A, J1939+2134, J2145−0750 and J1024−0719. In the remaining pulsar J1012+5307 we did find some evidence of spin noise, $\log \mathscr{B}^{\rm PL}_{\varnothing,i} = 4.3$, assuming the default Solar System ephemeris DE421. However, J1012+5307 did not satisfy our formal criteria to be included in Table 3.4. It is worth noting that in Lentati et al. (2016) pulsar J2145−0750 is found to have the most shallow power-law index $\gamma_{\rm SN} = 0.6 \pm 0.2$. For the reasons discussed in Section 3.2.3, J1012+5307 only showed evidence of spin noise in our analysis after we changed a number of Fourier components $N_{\rm F}$ from 30 to 100 for this pulsar. Pulsar J1024−0719 is marked with a star for the following reason. It has been suggested that the spin noise in J1024−0719 originates from a companion star in a long-period binary system (Kaplan et al., 2016). After we take binary motion into account, by adding a second spin frequency derivative into the timing model, we see no evidence for spin noise in J1024−0719.

The last column in Table 3.3, $\log \mathscr{B}^{\rm M}_{{\rm PL},i}$, presents log Bayes factors in favour of Model M over Model PL. We find that no pulsars show a strong support for Model M. However, pulsars J1939+2134, J1024−0719 and J1713+0747 disfavour Model M with $\log \mathscr{B}^{\rm M}_{{\rm PL},i} < -4$.

We also consider that our data may contain a mixture of pulsars from two models. For this case, we define a likelihood:

$$\mathscr{L}^{\rm A}_{\rm B}(\xi) = \prod_{i=1}^{\rm N_{psr}} \left(\xi \mathscr{Z}^{\rm A}_i + (1-\xi) \mathscr{Z}^{\rm B}_i \right), \tag{3.18}$$

where ξ is a hyper-parameter that determines the fraction of pulsars that are described by model A. The prior for ξ is $\mathscr{U}(0,1)$. The rest of the pulsars are described by model B. Using Equation 3.18, we estimate the fraction of pulsars that are consistent with a superfluid turbulence origin and a spectral turnover. The results are summarized in Figure 3.3. We estimate that the fraction of pulsars with the spectral turnover is consistent with any number between 0 and 1, while the fraction of pulsars where Model M is favored over Model PL is mostly consistent with zero. Since no spectral turnover is detected, pulsars J0621+1002 and J1824−2452A could get positive preference for Model M over Model PL because their power-law index γ is consistent with 2.

Table 3.4: The overall $\log \mathscr{B}^{\mathrm{BPL}}_{\mathrm{PL}}$ in favour of Model BPL (Equation 3.14) over Model PL (Equation 3.13), using all available IPTA data, for different Solar System ephemeris models.

Ephemeris	$\log \mathscr{B}^{\mathrm{BPL}}_{\mathrm{PL}}$	$\log \mathscr{B}^{\mathrm{BPL}}_{\mathrm{PL}}$ (without J1024−0719)
DE405	−0.4	0.3
DE418	−1.0	−0.3
DE421	0.2	0.8
DE430	−0.1	0.7
DE435	−0.8	−0.1

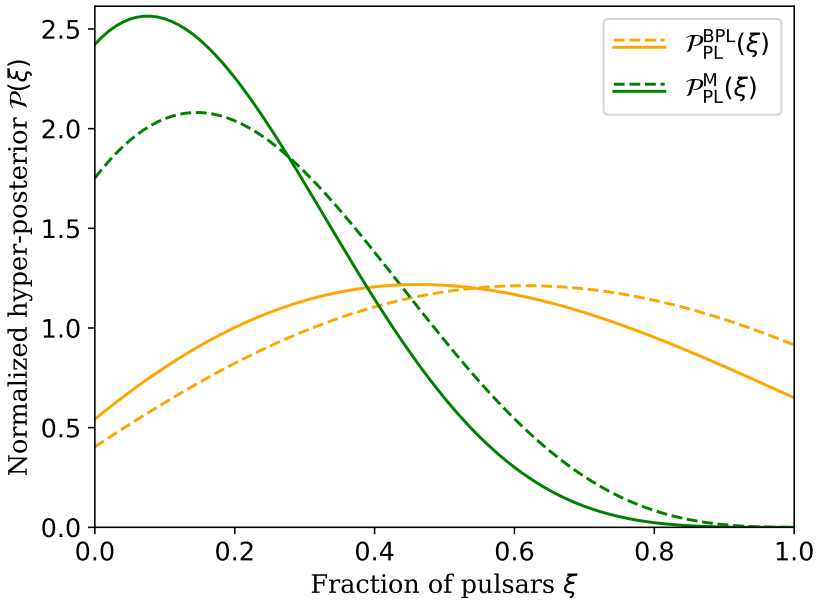

FIGURE 3.3. Hyper-posteriors $\mathscr{P}(\xi)$ for DR1 pulsars. Orange lines are posteriors $\mathscr{P}^{\mathrm{BPL}}_{\mathrm{PL}}(\xi)$ for the fraction of pulsars that are described by Model BPL (Equation 3.14), assuming other pulsars are described by Model PL (Equation 3.13). Green lines are posteriors $\mathscr{P}^{\mathrm{M}}_{\mathrm{PL}}(\xi)$ for a fraction of pulsars that are described by Model M (Equation 3.15), assuming other pulsars are described by Model PL. For solid lines, we assume that spin noise in J1024−0719 is intrinsic to the pulsar. For dashed lines, we assume that the apparent spin noise in J1024−0719 is caused by the second spin frequency derivative of the pulsar induced by gravitational interaction of J1024−0719 with a binary companion star (Kaplan et al., 2016).

3.6 Conclusions

We perform Bayesian model selection to search for a spectral turnover in pulsar spin noise using the first data release of the IPTA. We find support, with a log Bayes factor above 4, for spin noise in eight pulsars, which is consistent with Lentati et al. (2016). However, we find no evidence for a

spectral turnover either in individual pulsar data or by combining different pulsars. We also fit the data to the superfluid turbulence model proposed by Melatos and Link (2013). Our results show that whereas this model is indistinguishable from the power-law model for most pulsars, it is strongly disfavored by three pulsars, especially PSR J1939+2134 with a log Bayes factor of 110.

Based on a range of simulations, we find that one is unlikely to resolve a spectral turnover with a fiducial corner frequency of 10 nHz in any pulsar with ≈ 10 years of observations. Longer data spans are required to increase the detection confidence of a spectral turnover in individual pulsars, while a larger number of pulsars with red noise can help to resolve the presence of a spectral turnover in a population of pulsars. A follow-up study using longer data sets and a larger sample of pulsars, e.g., the IPTA second data release (**?**), will prove useful in not only understanding the nature of red noise in millisecond pulsars but also in evaluating the realistic prospect of gravitational-wave detection. A more detailed simulation study is required to explore pulsar timing array configurations that would resolve spectral turnover in the individual pulsars. Whereas our simulation study assumed a pulsar with observation span of 10 years, two pulsars from the first data release of the IPTA have observations spans above 25 years. At the same time, next-generation pulsar timing arrays based on MeerKat, FAST, SKA, will have a reduced radiometer noise. Both greater observation spans and reduced white noise levels will increase the sensitivity of a pulsar timing array to the spectral turnover, and the future study could help to estimate by how much. Simulations that attempt to provide a precise answer to these questions for the real data ought to include all other noise sources (i.e., DM noise, band noise), multiple observing backends with realistic observation cadences. Another interesting future simulation study would determine whether the broken power-law model would be favored over the power-law model when the superfluid turbulence model is simulated.

3.7 Acknowledgements

We thank the anonymous referee for valuable feedback. We thank Nataliya Porayko, Yuri Levin, Daniel Reardon and Paul Lasky for useful discussions. BG, XZ, and ET are supported by ARC CE170100004. ET is additionally supported by ARC FT150100281.

CHAPTER 4

IDENTIFYING AND MITIGATING NOISE SOURCES IN PRECISION PULSAR TIMING DATA SETS

Submitted manuscript:
Goncharov, B., Reardon, D. J., Shannon, R. M., Zhu, X. J., Thrane, E., Bailes, M., Bhat, N. D. R., Dai, S., Hobbs, G., Kerr, M., Manchester, R. N., Osłowski, S., Parthasarathy, A., Russell, C. J., Spiewak, R., Thyagarajan, N., Wang J. B. (2020). Monthly Notices of the Royal Astronomical Society.

Pulsar timing array projects measure the pulse arrival times of millisecond pulsars for the primary purpose of detecting nanohertz-frequency gravitational waves. The measurements include contributions from a number of astrophysical and instrumental processes, which can either be deterministic or stochastic. It is necessary to develop robust statistical and physical models for these noise processes because incorrect models diminish sensitivity and may cause a spurious gravitational wave detection. Here we characterise noise processes for the 26 pulsars in the second data release of the Parkes Pulsar Timing Array using Bayesian inference. In addition to well-studied noise sources found previously in pulsar timing array data sets such as achromatic timing noise and dispersion measure variations, we identify new noise sources including time-correlated chromatic noise that we attribute to variations in pulse scattering. We also identify "exponential dip" events in four pulsars, which we attribute to magnetospheric effects as evidenced by pulse profile shape changes observed for three of the pulsars. This includes an event in PSR J1713+0747, which had previously been attributed to interstellar propagation. We present noise models to be used in searches for gravitational waves. We outline a robust

methodology to evaluate the performance of noise models and identify unknown signals in the data. The detection of variations in pulse profiles highlights the need to develop efficient profile domain timing methods.

4.1 Introduction

Pulsar Timing Arrays (PTA) perform measurements of pulse arrival times from millisecond pulsars over the time scales on the order of years (Foster and Backer, 1990b). Benefiting from the long-term timing stability of millisecond pulsars, the arrays are the most sensitive detectors of nanohertz gravitational waves. Taylor et al. (2016) predicts that a stochastic gravitational wave background from supermassive black hole binaries will be detected and studied with pulsar timing arrays in the following decade. The background would manifest as a red noise process that is correlated between pulsars (Rajagopal and Romani, 1994). In addition to gravitational waves, pulsar timing arrays are sensitive to other correlated signals, including errors in terrestrial time standards (Hobbs et al., 2020a, 2012) and solar system ephemerides (Caballero et al., 2018; Champion et al., 2010; Vallisneri et al., 2020), and, potentially, ultralight dark matter (Porayko et al., 2018). Data from pulsar timing arrays are used to study a wide range of astrophysical topics including: neutron-star interiors (Lam et al., 2016; Shannon and Cordes, 2010) and magnetospheres (Shannon et al., 2016), the interstellar medium (Coles et al., 2015; Levin et al., 2016), and the solar wind (Madison et al., 2019; You et al., 2007).

There are a number of pulsar timing array projects underway, utilising the most sensitive metre- and centimetre-wavelength radio telescopes. The Parkes Pulsar Timing Array (Manchester et al., 2013) utilises the 64-m Parkes telescope in Australia to monitor 24 millisecond pulsars. The first data release of the Parkes Pulsar Timing Array (DR1) has been described in Manchester et al. (2013), while timing properties of DR1 pulsars have been described in Reardon et al. (2016). The first data release comprises observations between 1994 and 2011. The project has recently completed a second data release (DR2, Kerr et al., 2020), which extends beyond DR1 by 7 years. Other timing array projects include the European Pulsar Timing Array (EPTA, Kramer and Champion, 2013) and North-American Nanohertz Gravitational-wave observatory (NANOGrav, McLaughlin, 2013b). Together, PPTA, EPTA and NANOGrav form the International Pulsar Timing Array (IPTA, Hobbs et al., 2010a).

In order to effectively search for spatially correlated signals, it is necessary to provide complete models for the arrival time variations of the pulsars. This includes both deterministic processes encapsulated in the pulsar ephemerides, and stochastic processes. Otherwise, the estimate of the gravitational-wave signal or other correlated signal could absorb unaccounted features in pulsar noise. In Shannon et al. (2016), it was found that a dip in timing residuals in J1643−1224, when not modelled, affects upper limits on the stochastic gravitational-wave background with 4 years of data by an order of magnitude. The dip itself is associated with a sudden change of pulse

profile. Moreover, Hazboun et al. (2020) and Tiburzi et al. (2016) studied cases where incorrect noise models led to false positives in gravitational wave searches.

Deterministic processes include the non-linear change in the relative distance between the pulsar and the Earth and relativistic propagation effects in the solar system or binary (if the pulsar has a companion) (Edwards et al., 2006). Stochastic terms can be divided phenomenologically into two classes: temporally uncorrelated or correlated processes. The two classes are often referred to respectively as white noise and red noise, reflecting the shape of their Fourier spectra. On short time scales (at high fluctuation frequency), pulsar timing observations are dominated by white noise. The main sources of white noise are radiometer noise and pulse-to-pulse variations of profile shape, referred to as pulse jitter. Shannon et al. (2014) found that the brightest observations of the brightest PPTA pulsars are dominated by jitter noise. In Lam et al. (2016) jitter was studied in the context of pulse phase and amplitude, and it has also been found that jitter noise evolves with radio frequency.

On longer time scales (lower fluctuation frequencies), pulsar timing arrays are dominated by time-correlated red noise. Achromatic red noise, which is not dependent on radio frequency, is referred to as timing noise or spin noise because it is thought to largely be associated with irregularities in the rotation of the neutron star. Shannon and Cordes (2010) suggested that more millisecond pulsars are expected to be dominated by spin noise when observed over longer observing spans, and that scaling relations for spin noise in millisecond pulsars are consistent with those for regular pulsars. Later, Caballero et al. (2016) estimated power law parameters of the timing noise in the first data release of the EPTA and found that timing noise reduces the sensitivity of the EPTA to stochastic gravitational waves by a factor of > 9. Low-frequency turnover in the power-law timing noise could potentially stop the deterioration of timing precision on long time scales. Although marginal evidence for the low-frequency turnover has been found in a power-law spectrum of canonical pulsars (Parthasarathy et al., 2019), no presence of a spectral turnover has been found in 49 millisecond pulsars from the first data release of the IPTA (Goncharov et al., 2019).

There is also evidence for chromatic red noise processes in pulsars. The strongest red noise source is thought to be dispersion-measure variations (Keith et al., 2013), a manifestation of changing column density of ionised plasma along the pulsar-Earth line of sight. However, other forms of chromatic noise have been identified. In the first data release of the IPTA, Lentati et al. (2016) identified new band-dependent and system-dependent red noise processes. Ignoring these components resulted in 60% less stringent upper limits on the gravitational-wave background. The origins of these components are unclear, and were speculated to be either related to propagation effects in the interstellar medium or instrument-based systematic errors (Cordes and Shannon, 2010; Shannon and Cordes, 2017).

The PPTA DR2 data set comprises observations for as long as 15 years from 26 pulsars (Kerr et al., 2020). At each epoch (with epochs typically having a three-week cadence) the pulsars

were usually observed in three bands: the 10-cm, 20-cm, and either the 40-cm or 50-cm. The central radio frequencies of the observations in these bands were close to 3100 MHz, 1370 MHz, 730 MHz and 680 MHz, respectively. Before mid-2009, the low frequency observations were conducted at 680 MHz (50-cm band). However the presence of digital television necessitated adjusting the observations to shorter-wavelength 40-cm band. Additionally, each observation has been performed with one of the following observing processing systems (referred to as backends): `CASPSR`, `CPSR2`, `PDFB1`, `PDFB2`, `PDFB3`, `PDFB4`, and `WBCORR`. The most notable difference between DR1 and DR2 is the presence of sub-banded arrival times. Pulse arrival times are provided not only averaged across each band, but also for between 2 and 32 dynamically-chosen sub-bands, with the level of sub-banding determined by the signal to noise ratio of the observation. The sub-banding allows us to account for profile evolution, which is known to bias arrival time measurements (Demorest et al., 2012). It also allows us to examine chromatic processes in greater detail.

In this work, we characterise sources of noise in the second data release of the PPTA. We outline the Bayesian approach to analysis of the data in Section 4.2. In Section 4.3, we describe noise models in our analysis. We present our results in Section 4.4 and our conclusions in Section 4.5.

4.2 Bayesian inference

Our methods follow those described in sections 2.1 and 2.2 of Goncharov et al. (2019). We assume that the data is represented by contributions from deterministic signals, included in the timing model, and Gaussian stochastic processes. We Taylor-expand the timing model for each time of arrival (ToA), keeping the linear term $\boldsymbol{M\xi}$ and assuming non-linear terms to be negligible. Here, $\boldsymbol{\xi}$ is the vector of timing model parameters and $\boldsymbol{M}$ is the design matrix, which represents contribution of the timing model to each measured ToA. Following van Haasteren and Levin (2013); Van Haasteren et al. (2009), we employ the Gaussian likelihood function of the form,

$$\mathscr{L}(\boldsymbol{\delta t}|\boldsymbol{\theta}) = \frac{1}{\sqrt{(2\pi)^{n-m}\det(\boldsymbol{G}^T\boldsymbol{C}\boldsymbol{G})}} \exp\left(-\frac{1}{2}(\boldsymbol{\delta t}-\boldsymbol{s})^T\boldsymbol{G}(\boldsymbol{G}^T\boldsymbol{C}\boldsymbol{G})^{-1}\boldsymbol{G}^T(\boldsymbol{\delta t}-\boldsymbol{s})\right), \tag{4.1}$$

where $\boldsymbol{\delta t}$ is the vector of timing residuals, $\boldsymbol{C}$ is the covariance matrix to describe stochastic signals and $\boldsymbol{s}$ is the deterministic signal vector. We perform a singular value decomposition of the design matrix $\boldsymbol{M}$, so that $\boldsymbol{M} = \boldsymbol{USV}^*$, where $\boldsymbol{S}$ contains singular values of $\boldsymbol{M}$, $\boldsymbol{U}$ and $\boldsymbol{V}$ are unitary matrices with dimensions $n \times n$ and $m \times m$ respectively. Terms $\boldsymbol{U} = \boldsymbol{U_1G}$ with $\boldsymbol{U_1}$ and $\boldsymbol{G}$ consisting of the first m and remaining $n-m$ columns of $\boldsymbol{U}$.

We use the Bayes factor to select which of two given models (A and B), with parameters $\boldsymbol{\theta}_\mathrm{A}$

and $\boldsymbol{\theta}_{\rm B}$, better explains the data:

$$\mathscr{B}^{\rm B}_{{\rm A},i} = \frac{\mathcal{Z}^{\rm B}_i(\boldsymbol{\delta t})}{\mathcal{Z}^{\rm A}_i(\boldsymbol{\delta t})},\ i \in [1, N_{\rm psr}]\,, \tag{4.2}$$

where $N_{\rm psr}$ is the number of pulsars, and the function $\mathcal{Z}(\boldsymbol{\theta}, \boldsymbol{\delta t})$ is the Bayesian evidence for the model,

$$\mathcal{Z}(\boldsymbol{\delta t}) = \int \mathscr{L}(\boldsymbol{\delta t}|\boldsymbol{\theta})\pi(\boldsymbol{\theta})d\boldsymbol{\theta}. \tag{4.3}$$

It is an integral over the prior volume of the product of the likelihood and the prior probability.

We perform parameter estimation using Markov-chain Monte-Carlo methods. To calculate the Bayesian evidence for a given model, we perform nested sampling (Skilling et al., 2006) using `PolychordLite` (Handley et al., 2015a,b). For parameter estimation, we sample the likelihood function using `PTMCMCSampler` (Ellis and van Haasteren, 2017). We employ `TEMPO2` (Edwards et al., 2006) to fit the deterministic timing model parameters and use `Enterprise` (Ellis et al., 2019) and `Libstempo` (Vallisneri, 2013) to perform likelihood evaluations. The `Bilby` package (Ashton et al., 2019a) is used to access `PolychordLite`. The `ChainConsumer` package, developed by Hinton (2016), is used to plot posterior distributions.

4.3 Signal models

In the following subsections, we describe families of signal models we considered. The empirical prior distributions are listed in Table A.1.

4.3.1 White noise

We model white noise to be diagonal components σ_j of the covariance matrix $\boldsymbol{C}$, which contains known contributions from ToA uncertainties $\sigma_j^{\rm ToA}$ and unknown contributions that we take into account by introducing parameters EFAC and EQUAD. The parameter EFAC modifies the TOA uncertainty while EQUAD adds in quadrature an extra term that is independent of the formal TOA uncertainty. The modified white noise component to the timing noise is then

$$\sigma_j^2 = (\mathrm{EFAC}\ \sigma_j^{\rm ToA})^2 + \mathrm{EQUAD}^2\ . \tag{4.4}$$

As these values are expected to be signal-processor- and band-dependent, we assume different white noise terms for each band and all backends. The exception is for `PDFB2`, `PDFB3`, and `PDFB4`, which have similar hardware architectures (digital polyphase filter banks); for these we assume to have the same white noise properties within a band.

4.3.2 Red noise

We implement frequency-domain models of time-correlated stochastic proceses in the time-domain likelihood function, using a Fourier-sum approach, described in Lentati et al. (2013). The red noise component of the covariance matrix $\boldsymbol{C}$ is represented in a reduced order as

$$\boldsymbol{K} = \boldsymbol{F}\boldsymbol{\Phi}\boldsymbol{F}^{\mathrm{T}}\,\Delta f\ , \tag{4.5}$$

where $\Phi_i = P(f_i)$ is the power spectral density model of the red noise for each frequency f_i that we include in our model, $\boldsymbol{F}$ is the Fourier basis, the matrix that Fourier-transforms frequency-domain power spectral density model into the time domain covariance. The size of a frequency bin, Δf, is equal to the inverse of the total observation time for a given pulsar. The exact form of $\boldsymbol{F}$ that we use can be found in Equation 9 in Goncharov et al. (2019). A Woodbury lemma is then used to simplify the inversion of a covariance matrix, decomposed into $\boldsymbol{N}$ and $\boldsymbol{K}$ (Hager, 1989; van Haasteren and Vallisneri, 2014). We use the frequency-domain model for pulsar red noise with power spectral density following a power law in units of $[s^3]$:

$$P_{\mathrm{PL}}(f|A,\gamma) = \frac{A^2}{12\pi^2}\left(\frac{f}{\mathrm{yr}^{-1}}\right)^{-\gamma}\mathrm{yr}^3, \tag{4.6}$$

where A quantifies the amplitude[1] of the power-law, γ is the slope of the power-law and yr is the number of seconds in a year. We discuss three subsets of red noise in this work:

- Achromatic spin noise (SN)
- Frequency-dependent dispersion measure (DM) noise
- Achromatic band noise (BN) and system ("group") noise (GN)
- Frequency-dependent chromatic noise (CN)

For each pulsar, the spin noise is a common red-noise process in all observing systems and bands, across all radio-frequencies. There are several potential origins for spin noise. Some studies suggest spin noise to be the consequence of the interaction between the crust and the superfluid core of a neutron star (Alpar et al., 1986; Jones, 1990). A model that links power-law parameters of a spin noise to physical parameters of such systems has been derived in Melatos and Link (2013). Other studies attempt to link spin noise and pulsar glitches, sudden jumps in rotational frequency of pulsars (Cordes and Downs, 1985; D'Alessandro et al., 1995; Johnston and Galloway, 1999a; Melatos et al., 2008). In Lyne et al. (2010), the authors suggested switching between two different spin-down rates as the origin of spin noise. Some models suggest that the influence of planets (Cordes, 1993), asteroids (Shannon et al., 2013) and possibly unmodeled binary motion (Bassa et al., 2016; Kaplan et al., 2016). We denote spin noise parameters A_{SN}

[1]The scaling for A is chosen such that it represents the amplitude of the strain spectrum of a stochastic gravitational wave background, measured a frequency of $1\,\mathrm{yr}^{-1}$.

and $\gamma_{\rm SN}$. We do not attempt to model uncertainties in the solar system ephemeris, which are known to contribute red noise to pulsar timing data sets. It is likely to affect red noise in the most stable pulsars. In particular, some of the red noise in PSR J1909−3744 can be attributed to this, as discussed below.

Stochastic variations in DM (Phillips and Wolszczan, 1991) are another source of red noise. We model DM noise as a power-law with parameters $A_{\rm DM}$ and $\gamma_{\rm DM}$, with Fourier basis components $\boldsymbol{F} \propto \kappa_j$, where $\kappa_j = K^2 \nu_j^{-2}$ is introduced to model the dependency of DM noise amplitude on the radio frequency ν_j of ToA j. We choose K = 1400 MHz to be the reference frequency. A Kolmogorov spectrum for turbulence in a neutral gas is used as a standard model to describe DM variations, DM(t), in the interstellar medium. In the case of Kolmogorov turbulence, we would expect $\gamma_{\rm DM}$ = 8/3 (Rickett, 1990).

We also search for a more general form of red noise which we refer to as chromatic red noise. In this case, we have $\kappa_j = K^\chi \nu_j^{-\chi}$, where χ is a value other than 2. We may refer to χ as the chromaticity of a red process. Numerous astrophysical mechanisms can potentially introduce chromatic red noise. Scattering variations in the interstellar medium change widths of radio pulses by $\Delta\nu \propto \nu^4$ (Lyne and Graham-Smith, 2012). While a template for pulse profiles does not account for this, the arrival times would temporal variations that would scale with radio frequency proportional to ν^{-4}. Shannon and Cordes (2017) show through simulation how refractive propagation effects can potentially introduce correlations in arrival times which can have frequency dependencies as steep as $\nu^{-6.4}$. Simulations of scattering of pulsar radio emission by the interstellar plasma have also been performed by Coles et al. (2010).

Band noise and system noise are separate red noise processes in a given band or system. Both were introduced and discussed in modelling of the first IPTA data release (Lentati et al., 2016). System noise is attributed to instrumental artifacts, including polarisation calibration errors. Band noise could potentially be produced by processes incoherent between bands in the interstellar medium, such as frequency dependent dispersion measure variations (Cordes et al., 2016), frequency-dependent calibration errors (Van Straten, 2013), or radio frequency interference.

4.3.3 Deterministic signals

To fully model the data we identified new deterministic signals in the timing model. We describe these in the following subsections.

4.3.3.1 Chromatic exponential dips

Some pulsars show evidence of frequency-dependent events in timing residuals on time scales of a few months. Some events have been identified as a sudden advancement in apparent pulse arrival time, followed by an exponential relaxation. PSR J1713+0747 shows an exponential discontinuity in timing residuals at around MJD 54757, which has been attributed to the sudden

drop in dispersion measure (Coles et al., 2015; Desvignes et al., 2016; Lentati et al., 2016). In Lam et al. (2018), a second exponential event in PSR J1713+0747 was reported and also attributed to the interstellar medium. In Shannon et al. (2016), an exponential timing event in J1643−1224 was reported, which had the most pronounced effect at high radio frequency. This event was connected with a sudden change in the pulse profile.

We model exponential events in the time domain to be

$$s_{\rm E}(t|A_{\rm E},t_{\rm E},\tau_{\rm E},\chi_{\rm E}) = K^{\chi}\nu^{-\chi}\begin{cases}0, & t<t_{\rm E}\ ;\\ A_{\rm E}\, e^{-\frac{t-t_{\rm E}}{\tau_{\rm E}}}, & t\geq t_{\rm E}\ ;\end{cases} \tag{4.7}$$

where $A_{\rm E}$ is the amplitude of the event in seconds, $t_{\rm E}$ is the time of the event, $\tau_{\rm E}$ is the characteristic relaxation time. The radio-frequency dependence, as for the case of chromatic noise, is treated by the parameter χ, and the amplitude of the event is at a frequency of 1400 MHz.

4.3.3.2 Extreme scattering events

Extreme scattering events (ESEs) have been observed in the direction of a number of pulsars. The events are manifested as increase in the electron density along the line of sight and diffractive scattering strength. This suggests that the line of sight to the pulsar passed through an overdense region of the interstellar medium (Coles et al., 2015; Keith et al., 2013). In our sample PSR J1603−7202 has been observed to have experienced an ESE (Coles et al., 2015). We model the dispersion measure variations associated with the event using a Gaussian function:

$$s_{\rm G}(t|A_{\rm G},t_{\rm G},\sigma_{\rm G}) = K^2\nu^{-2}A_{\rm G}\, e^{-\frac{(t-t_{\rm G})^2}{2\sigma_{\rm G}^2}}, \tag{4.8}$$

where $A_{\rm G}$ is the amplitude of the Gaussian in seconds at K = 1400 MHz, $t_{\rm G}$ is the time of the event, $\sigma_{\rm G}$ is the width. There are no measurable arrival time variations from diffractive scintillation during this event.

4.3.3.3 Annual dispersion measure variations

In case there is a strong gradient in electron column density between the pulsar and the Earth, the motion of the Earth around the sun will cause the gradient to manifest as annual DM variations. In Keith et al. (2013) a clear annual modulation in DM was identified for J0613−0200. We model this effect by including the deterministic yearly sinusoids:

$$s_{\rm Y}(t|A_{\rm Y},\phi_{\rm Y}) = A_{\rm Y}K^2\nu^{-2}\sin(2\pi t\times{\rm yr}+\phi_{\rm Y}), \tag{4.9}$$

with amplitude $A_{\rm Y}$ in seconds at K = 1400 MHz and dimensionless phase $\phi_{\rm Y}$. The strength of annual DM variations will depend on the two main factors. The first is the persistence of the annual gradient over time scales much longer than a year. The second is the mutual orientation of the gradient and the velocity of a pulsar. The orthogonal orientation of the velocity of the

pulsar with respect to the gradient provide the strongest annual DM signal, while the parallel orientation will diminish the signal. Additionally, contributions to DM from the heliosphere could potentially show up in annual DM.

4.3.3.4 System dependent profile evolution

In PPTA-DR2, arrival times were measured using standard techniques. While different standards were used for each band and most subsystems (see Kerr et al., 2020, for more information), the templates themselves were one-dimensional. This necessitated the use of FD parameters described above. For one pulsar, J0437−4715, we noticed that the profile evolution depended on system. The exceptional brightness of PSR J0437−4715 biases estimates of the pulse arrival times, due to profile templates not being tailored enough for each radio frequency. To account for pulse profile evolution, six `FD` parameters (Arzoumanian et al., 2015b) are introduced to the timing model of PSR J0437−4715, where each parameter represents a log-polynomial term of radio-frequency-dependence of timing residuals for the whole data span. Up to two FD parameters are included in timing models of the remaining DR2 pulsars. Additionally, in DR2, the dependence of timing residuals on radio-frequency for PSR J0437-4715 has been subtracted using the model with three `FD` parameters for specific systems and sub-systems: `CPSR2_50CM`, `CPSR2_20CM` above 1370 MHz, `CPSR2_20CM` below 1370 MHz, `PDFB1_1433`, `PDFB1_10CM`, `PDFB1_early_10CM`, `CPSR2_10CM` between 2970 MHz and 3030 MHz, `CPSR2_10CM` between 3100 MHz and 3160 MHz, `CPSR2_10CM` between 3230 MHz and 3290 MHz, `20CM_H-OH_PDFB1`, `20CM_MULTI_PDFB1`, `WBCORR_10CM` with 512 MHz bandwidth, `WBCORR_10CM` with 1024 MHz bandwidth.

We model this evolution using a linear function:

$$s_{\mathrm{F}}(\nu|\alpha) = \alpha(\nu - \tilde{\nu}), \tag{4.10}$$

where α determines the tilt in timing residuals in the radio frequency domain, while $\tilde{\nu}$ is the median radio frequency in the given system. More details and examples are provided in Section 4.4.

4.4 Results

We perform our analysis in three steps. For each pulsar, we first establish a base model, which contains white noise, spin noise (common red noise process in all observing bands and systems) and DM noise, and perform parameter estimation for the noise processes while marginalising over the timing model. In the second step, we start with the base model but perform model selection for the possible additional band/system noise components described in Section 4.3. Model selection for red noise in all possible bands and systems is computationally expensive, so we fixed white noise parameters at maximum-posterior values that we obtained in the first step. In the third step, after finding the most probable band/system noise combination, we perform

Table 4.1: Preferred models for the PPTA DR2 pulsars. For PSR J1024−0719, we present two models. The "+" symbol is used identify a model where second spin frequency derivative is included into the timing model to account for the influence of a possible companion star (Bassa et al., 2016; Kaplan et al., 2016). Parameters with asterisks are estimated from the median marginalized posterior values, while other parameter estimates are calculated from the maximum-posterior values. Symbol "↔" means that that the spin noise can not be distinguished from band-dependent red noise; see Section 4.4.1 for more details.

Pulsar	$\log\mathscr{B}^{\mathrm{DM,SN}}_{\varnothing}$	$\log\mathscr{B}^{\mathrm{DM}}_{\varnothing}$	$\log\mathscr{B}^{\mathrm{SN}}_{\varnothing}$	SN	$\log_{10} A_{\mathrm{SN}}$	γ_{SN}	DM	$\log_{10} A_{\mathrm{DM}}$	γ_{DM}	T_{obs} [yr]	n_{c}
J0437−4715	-	-	-	✓	$-14.01^{+0.05}_{-0.05}$	$1.78^{+0.18}_{-0.16}$	✓	$-13.52^{+0.05}_{-0.04}$	$2.76^{+0.16}_{-0.19}$	15.0	91
J0613−0200	57.3	52.5	57.6	✓	$-14.25^{+0.27}_{-2.08}$	$3.99^{+3.92}_{-0.39}$	✗			14.2	85
J0711−6830	75.6	64.6	68.3	✓	$-13.04^{+0.07}_{-0.07}$	$1.04^{+0.39}_{-0.22}$	✓	$-15.85^{*\,+1.76}_{-1.45}$	$6.31^{*\,+2.59}_{-3.16}$	14.2	86
J1017−7156	-0.7	-0.4	-0.2	✗			✗			7.8	46
J1022+1001	52.1	49.1	46.0	✓	$-16.51^{+2.10}_{-0.53}$	$7.02^{*\,+2.11}_{-2.73}$	✓	$-13.40^{*\,+0.08}_{-0.09}$	$0.40^{+0.59}_{-0.21}$	14.2	85
J1024−0719	474.0	259.1	435.1	✓	$-14.62^{+0.43}_{-0.95}$	$6.39^{+2.16}_{-0.71}$	✓	$-13.98^{+0.17}_{-1.50}$	$4.04^{+2.99}_{-0.51}$	14.1	85
J1024−0719^{+}	45.9	46.1	1.9	✗			✓	$-13.94^{+0.07}_{-1.94}$	$3.85^{+3.73}_{-0.29}$		
J1045−4509	-1.0	-0.1	-1.2	✗			✗			14.2	85
J1125−6014	170.9	171.3	124.2	✗			✓	$-13.02^{+0.08}_{-0.14}$	$2.83^{+0.52}_{-0.32}$	12.3	74
J1446−4701	3.1	2.8	2.5	↔	$-13.06^{+0.14}_{-5.17}$	$0.80^{+5.79}_{-0.24}$	✓	$-13.25^{+0.16}_{-4.33}$	$1.00^{+3.88}_{-0.23}$	7.4	44
J1545−4550	31.3	31.6	20.6	✗			✓	$-13.29^{+0.14}_{-0.45}$	$3.03^{+2.10}_{-0.34}$	7.0	41
J1600−3053	58.5	52.5	32.3	↔	$-13.90^{+0.13}_{-1.27}$	$3.60^{+2.38}_{-0.78}$	✓	$-13.56^{+0.04}_{-2.81}$	$3.48^{+5.28}_{-0.25}$	14.2	86
J1603−7202	457.7	458.0	341.7	✗			✓	$-13.19^{+0.09}_{-0.10}$	$2.30^{+0.47}_{-0.19}$	14.2	86
J1643−1224	275.4	260.6	235.2	✓	$-12.86^{+0.08}_{-0.05}$	$1.01^{+0.28}_{-0.24}$	✓	$-13.24^{+0.17}_{-0.32}$	$2.97^{+1.28}_{-0.27}$	14.2	85
J1713+0747	34.8	34.8	6.3	✗			✓	$-13.70^{+0.06}_{-0.05}$	$1.45^{+0.26}_{-0.19}$	14.2	86
J1730−2304	73.7	74.2	34.2	✗			✓	$-13.53^{+0.13}_{-0.78}$	$2.38^{+2.28}_{-0.09}$	14.2	86
J1732−5049	2.8	3.2	1.4	✗			✓	$-12.66^{+0.08}_{-1.90}$	$2.69^{*\,+4.71}_{-2.02}$	7.2	43
J1744−1134	161.4	161.8	118.0	✗			✓	$-13.58^{+0.06}_{-0.05}$	$1.51^{+0.30}_{-0.13}$	14.2	86
J1824−2452A	4328.9	3859.5	4204.2	✓	$-13.26^{+0.17}_{-0.47}$	$4.97^{+1.31}_{-0.34}$	✓	$-12.50^{+0.06}_{-0.04}$	$2.75^{+0.27}_{-0.29}$	13.8	83
J1832−0836	36.7	36.7	29.8	✗			✓	$-12.93^{+0.06}_{-1.41}$	$2.74^{+4.54}_{-0.01}$	5.4	32
J1857+0943	65.7	48.0	42.6	✓	$-15.99^{*\,+1.30}_{-0.97}$	$7.51^{*\,+1.72}_{-2.36}$	✓	$-13.40^{+0.14}_{-0.22}$	$2.56^{+0.76}_{-0.45}$	14.2	86
J1909−3744	121.4	113.4	9.2	✓	$-15.32^{+0.62}_{-1.08}$	$5.20^{+2.33}_{-1.45}$	✓	$-13.72^{+0.05}_{-0.03}$	$1.37^{+0.21}_{-0.14}$	14.2	85
J1939+2134	3834.5	3263.1	2507.9	✓	$-14.26^{+0.34}_{-0.25}$	$5.16^{+1.07}_{-0.61}$	✓	$-12.93^{+0.04}_{-0.02}$	$2.52^{+0.11}_{-0.14}$	14.1	85
J2124−3358	4.1	4.3	2.5	✗			✓	$-13.49^{+0.11}_{-0.32}$	$1.41^{+1.23}_{-0.18}$	14.2	85
J2129−5721	43.2	43.7	35.5	✗			✓	$-13.45^{+0.07}_{-0.11}$	$1.68^{+0.51}_{-0.33}$	13.9	83
J2145−0750	98.3	82.0	91.0	↔	$-13.18^{+0.09}_{-0.05}$	$0.50^{+0.31}_{-0.25}$	✓	$-13.63^{+0.15}_{-0.19}$	$1.00^{+0.94}_{-0.31}$	14.1	85
J2241−5236	104.7	103.4	88.4	✗			✓	$-13.82^{+0.06}_{-0.06}$	$1.05^{+0.32}_{-0.24}$	8.2	49

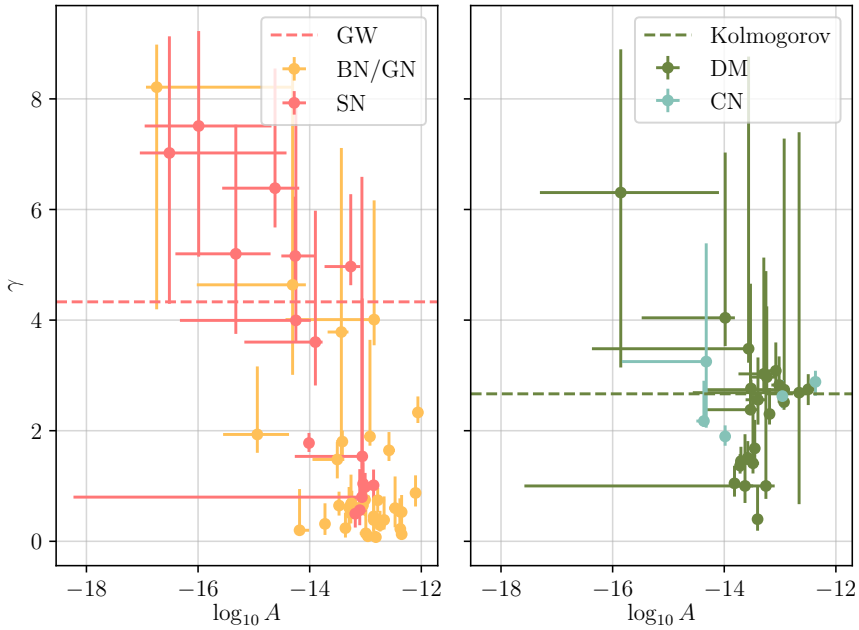

FIGURE 4.1. Strength and spectral index for red noise processes in the 26 PPTA DR2 pulsars. Left panel: spin noise (SN), band noise (BN) and system noise (GN). Right panel: DM noise and chromatic noise (CN) with strength referenced to $K = 1400$ MHz. The main feature of the left panel is the clustering of red noise parameters around two areas of the parameter space: where γ is between 2 and 10 (mostly spin noise), and where γ is between 0 and 2 (mostly band noise and system noise). For some pulsars, we found only marginal preference to choose between competing noise models with band and system noise, see Section 4.4.1 for more details. This is the reason for steep band/system noise and shallow spin noise in the figure. The red dashed line (GW) highlights the spectral index $\gamma = 13/3$, predicted for a red noise process induced by the stochastic gravitational-wave background. The green dashed line highlights $\gamma = 8/3$, predicted for the standard model of DM variations from Kolmogorov turbulence.

model selection for spin noise and DM noise in all pulsars, with free white noise parameters. Including white noise in parameter estimation increases the computation time by the order of magnitude. Similarly, if frequency-dependent index χ for chromatic red noise is a free parameter, the calculation takes by one order of magnitude more time than when χ is fixed. In the third step we fix χ at the maximum-posterior values.

We chose to incorporate additional terms if the more complicated model resulted in an increase in the $\ln \mathscr{B}$ of 3. Then, we perform model selection for spin noise and DM noise. All posteriors for red noise power-law parameters are presented in Figure 4.1. The DM and spin noise processes are described Table 4.1. Band-dependent and system-dependent red noise processes are described in Table 4.2. Chromatic noise processes are described in Table 4.3. We clarify that, although the

noise models presented in the above tables are valid for use in gravitational-wave searches, some of the red processes are only attributed to a certain class (i.e., spin noise or system noise) due to a marginal preference over competing hypotheses. We provide more details and explain the caveats below.

Additionally, we provide maximum-likelihood realisations of red noise processes in pulsars. We obtain them in two steps. Firstly, we perform red noise power-law parameter estimation, marginalizing over Fourier coefficients that determine the time evolution of red noise (van Haasteren and Vallisneri, 2014). Secondly, with `TEMPO2`, we estimate maximum-likelihood values of Fourier coefficients and hence the time evolution of red noise. We provide maximum-likelihood noise realisations for pulsars with chromatic noise in figures 4.2, 4.3, 4.4. The maximum-likelihood noise realisations for the remaining pulsars are shown in Figure A.2 in the Appendix.

4.4.1 Spin noise

We identify an increased sample of millisecond pulsars showing evidence for red noise. Longer datasets are more sensitive to low-frequency red noise. For example, for PSR J1909−3744 we find evidence for steep spin noise with $\gamma_{\rm SN} \approx 5$ in PPTA DR2, while in Shannon et al. (2015), with an 11 year dataset, there was no evidence for red noise. In DR2, we find evidence for spin noise in 11 pulsars, while Lentati et al. (2016) found spin noise only in 6 PPTA DR1 pulsars. In two of these six pulsars, J0613−0200 and PSR J1939+2134, we measure spin noise parameters consistent with Lentati et al. (2016). For PSR J1024−0719, when we do not model $\ddot{\nu}$, our measurement of $A_{\rm SN}$ is consistent with Lentati et al. (2016), while for $\gamma_{\rm SN}$ only 1-σ uncertainties overlap, so that the values are approximately within 2-σ agreement. For PSR J2145−0750, our measurement of $\gamma_{\rm SN}$ is consistent with Lentati et al. (2016), while values of $A_{\rm SN}$ are approximately within 2-σ agreement. For PSR J1824−2452A, we find evidence for steep spin noise, as in Lentati et al. (2016), although our measurements of spin noise parameters are not consistent. Lentati et al. (2016) finds stronger and more shallow spin noise. However, additional shallow band noise we identify in PSR J1824−2452A could be the reason for discrepancy. Similarly, for PSR J0613−0200 and PSR J1024−0719, where we find no evidence of band noise, spin noise parameters that we measure are consistent with red timing noise parameters in Caballero et al. (2016) within 1-2 σ credible levels. Since Caballero et al. (2016) do not model band noise and system noise, in other pulsars they identify examples of shallow red noise. Additionally, the sixth pulsar with spin noise in Lentati et al. (2016) is PSR J1713+0747, which is discussed below.

In 4 pulsars, marked with "↔" in Table 4.1, high radio frequency band noise is only marginally preferred ($\ln \mathscr{B}$ of less than 3) over achromatic noise alone. Three of these pulsars show evidence for a very shallow spin noise (low γ), which is more consistent for what we find for band and system noise (Table 4.2). For the fourth pulsar, PSR J1600−3053, the power-law index of $3.60^{+2.38}_{-0.78}$ is relatively steep, although still not uncommon for observed band and system noise.

Similarly, some pulsars with band and system noise have only marginal evidence in favour

Table 4.2: Results for band noise and system noise parameter estimation and model selection. The second column contains flags and the corresponding flag values to select pulse times of arrival, which are affected by the red noise. The third and the fourth columns contain red noise power-law parameters. The fifth column is the ln Bayes factor in favour of the band/system noise in addition to white noise, spin noise and DM noise, against the same model without the band/system noise term. The last column represents the number of Fourier components, explained in Section 4.3.2.

Pulsar	Flag and value	$\log_{10} A$	γ	$\log\mathscr{B}$	n_c
J0437−4715	`-group CPSR2_10CM`	$-13.41^{+0.06}_{-0.11}$	$0.68^{+0.53}_{-0.22}$	156.9	36
	`-group CPSR2_20CM`	$-13.01^{+0.07}_{-0.06}$	$0.75^{+0.25}_{-0.29}$	284.9	39
	`-group WBCORR_10CM`	$-13.26^{+0.13}_{-0.08}$	$0.31^{+0.37}_{-0.20}$	85.9	10
	`-group CPSR2_50CM`	$-12.92^{+0.07}_{-0.10}$	$1.48^{+0.31}_{-0.34}$	323.6	36
	`-B 40CM` and `-B 50CM`	$-13.51^{+0.13}_{-0.44}$	$1.90^{+1.75}_{-0.17}$	356.8	90
	`-B 20CM`	$-13.73^{+0.07}_{-0.06}$	$1.80^{+0.20}_{-0.27}$	353.8	90
J1017−7156	`-B 20CM`	$-13.26^{+0.08}_{-0.06}$	$0.50^{+0.35}_{-0.18}$	13.3	46
J1022+1001	`-group CPSR2_50CM`	$-12.38^{+0.07}_{-0.07}$	$0.22^{*\,+0.25}_{-0.16}$	9.6	31
	`-B 20CM`	$-12.81^{+0.04}_{-0.04}$	$0.08^{*\,+0.11}_{-0.06}$	45.2	85
	`-group PDFB_10CM`	$-12.35^{+0.05}_{-0.04}$	$0.13^{*\,+0.14}_{-0.09}$	109.3	64
J1125−6014	`-B 20CM`	$-12.85^{+0.07}_{-0.09}$	$0.45^{+0.38}_{-0.27}$	18.4	74
	`-B 10CM`	$-12.99^{+0.12}_{-0.11}$	$0.14^{+0.75}_{-0.00}$	7.3	21
J1600−3053	`-B 20CM`	$-13.29^{+0.08}_{-0.10}$	$0.61^{+0.37}_{-0.33}$	26.8	85
	`-B 40CM` and `-B 50CM`	$-12.58^{+0.11}_{-0.03}$	$1.65^{+0.33}_{-0.19}$	27.9	86
J1603−7202	`-group CPSR2_50CM`	$-12.47^{+0.15}_{-0.11}$	$0.60^{+0.57}_{-0.35}$	5.7	31
	`-B 20CM`	$-12.96^{+0.06}_{-0.04}$	$0.09^{*\,+0.13}_{-0.07}$	14.3	85
J1643−1224	`-B 40CM` and `-B 50CM`	$-12.06^{+0.04}_{-0.04}$	$2.33^{+0.29}_{-0.19}$	105.4	85
J1713+0747	`-group CPSR2_50CM`	$-12.85^{+0.02}_{-1.59}$	$3.78^{*\,+3.33}_{-2.32}$	8.1	31
	`-B 10CM` and `-B 20CM`	$-14.94^{+0.57}_{-0.61}$	$4.01^{+2.16}_{-0.46}$	4.4	86
	`-group CPSR2_20CM`	$-13.43^{+0.13}_{-0.25}$	$1.93^{+1.23}_{-0.33}$	21.9	36
J1744−1134	`-group CPSR2_50CM`	$-12.78^{+0.13}_{-0.06}$	$0.24^{*\,+0.28}_{-0.17}$	19.9	31
	`-B 10CM` and `-B 20CM`	$-13.36^{+0.07}_{-0.04}$	$0.74^{+0.22}_{-0.22}$	12.7	86
J1824−2452A	`-group PDFB_20CM`	$-12.67^{+0.09}_{-0.08}$	$0.39^{+0.43}_{-0.17}$	79.1	64
	`-B 40CM` and `-B 50CM`	$-12.10^{+0.09}_{-0.06}$	$0.87^{+0.32}_{-0.24}$	78.2	83
J1909−3744	`-B 10CM` and `-B 20CM`	$-14.18^{+0.17}_{-0.04}$	$0.20^{+0.75}_{-0.03}$	23.5	85
	`-B 40CM` and `-B 50CM`	$-13.25^{+0.07}_{-0.05}$	$0.68^{+0.23}_{-0.24}$	62.3	85
	`-group CPSR2_20CM`	$-14.31^{+0.24}_{-1.72}$	$4.64^{+3.83}_{-1.63}$	8.5	36
J1939+2134	`-B 40CM` and `-B 50CM`	$-12.74^{+0.06}_{-0.04}$	$0.29^{+0.26}_{-0.12}$	135.1	84
J2124−3358	`-B 20CM`	$-16.74^{+2.45}_{-0.19}$	$8.21^{+0.77}_{-4.02}$	1.9	84
J2145−0750	`-group CPSR2_50CM`	$-12.35^{+0.09}_{-0.08}$	$0.53^{+0.31}_{-0.22}$	16.9	31
	`-group PDFB_20CM`	$-13.05^{+0.05}_{-0.09}$	$0.65^{+0.40}_{-0.17}$	3.4	65
J2241−5236	`-B 20CM`	$-13.47^{+0.05}_{-0.06}$	$0.65^{+0.25}_{-0.18}$	6.3	49

Table 4.3: Results for chromatic noise parameter estimation and model selection. The second column is the chromaticity of the red process, the third and the fourth columns are parameters of the power-law spectrum. The last column is the ln Bayes factor in favor of chromatic noise over the hypothesis of just white noise, spin noise and DM noise.

Pulsar	χ	$\log_{10} A$	γ	$\log\mathscr{B}$
J0437−4715	4	$-14.36^{+0.07}_{-0.13}$	$2.35^{+0.56}_{-0.29}$	286.5
J0613−0200	4	$-13.98^{+0.06}_{-0.04}$	$1.90^{+0.20}_{-0.17}$	11.1
J1017−7156	2.39	$-12.96^{+0.07}_{-0.02}$	$2.63^{+0.29}_{-0.22}$	3.9
J1045−4509	1.82	$-12.37^{+0.05}_{-0.03}$	$2.88^{+0.20}_{-0.25}$	3.2
J1939+2134	4	$-14.32^{+0.10}_{-1.51}$	$3.25^{*\,+2.14}_{-1.20}$	4.7

of a hypothesis that excludes spin noise. For example, in PSR J1713+0747, with steep band noise in 10 cm and 20 cm data ($\gamma \approx 4$), the current model is preferred over a model with spin noise and 40-cm band noise with only a $\ln\mathscr{B}$ of 2. Generally speaking, if one is interested in studying spin noise to infer inner the workings of neutron stars, we recommend strengthening the requirement for the evidence in favour of the absence of chromaticity of the red process, while also assuming that band and system noise could contain the missing spin noise just because some other marginally-preferred term is not in the noise model. Otherwise, the noise might not be intrinsic to the pulsar. For example, one could require a minimum threshold on Bayes factor in favour of spin noise over each band noise component. Another suggestion would be to choose different priors for spin noise and band noise, as well as to fine-tune model selection by establishing prior odds. At the same time, for the purpose of gravitational-wave searches, it is justified to use Table 4.1 as a guide on whether to include spin noise in pulsar noise models. We also find that spin noise processes in PSR J0711−6830 and PSR J1643−1224 have $\gamma_{\rm SN} \approx 1$, although there is a significant evidence that this noise process is not band-specific.

For the remaining pulsars with spin noise, we find evidence for steep red spectra, with power-law indices between 4 and 10. For example, we measure $\gamma_{\rm SN}$ consistent with 7 for PSR J1857+0943. Similarly, for young pulsars, Parthasarathy et al. (2019) measured steep red noise with power-law indices between 2 and 10. In the timing analysis of the NANOGrav 11 year data set Arzoumanian et al. (2018b), the spectral index of observed red noise slope ranged between 1 and 3, which is why the authors suggested that the physical process is distinct from spin noise. According to Lentati et al. (2016), these results could be influenced by the absence of band-specific and system-specific red noise processes in pulsar noise models.

4.4.2 Dispersion measure variations

We find evidence for stochastic DM noise in 23 of the pulsars. PSR J1017−7156 and PSR J1045−4059 favour chromatic noise with a frequency-dependent index $\chi \approx 2$, the value expected from DM

noise. More details will be provided in Section 4.4.8 below. In PSR J0613−0200, we do not find evidence with $\ln \mathscr{B} > 3$ in favour of stochastic DM noise. We do find evidence of annual DM variations in PSR J0613−0200, which is consistent with previous studies by Keith et al. (2013). Moreover, in PSR J0613−0200 we find evidence for chromatic noise with $\chi = 4$, which we attribute to scattering variations in the interstellar medium. Given that the chromatic index χ has not been widely explored as a free parameter in the past, we suspect that DM noise previously observed in PSR J0613−0200 (i.e., in Lentati et al. 2016), had been, in fact, a chromatic noise. Moreover, the spectral index, $\gamma_{\rm DM}$, for PSR J0613−0200, found in Lentati et al. (2016), is consistent with $\gamma_{\rm CN}$ for PSR J0613−0200 in our work.

In PSR J1939+2134 and PSR J0437−4715, we find evidence for both stochastic DM noise and chromatic noise. Chromatic noise for these pulsars will be discussed in more detail the following subsections.

In the NANOGrav 11-year timing analysis by Arzoumanian et al. (2018b), DM variations were modeled by independently measuring dispersion for each epoch. We defer a comparison of these DM time series to our maximum-likelihood DM noise reconstructions to future work. Annual DM variations of PSR J0613−0200, low-frequency band noise in PSR J1939+2134 (PSR B1937+21), and a DM event for PSR J1713+0747 are all clearly seen in the dispersion measure time series presented in Arzoumanian et al. (2018b).

In addition to DM variations, DR2 pulsar timing models include first and second time-derivatives of dispersion measure (`DM1` and `DM2`), which absorb long-term variations in dispersion measure. We measure significant `DM1` values $\sim 10^{-3}$ [cm^{-3} pc yr^{-1}] in PSRs J0613−0200, J1017−7156, J1045−4509, J1643−1224 and J1824−2452A, and significant `DM2` values on the order of $\sim 10^{-4}$ [cm^{-3} pc yr^{-2}] in PSRs J1732−5049 and J1832−0836. For PSR J1824−2452A we measure the highest value of DM and the highest amplitude of stochastic DM variations.

4.4.3 Band noise and system noise

In an analysis of IPTA DR1, Lentati et al. (2016) found evidence for band and system noise terms. We also find evidence for these processes in PPTA DR2. Our measurements of band noise are provided in Table 4.2. In particular, Lentati et al. (2016) found that PSRs J0437−4715, J1600−3053, J1643−1224 and J1939+2134 have band noise processes at low frequencies, which we also see in PPTA DR2. Unlike Lentati et al. (2016), we do not find evidence for band noise in 10-cm band and system noise in `CPSR2_20CM` for PSR J1939+2134; however, we observe new chromatic noise in this pulsar, as discussed below. We observe that PSR J1600−3053 has band noise in 20-cm data. In PPTA DR2, we also find more pulsars to show evidence of band and system noise. Unlike spin noise, in most band and system noise cases, the processes are found to have very shallow (nearly white) power-law spectra, as seen in Figure 4.1. Of the 27 measured power-law indices for band and system noise, 17 pulsars possess an index $\gamma < 1$.

There are a few potential sources of systematic error that may contribute to this noise. It is

possible that it arises from polarisation calibration. Highly polarised pulsars are more susceptible to this form of noise. Radio frequency interference is another possible origin. PSR J1022+1001 has been known to have errors in polarisation calibration (Kramer et al., 1999), resulting in so-called ToA drop-outs, which result in outlying residual arrival times in the 10-cm and 20-cm observations. We suggest that the high-frequency noise in these bands to possible polarisation calibration errors. One possible origin for the high-frequency system noise in `CPSR2_50CM`, is residual radio-frequency interference.

Additionally, the solar wind is known to contribute to pulsar timing noise (Madison et al., 2019; You et al., 2007). PSR J1022+1001 lies close to the ecliptic plane, which is where density of the solar wind along the line of sight to the pulsar is higher. Given the time scale on which angle between the line of sight to the pulsar and the Sun changes, some contributions to high-frequency band and system noise could be influenced by the solar wind if DM is not properly modeled. Stochasticity in the solar wind unaccounted for in noise noise models (Tiburzi et al., 2019) introduces another potential source of noise.

4.4.4 PSR J1643–1224: profile event, band noise

The DM ($\approx 62.4\,\mathrm{pc\,cm^{-3}}$) makes PSR J1643−1224 one of the more susceptible to noise introduced by propagation effects. However the most unusual feature in its arrival time is unlikely to have originated in the interstellar medium. Between 2015 and 2016, PSR J1643−1224 exhibited a sudden change in pulse shape (Shannon et al., 2016), which caused the same evolution of timing residuals. Interestingly, the event was most pronounced at high radio frequency. Shannon et al. (2016) suggested that this event originated in the pulsar magnetosphere, because the spectral properties were inconsistent with being a propagation effect, and the presence in multiple bands and instruments made it inconsistent with being a telescope dependent effect. In our work, we estimate the chromaticity of the event to be $\chi = -0.99^{+0.10}_{-0.11}$, consistent with the inverted spectrum noted by Shannon et al. (2016). In this work, we find that the profile event in PSR J1643−1224 must be taken into account, in order not to be confused with a red process in 10-cm and 20-cm data. The event was also identified in the NANOGrav 11-year data set. However because of their lower frequency data and dual-frequency observations, they were unable to establish its chromaticity (Brook et al., 2018). Additionally, we find that J1643−1224 shows evidence of red noise process in 40-cm and 50-cm observations.

4.4.5 PSR J1713+0747: DM event, profile event, system noise, band noise

Previous studies have found that PSR J1713+0747 has shown two exponential events. The first event, which started at approximately MJD 54750, was observed as a sudden decrease in dispersion measure by Keith et al. (2013), and discussed in detail in Coles et al. (2015); Desvignes et al. (2016); Jones et al. (2017). A second event, at approximately MJD 57510, has been reported in Lam et al. (2018). It shows deviations from $\chi = 2$, which is the index for DM-related radio pulse

(a) PSR J0613−0200: red noise reconstruction

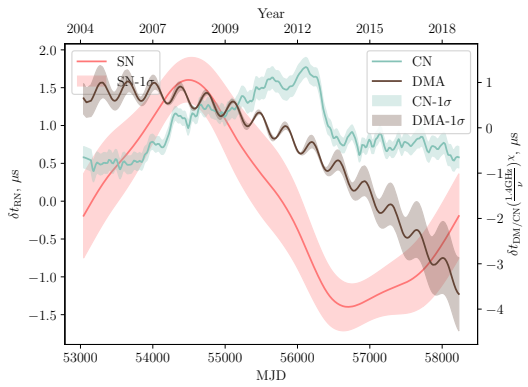

(b) PSR J0613−0200: chromatic noise parameters

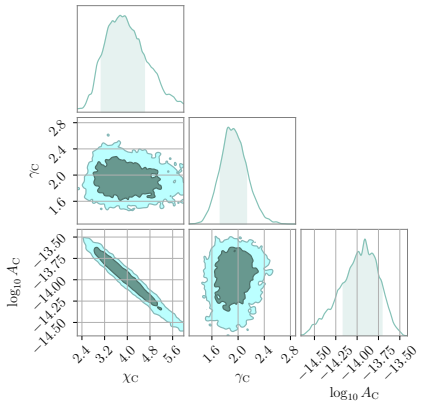

(c) PSR J1939+2134: red noise reconstruction

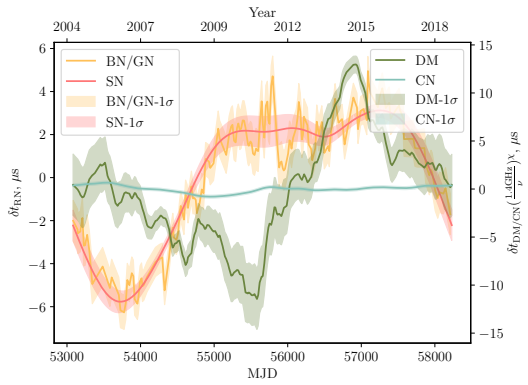

(d) PSR J1939+2134: chromatic noise parameters

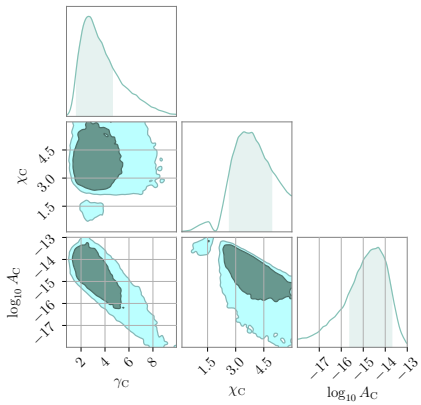

FIGURE 4.2. Noise models for pulsars with chromatic red noise with $\chi \approx 4$. Noise with this chromatic index would be expected from scattering variations in the interstellar medium. On the left two panels (4.2(a) and 4.2(c)) we present maximum-likelihood realization of spin noise (red), band and system noise (yellow), DM noise (green), chromatic noise (turquoise) and annual DM noise on top of the first and the second time derivatives of the dispersion measure (brown). We do not find evidence with ln Bayes factor of above three for stochastic DM noise in J0613−0200, but we do find evidence of annual DM variations in this pulsar. On the right two panels (4.2(b) and 4.2(d)) we present posterior distributions for chromatic noise power-law parameters $A_C \propto \nu^{-\chi_C}$ and γ_C, where ν is a radio frequency.

time delays. We include both of these events into the noise model of PSR J1713+0747. We found the chromatic index of the second event to be $\chi = 1.15^{+0.18}_{-0.19}$. This, and the observation of a pulse shape change at the time of the event (Figure 4.5(c)), points to the magnetospheric origin. We do not find evidence for pulse shape changes for PSR J1713+0747 at the time of the first exponential event. In addition to exponential events, we find evidence of system noise in `CPSR2_20CM` and `CPSR2_50CM`. We also find evidence of band noise in 10-cm and 20-cm data.

4.4.6 PSR J0613–0200: scattering variations, annual dispersion measure variations

In PSR J0613−0200, we find evidence of scattering variations in the interstellar medium, as a red process, with an amplitude roughly proportional to radio-frequency to the power of −4: $A_{\rm C} \propto \nu^{-4}$. We also find evidence of the annual DM signal, described by Equation 4.9. The detection of annual DM variations is consistent with Keith et al. (2013). We do not find any additional evidence for stochastic DM variations in PSR J0613−0200, suggesting the DM(t) is well modelled by the annual and quadratic terms. Reconstruction of the red noise in PSR J0613−0200 using the maximum-likelihood method is provided in Figure 4.2(a). Posterior distribution for chromatic noise parameters is in Figure 4.2(b).

4.4.7 PSR J1939+2134: scattering variations, band noise

Pulsar PSR J1939+2134 is known as a pulsar with strong DM variations and spin noise. In this study, we find that PSR J1939+2134, like PSR J0613−0200, exhibits chromatic noise with an amplitude: $A_{\rm C} \propto \nu^{-4}$. This, again, suggests the cause may be scattering variations towards the line of sight to the pulsar. With a narrow pulse profile and high dispersion, the pulsar is expected to show multipath propagation effects (Ramachandran et al., 2006). Posterior distribution for chromatic noise parameters is presented in Figure 4.2(d). Additionally, we find evidence of band noise in 40-cm and 50-cm observations. We reconstruct red noise processes in PSR J1939+2134 in Figure 4.2(c).

4.4.8 PSR J1017−7156 and PSR J1045−4509: chromatic noise, dominated by DM variations

In PSR J1017−7156, we find a chromatic noise with $\chi = 2.39$, which is close to what we expect from DM variations. Additionally, for PSR J1017−7156, we find the presence of band noise in 20-cm data. In PSR J1045−4509 we also find a similar chromatic noise with $\chi = 1.82$. When chromatic noise is included in the noise model, we find no evidence of DM noise in these two pulsars. We find $\ln\mathscr{B}$ in favour of excess chromatic noise in addition to DM are 3.9 and 3.2 for PSR J1017−7156 and PSR J1045−4509, respectively. We interpret these noise processes, as dispersion measure variations on a similar time scale as scattering of radio pulses in the

(a) PSR J1017−7156: red noise reconstruction

(b) PSR J1017−7156: chromatic noise parameters

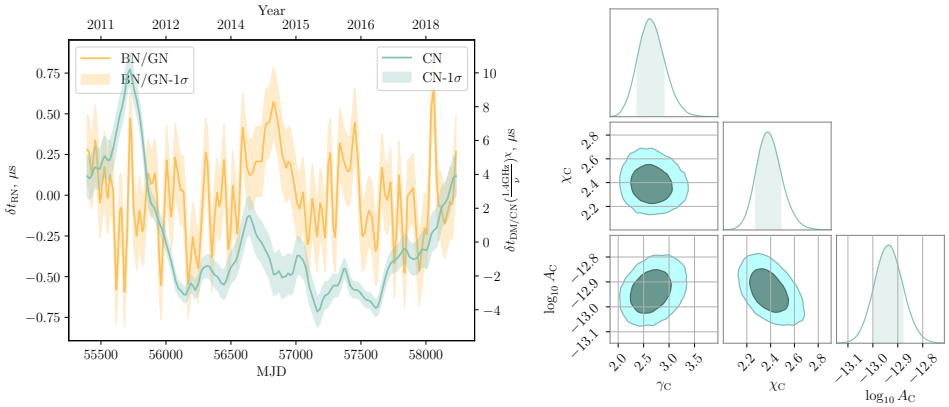

(c) PSR J1045−4509: red noise reconstruction

(d) PSR J1045−4509: chromatic noise parameters

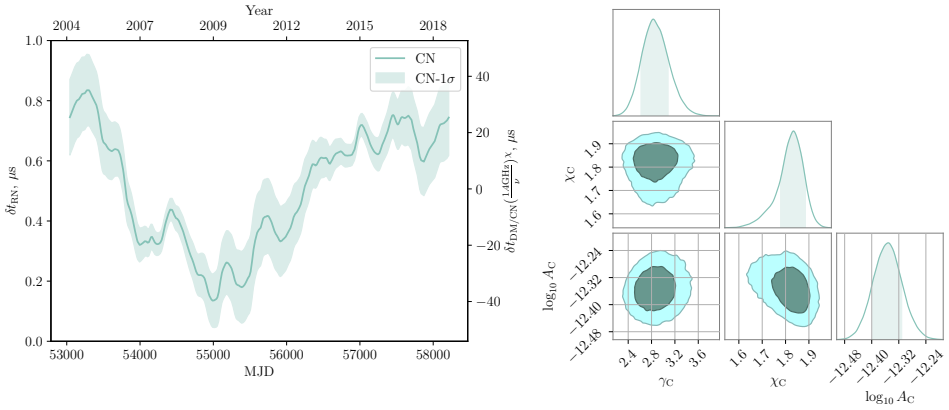

FIGURE 4.3. In this figure, we present our results for two pulsars, J1017−7156 and J1045−4509, where we find chromatic noise (turquoise), with the chromaticity close to what is expected for dispersion measure variations. Noise realizations are displayed on the left two panels (4.3(a), 4.3(c)), posterior distributions for chromatic noise parameters are on the right two panels (4.3(b), 4.3(d)). J1017−7156 additionally has evidence for band noise in 20-cm data (yellow).

interstellar medium. In Figure 4.3, we provide maximum-likelihood reconstructions of the chromatic noise in PSR J1017−7156 and PSR J1045−4509, as well as posterior distributions for chromatic noise parameters.

4.4.9 PSR J2145–0750: an achromatic exponential dip

The initial maximum-likelihood red noise realisation of PSR J2145−0750 contained a dip in timing residuals, like the ones found in PSRs J0437−4715, J1713+0747 and J1643−1224. We found $\ln \mathscr{B} \approx 30$ in favour of the exponential dip on top of known red noise in PSR J2145−0750.

Results of parameter estimation for exponential dip parameters are presented in Figure 4.4(e). Unlike the other exponential dip events, the chromatic index χ for the one in PSR J2145−0750 is mostly consistent with zero. Additionally, we do not see any significant pulse profile residuals for PSR J2145−0750 at around the time of the event, which we show in Figure 4.5(a). The absence of pulse profile residuals could be either the consequence of its relatively slow spin period (16 ms) or a different origin of the exponential dip. In addition to the exponential dip, we find DM noise and high-frequency spin noise and system noise in the pulsar.

4.4.10 PSR J0437–4715: profile evolution, profile events, scattering variations, band and system noise

PSR J0437−4715 is by far the brightest millisecond pulsar at metre and centimetre wavelengths. Its short term timing is severely limited by pulse jitter and self noise effects (Osłowski et al., 2011b). The pulsar is also susceptible to additional instrumental noise, introduced through pulse profile distortions. Because of its brightness, the profile can experience distortions, particularly when observed with the early backends which had low bit depth. The level of the distortions would depend on both frequency and date as the pulsar is subject to diffractive and refractive scintillation. The polarisation shows rapid changes in time in the region of pulse phase close to the peak of the pulse profile (Dai et al., 2015).

In PPTA-DR2, PSR J0437−4715 has the longest data span because of the availability of early CPSR2 data. The timing data contains two main important features that we present and try to account for.

The first one is related to the evolution of pulse profiles. After least-squares fitting of the data to the timing model of DR2, we identified a clear linear dependence of timing residuals on radio-frequency for observing systems, as well as sub-systems, described in Section 4.3.3.4. We conclude that regular `FD` parameters in the timing model for PSR J0437−4715 do not allow this effect to be properly taken into account, and we introduced the linear residual-frequency model in Equation 4.10 to serve this purpose. Before performing model selection for band and system noise, we perform model selection for system-specific frequency dependence. We find evidence for linear dependence of residuals on radio frequency in these systems: `PDFB_20CM`, `CPSR2_50CM`, `CASPSR_40CM`, `PDFB1_early_20CM`, `WBCORR_10CM`, `PDFB1_1433`, `PDFB1_10CM`, `PDFB_40CM`, `CPSR2_10CM`, `WBCORR_10CM` with 512 MHz bandwidth. Therefore, we include linear dependence of timing residuals on radio frequency for the above systems into the noise model of PSR J0437−4715.

The second feature is the sudden change in the timing residuals of PSR J0437−4715 around MJD 57070, which is correlated with a change in the pulse profile. In Figure 4.5, we plot the evolution of timing residuals and profile residuals, to demonstrate the clear connection between the two. In our model selection, we include profile event, modelled by Equation 4.7. Otherwise, the profile event will be absorbed in stochastic component of the noise. We find the chromaticity

(a) PSR J0437−4715: red noise reconstruction

(b) PSR J0437−4715: chromatic noise parameters

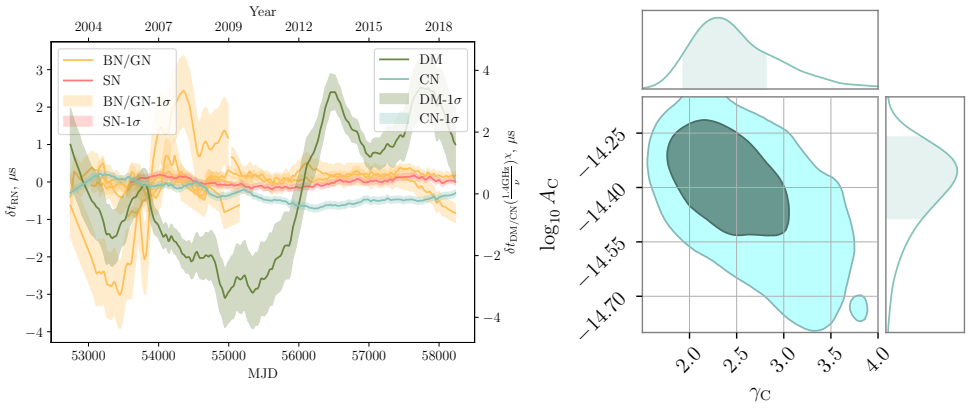

FIGURE 4.4. On the left panel (4.4(a)) we present maximum-likelihood realization of spin noise (red), band and system noise (yellow), chromatic noise (turquoise) and DM noise (green) for PSR J0437−4715. On the right panel (4.4(b)) we present posterior distribution for chromatic noise power-law parameters $A_{\rm C}$ and $\gamma_{\rm C}$. Due to the largest amount of data and the most complicated noise model for J0437−4715 in DR2, it is computationally challenging to produce a posterior distribution that would include the chromatic index χ. We found χ consistent with 4 for this pulsar empirically.

of the event to be consistent with zero. In Figure 4.5(a) we added an additional observation for J0437−4715 at around the time of the event, which was initially flagged as an RFI and looks like a hint of a yellow dot behind the red line. Later we found that this observation causes an advance in pulse arrival time across all three radio bands, which is not consistent with a typical RFI. The timing residuals for this observation also line up with the exponential event. Thus, there is a reason to consider this observation the earliest observation of the exponential dip, associated with the profile event. The additional observation, which took place at MJD 57073, also separates exponential events for J0437−4715 and J1643−1224 in time. Initially, errors for event time estimates were overlapping, which may seem like a spurious coincidence. The additional observation for J0437−4715 narrows down the uncertainty, whereas MJD 57073 is ruled out by the data from PSR J1643−1224.

Compared to the other PPTA pulsars, PSR J0437−4715 shows the largest number of red noise processes. In the IPTA DR1 data set, Lentati et al. (2016) found evidence of band noise in all bands and system noise in `CPSR2_20CM`. In PPTA-DR2, consistent with Lentati et al. (2016), we find evidence of red noise in `CPSR2_20CM` system, and we also find red noise in three additional systems: `WBCORR_10CM`, `CPSR2_10CM`, `CPSR2_50CM`. We also find evidence of band noise in both 20-cm and joint 40-50-cm data. On top of that, we find excess chromatic noise with χ consistent with 4. Maximum-likelihood reconstruction of the red noise in PSR J0437−4715, as well as the posterior distribution for power-law parameters of the chromatic noise, are provided in Figure 4.4.

PSR J0437−4715 has the lowest DM in the PPTA data set. It is surprising to identify chromatic noise with a chromactic index close to what would be expected from scattering variations. However this frequency scaling is consistent with what would be predicted from angle of arrival variations (Cordes and Shannon, 2010; Romani et al., 1986). An alternative possible origin of the chromatic noise could be in the evolution of pulse profile. Our red noise analysis was conducted after fitting for a second derivative of pulsar spin frequency, F2.

Given its high timing precision, PSR J0437−4715 provides great sensitivity to gravitational waves. Future improvements to the noise model for PSR J0437−4715 and profile-domain timing analyses would provide further answers about the origin of chromatic noise in this pulsar.

4.4.11 Evaluating the performance of the noise models

We can further test our models by analyzing the distribution of timing residuals after the subtraction of maximum-likelihood realisations of red noise. We normalise timing residuals by dividing them by the corresponding ToA errors. If the models well describe the data we would expect these residuals to be consistent with Gaussian distribution with zero mean and unit variance. We perform three tests to determine how Gaussian, uncorrelated and variance-stationary are whitened residuals of PPTA-DR2 pulsars. The results are summarized in Table 4.4. We carry out the Anderson and Darling (1952) test to determine if the distribution of timing residuals is consistent with Gaussian distribution with zero mean and unit variance. We find significant non-Gaussianity only for PSR J0437−4715, which has a probability of whitened timing residuals being drawn from such distribution of less than 1%. The distribution of whitened residuals of PSR J0437−4715 has a mean of 0.05 and standard deviation of 1.12. The increased standard deviation could mean that EFAC and EQUAD parameters are insufficient to describe the white noise in PSR J0437−4715. We also test how white are the actual whitened timing residuals with the help of the statistic derived by Ljung and Box (1978). Nine PSRs, J0437−4715, J1017−7156, J1022+1001, J1125−6014, J1744−1134, J1824−2452A, J1909−3744, J2124−3358, J2241−5236, have a probability of being uncorrelated in time of less than 1%. Moreover, with the Breusch and Pagan (1979) test, we find that whitened residuals for PSRs J0437−4715 and J2241−5236 have a probability of having temporally stationary variance[2] of less than 1%. Overall, nine pulsars did not pass the three tests we discussed in this paragraph. Eight of these pulsars have band or system noise, described in Table 4.2 and Section 4.4.3, with $\gamma < 0.5$. This is not a coincidence, as nearly flat power spectrum indicates that a power law might not be the best model to describe these noise processes. For the ninth pulsar, PSR J2124−3358, we found evidence for band noise in 20-cm data with $\gamma \approx 8$, although we do not rule out that this low-frequency red noise is pulsar spin noise (see discussion in Section 4.4.1). We defer the further improvement of noise models for the above nine pulsars to future work.

[2]homoskedasticity

Table 4.4: Tests of the noise models. The second column shows Anderson-Darling statistic (ADS), with the null hypothesis that the whitened timing residuals are described by a Gaussian distribution with zero mean and unit variance. Values smaller than 2.5 are within 95-% confidence intervals and values smaller than 3.9 are within 99-% confidence intervals (Stephens, 1974). Only PSR J0437−4715 has the statistic value greater than 3.9. The third column shows Ljung–Box statistic (LBS), with the null hypothesis that the whitened timing residuals are uncorrelated in time. The fourth column reports the p-values (LBp) that correspond to the Ljung–Box statistic values. We choose a number of Ljung–Box lags to be equal to n_c, listed in Table 4.1. For nine PPTA PSRs we obtain a probability of whitened residuals of being uncorrelated in time of less than 1%: J0437−4715, J1017−7156, J1022+1001, J1125−6014, J1744−1134, J1824−2452A, J1909−3744, J2124−3358, J2241−5236. The last two columns contain Breusch-Pagan statistic and corresponding p-values, with the null hypothesis that variance of the whitened timing residuals is constant in time. Only two PSRs, J0437−4715 and J2241−5236, have a statistically-significant probability of having non-stationary excess variance.

PSR	ADS	LBS	LBp	BPS	BPp
J0437−4715	15.4	24042	≈ 0	26.1	3×10^{-7}
J0613−0200	0.2	93	3×10^{-1}	0.0	8×10^{-1}
J0711−6830	0.4	82	6×10^{-1}	0.0	9×10^{-1}
J1017−7156	1.2	139	5×10^{-11}	2.2	1×10^{-1}
J1022+1001	1.5	527	1×10^{-64}	0.0	8×10^{-1}
J1024−0719	0.2	113	2×10^{-2}	0.0	9×10^{-1}
J1045−4509	1.2	83	6×10^{-1}	0.2	7×10^{-1}
J1125−6014	0.7	204	8×10^{-14}	4.3	4×10^{-2}
J1446−4701	0.4	67	1×10^{-2}	0.1	7×10^{-1}
J1545−4550	0.4	41	5×10^{-1}	0.7	4×10^{-1}
J1600−3053	0.6	83	6×10^{-1}	0.0	8×10^{-1}
J1603−7202	0.3	109	5×10^{-2}	4.4	4×10^{-2}
J1643−1224	0.4	99	2×10^{-1}	0.7	4×10^{-1}
J1713+0747	0.5	121	8×10^{-3}	0.2	7×10^{-1}
J1730−2304	0.5	86	5×10^{-1}	0.7	4×10^{-1}
J1732−5049	0.9	46	4×10^{-1}	0.6	4×10^{-1}
J1744−1134	1.7	179	2×10^{-8}	0.4	5×10^{-1}
J1824−2452A	0.2	151	8×10^{-6}	0.4	5×10^{-1}
J1832−0836	0.3	50	2×10^{-2}	0.0	9×10^{-1}
J1857+0943	1.3	83	6×10^{-1}	0.2	7×10^{-1}
J1909−3744	0.9	142	1×10^{-4}	0.3	6×10^{-1}
J1939+2134	1.1	132	8×10^{-4}	1.2	3×10^{-1}
J2124−3358	3.7	192	5×10^{-10}	0.1	8×10^{-1}
J2129−5721	0.3	55	1×10^{0}	2.0	2×10^{-1}
J2145−0750	2.2	109	4×10^{-2}	3.8	5×10^{-2}
J2241−5236	0.7	145	2×10^{-11}	18.7	2×10^{-5}

4.5 Conclusion

We have robustly determined noise models for the PPTA DR2 pulsars, which include models for red noise processes (Tables 4.3, 4.1, and 4.2) and specific models for deterministic signals, described throughout Section 4.4. These models can be used in timing analyses of the pulsars.

In our analysis we considered each pulsar independently. Therefore, our red noise models may have absorbed spatially correlated signals, such as the gravitational-wave background or errors in Solar System ephemeris. For example, the low fluctuation frequency red noise observed in PSRs J1713+0747 and J1909−3744 can possibly be attributed to this. Although the processes could still be detected with our noise models, either because of the fact that they are correlated between pulsars or because of the non-power-law model, some of our red noise terms may decrease the sensitivity to these signals one is interested in studying. This effect can be mitigated by the additional model comparison between the desired signal and such red noise terms in our noise models that are likely to be co-variant with the signal.

Due to the exceptional brightness and hence the high individual pulse signal-to-noise ratio of J0437−0715, pulse profile evolution becomes a significant noise component. We expect this source of noise will become even more important for data from high-sensitivity radio telescopes. An effective way to account for this noise is to perform profile-domain timing. The methodology has been outlined in Lentati et al. (2017).

We measured some band and system noise power-law indices to be nearly zero, which indicates that the power-law model might not be the best one to describe these noise processes.

Maximum-likelihood noise reconstructions and the tests, described in Table 4.4, complement Bayesian inference and provide an opportunity to validate noise models for current (Perera et al., 2019) and future IPTA data releases.

Chromatic effects will become more apparent with the deployment of future wide-band receiver systems. At Parkes, pulsar timing array observations are being undertaken with the ultrawide-band (low) receiver at Parkes (Hobbs et al., 2020b), which records data over a contiguous band from 700 MHz to 4.2 GHz. The MeerTime project (Bailes et al., PASA, submitted) is currently conducting sensitive observations of millisecond pulsars over an octave bandwidth. Wide-band systems are planned or proposed for many additional telescopes as well.

Acknowledgements

We thank William A. Coles for useful comments on the paper. The Parkes radio telescope is part of the Australia Telescope, which is funded by the Commonwealth Government for operation as a National Facility managed by CSIRO. This paper includes archived data obtained through the Australia Telescope Online Archive and the CSIRO Data Access Portal (data.csiro.au). E.T. acknowledges Australian Research Council grant FT150100281. M.B., R.M.S, and R.S. acknowledge Australian Research Council grant FL150100148. R.M.S. also acknowledges funding support

through Australian Research Council Future Fellowship FT190100155. Parts of this research were conducted by the Australian Research Council Centre of Excellence for Gravitational Wave Discovery (OzGrav), through project number CE170100004. J.W. is supported by the Youth Innovation Promotion Association of Chinese Academy of Sciences. Work at NRL is supported by NASA. This research has made use of NASA's Astrophysics Data System.

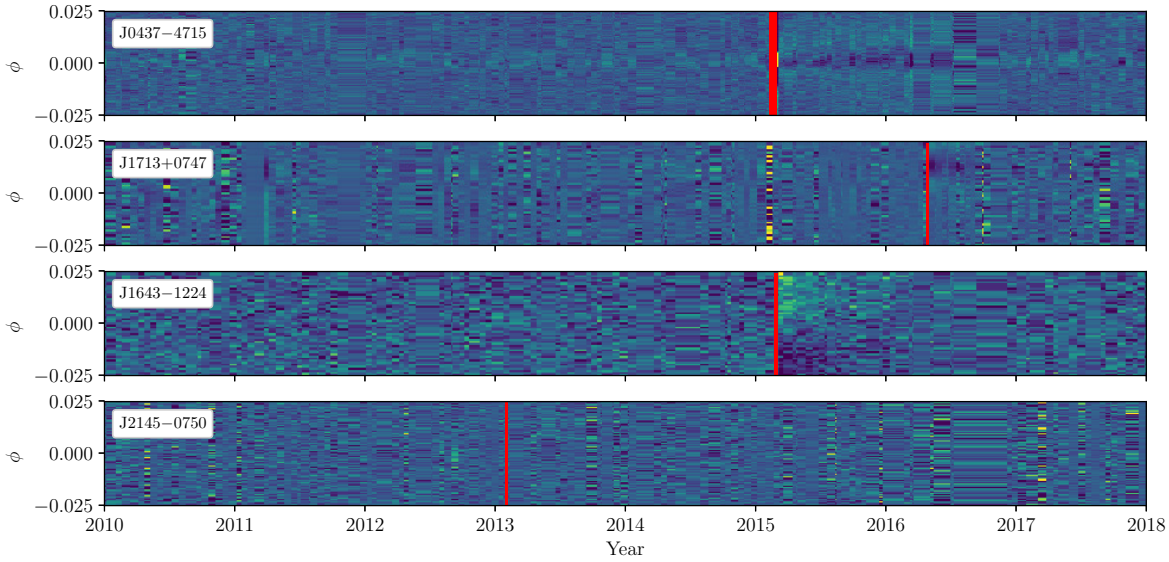

(a) Pulse profile residuals

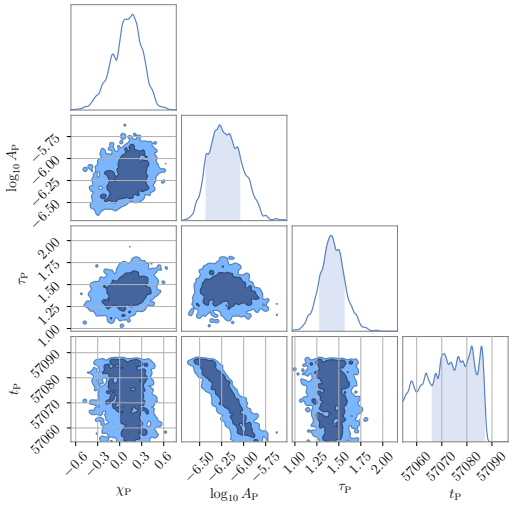

(b) PSR J0437−4715

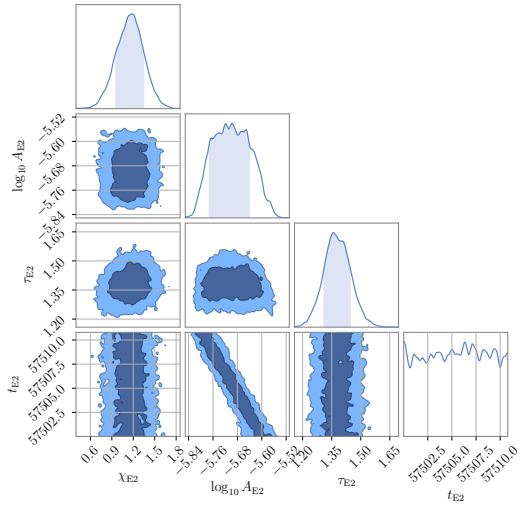

(c) PSR J1713+0747

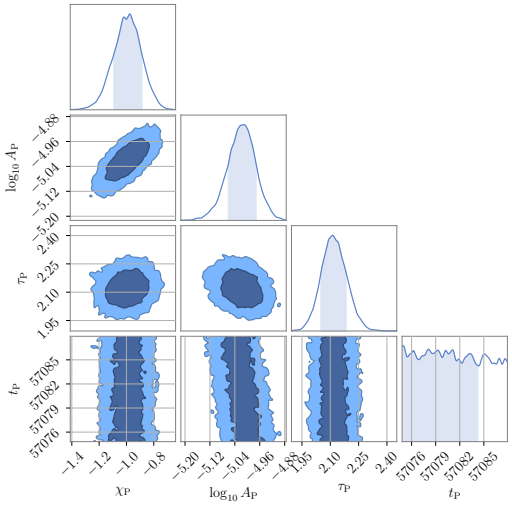

(d) PSR J1643−1224

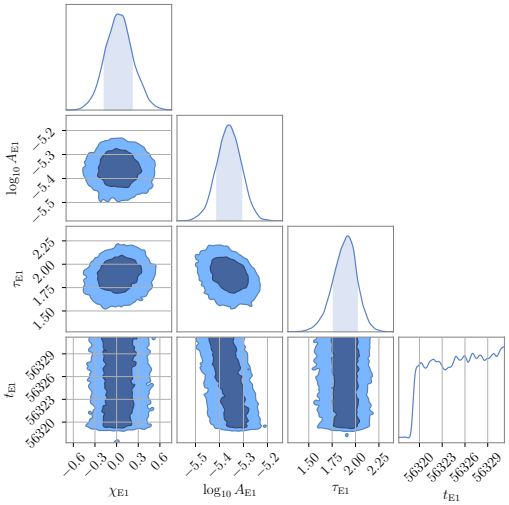

(e) PSR J2145−0750

FIGURE 4.5. Exponential dips and profile shape events. Top panel (4.5(a)): profile residuals (colour) as a function of pulse phase (ϕ) and year from PDFB4 observations for PSRs J0437−4715 (10 cm), J1713+0747 (20 cm), and J1643−1224 (10 cm). Red vertical lines correspond to the 1-σ credible intervals of inferred start times of chromatic exponential dips in the timing residuals. We also include J2145−0750, where we identified an apparent exponential dip with χ consistent with zero. In panels below (4.5(b),4.5(c),4.4(d),4.4(e)), we provide posterior distributions for inferred exponential dip parameters: the time of the event t, the chromatic index χ, the duration τ, the amplitude A [s].

CHAPTER 5

SUMMARY

The work outlined in this Ph.D. thesis provided a pathway to new searches for gravitational waves with both ground-based laser interferometers and pulsar timing arrays. The radiometer method can now be applied to the data from ground-based interferometers to search for persistent gravitational waves over all sky directions and frequencies. We performed the analysis of millisecond pulsar spin noise in the first data release of the International Pulsar Timing Array and found that the superfluid turbulence model for spin noise, derived by Melatos and Link, is not sufficient to describe spin noise in all pulsars. We also found no evidence for a hypothesised low-frequency turnover in millisecond pulsar spin noise power spectrum. Additionally, we identified noise properties of the second data release of the Parkes Pulsar Timing Array. The future work will use our noise models to perform nanohertz gravitational wave searches with the data set. Furthermore, we developed new methods to characterize timing properties of millisecond pulsars and unknown signals in the data. We identified new timing noise processes in pulsar timing arrays and discussed possible origins of these processes.

We propose the further development of the all-sky radiometer to become fully Bayesian as a subject of future work. The Bayesian implementation will make the radiometer a useful tool to ask astrophysically interesting questions about the nature of galactic neutron stars. Data folding, which enabled the all-sky radiometer, can also be applied to isotropic radiometer and spherical harmonic decomposion methods to search for gravitational-wave backgrounds.

During the analysis of the Parkes Pulsar Timing Array data, we found that in some pulsars one can not confidently determine whether the red noise is spin noise or band- or system-dependent process. It is also expected that some of the red noise is caused by errors in Solar System ephemerides. Thus, future spin noise studies will need to take that into account. Additionally, we propose to consider more physical models of spin noise in future work. Better

understanding of spin noise will be beneficial for gravitational-wave searches and will help to infer the dynamical processes in neutron star interiors.

We expect the new chromatic noise we found in the Parkes data to become more apparent in the upcoming wide-band data sets. This noise can potentially be mitigated using the profile-domain timing techniques, which provides means to use more tailored pulse profiles, to model interstallar propagation effects, such as scattering, as well as to better model pulse shape variability. This research will enable even more sensitive nanohertz gravitational-wave searches in the future.

APPENDIX

A.1 Explicit form of Model M power spectral density

The definite integral in Equation 3.15 yields an analytical solution. First, we reparametrize Equation 3.15:

$$\begin{cases} M = \frac{15}{(4\pi\lambda)^2} \ ; \\ t_c = \frac{2\pi}{\eta(R^{-1})} \ . \end{cases} \tag{A.1}$$

Next, we obtain the analytical solution in a form:

$$\begin{aligned} P(f) = \frac{3Mp^2}{4t_c f^2}\Bigg(& \frac{1}{128\sqrt{[}3]2\pi^{16/3}} + \frac{3}{704\sqrt{[}3]2\pi^{22/3}} + \frac{9}{3584\sqrt{[}3]2\pi^{28/3}} - \\ & \frac{1}{f^2 t_c^2}\left(\frac{1}{48\pi^4} + \frac{1}{96\pi^6} + \frac{3}{512\pi^8}\right) + \\ & \frac{1}{f^4 t_c^4}\left(\frac{1}{82^{2/3}\pi^{8/3}} + \frac{3}{562^{2/3}\pi^{14/3}} + \frac{9}{3202^{2/3}\pi^{20/3}}\right) - \\ & \frac{1}{f^6 t_c^6}\left(\frac{1}{2\sqrt{[}3]2\pi^{4/3}} + \frac{3}{20\sqrt{[}3]2\pi^{10/3}} + \frac{9}{128\sqrt{[}3]2\pi^{16/3}}\right) + \\ & \frac{1}{f^8 t_c^8}\left(\frac{1}{2\pi^2} + \frac{3}{16\pi^4} - \frac{4\log(\pi)}{3} - \log 4\right) - \\ & \frac{1}{f^{10} t_c^{10}}\left(\frac{3\sqrt{[}3]2}{\pi^{2/3}} + \frac{9}{82^{2/3}\pi^{8/3}}\right) + \\ & \frac{1}{f^{11} t_c^{11}} 6\tan^{-1}\left(\frac{t_c f}{(2\pi)^{2/3}}\right) + \frac{1}{f^{12} t_c^{12}} \frac{9}{2\sqrt{[}3]2\pi^{4/3}} + \\ & \frac{1}{f^{14} t_c^{14}}\Big(12\log(\pi) + 3\log(64)\Big)\Bigg) \end{aligned} \tag{A.2}$$

A.2 Posterior probability distribution examples

In Figure A.1 we demonstrate posterior distributions for spin noise parameters of two pulsars, J0621+1002 and J1939+2134, where the highest and the lowest $\log \mathscr{B}_{\mathrm{PL}}^{\mathrm{BPL},i}$ are found (see Table 3.3 for details).

(a) J0621+1002

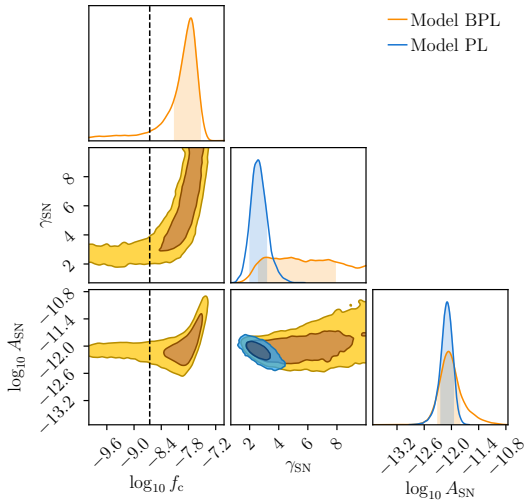

(b) J1939+2134

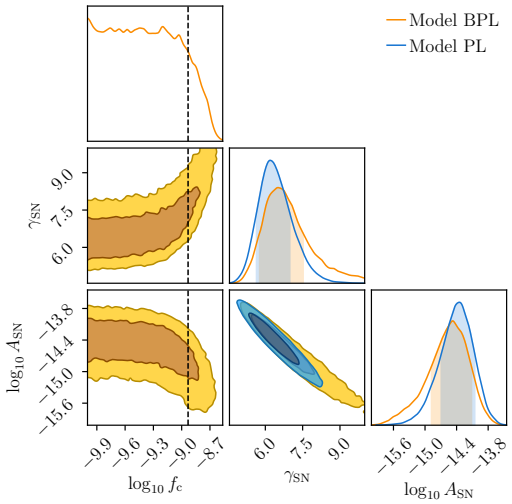

FIGURE A.1. Figure A.1 represents posterior distributions for spin noise parameters for J0621+1002 (left, A.1(a)) and J1939+2134 (right, A.1(b)). Vertical dashed lines represent $1/T_{\mathrm{obs}}$. For J1939+2134, with least evidence for the spectral turnover in Table 3.3, measurement of f_{c} does not affect the measurement of the amplitude and the slope of spin noise. However, for J0621+1002, with the highest evidence for the spectral turnover in Table 3.3, measurement of f_{c} does affect measurement of the power-law index.

A.3 Prior probability distributions for the PPTA DR2 noise model selection

Table A.1: Priors used for our model selection study. In the top five rows of the table we list priors for stochastic signals, described in Section 4.3.2. In the remaining rows, we list priors for deterministic signals, described in Section 4.3.3.

Parameter $\boldsymbol{\theta}$ [unit]	Pulsar	Prior $\pi(\boldsymbol{\theta})$
EFAC	all	$\mathscr{U}(0.01, 10)$
EQUAD [s]	all	$\log_{10} \mathscr{U}(10^{-8.5}, 10^{-5})$
A	all	$\log_{10} \mathscr{U}(10^{-20}, 10^{-8})$
γ	all	$\mathscr{U}(0, 10)$
χ	all	$\mathscr{U}(0, 6)$
A_{E} [s]	all	$\log_{10} \mathscr{U}(10^{-10}, 10^{-2})$
t_{E} [MJD]	J1713+0747 (1)	$\mathscr{U}(54500, 54900)$
	J1713+0747 (2)	$\mathscr{U}(57500, 57520)$
	J1643−1224	$\mathscr{U}(57050, 57150)$
	J0437−4715	$\mathscr{U}(57050, 57150)$
	J2145−0750	$\mathscr{U}(56100, 56500)$
χ_{E}	all	$\mathscr{U}(-7, 7)$
$\log_{10} \tau_{\mathrm{E}}$ [MJD]	J1713+0747 (1)	$\mathscr{U}(\log_{10} 5, 3)$
	all	$\mathscr{U}(\log_{10} 5, 2)$
A_{G} [s]	J1603−7202	$\log_{10} \mathscr{U}(10^{-6}, 10^{-1})$
t_{G} [MJD]	J1603−7202	$\mathscr{U}(53710, 54070)$
σ_G [MJD]	J1603−7202	$\mathscr{U}(20, 140)$
A_{Y} [s]	all	$\log_{10} \mathscr{U}(10^{-10}, 10^{-2})$
ϕ_{Y}	all	$\mathscr{U}(0, 2\pi)$

A.4 Red noise reconstruction for the remaining PPTA DR2 pulsars

(a) J0711−6830

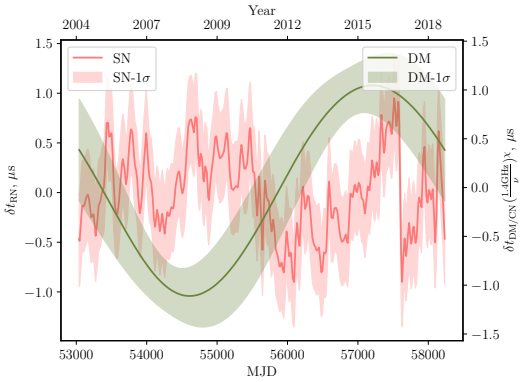

(b) J1022+1001

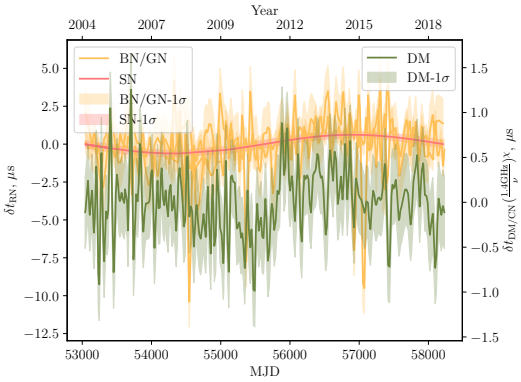

(c) J1024−0719

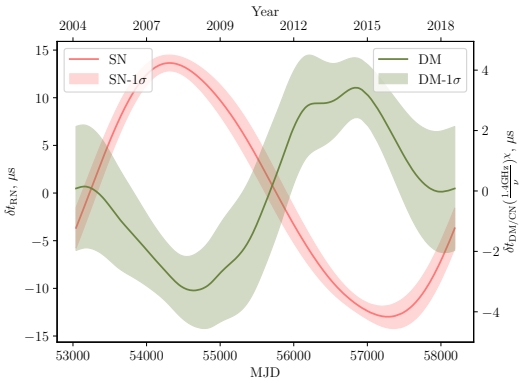

(d) J1125−6014

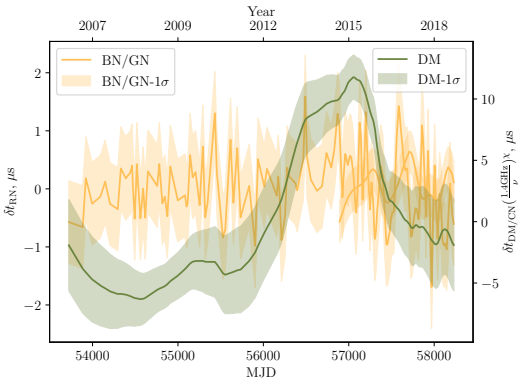

(e) J1446−4701

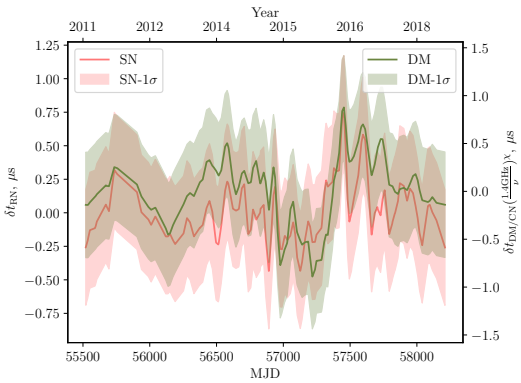

(f) J1545−4550

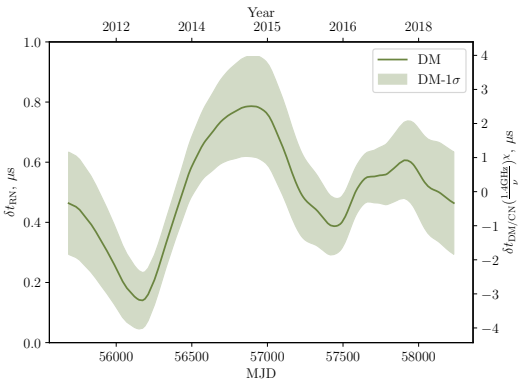

(g) J1600−3053

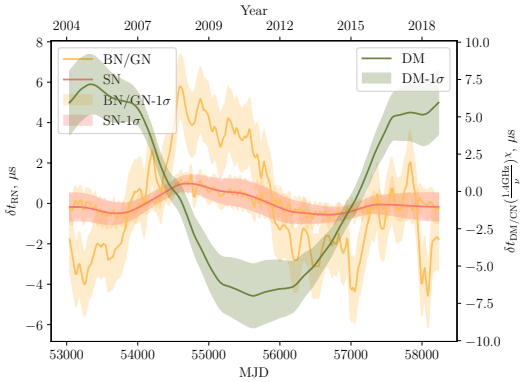

(h) J1603−7202

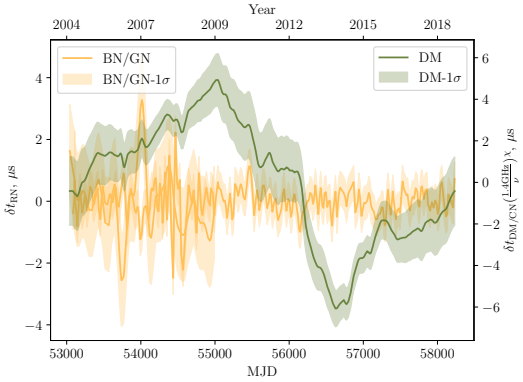

(i) J1643−1224

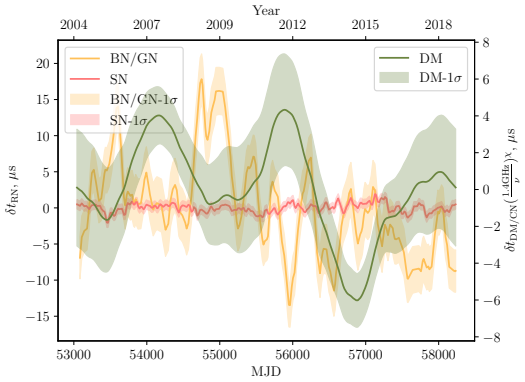

(j) J1713+0747

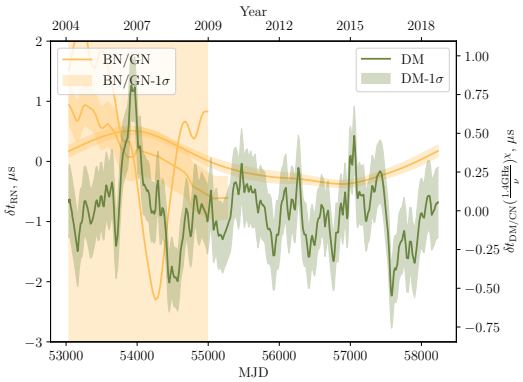

(k) J1730−2304

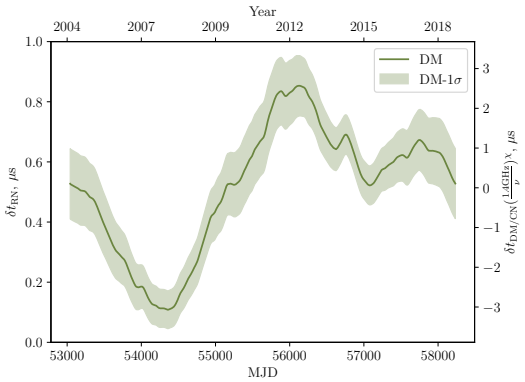

(l) J1732−5049

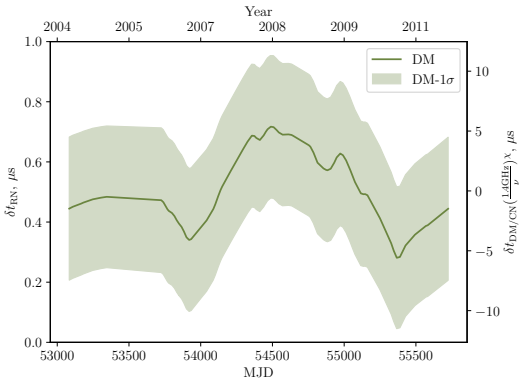

(m) J1744−1134

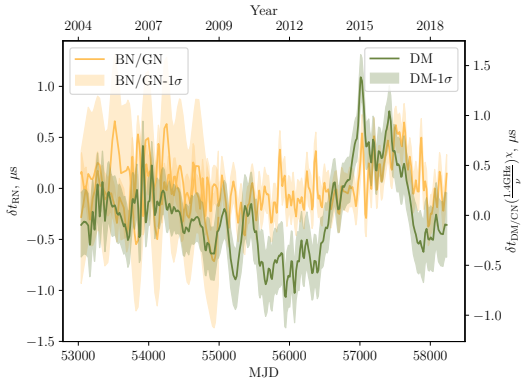

(n) J1824−2452A

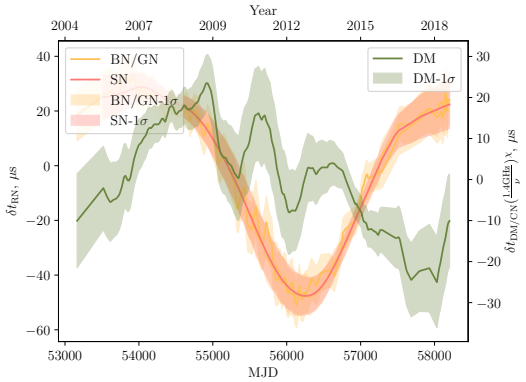

(o) J1832−0836

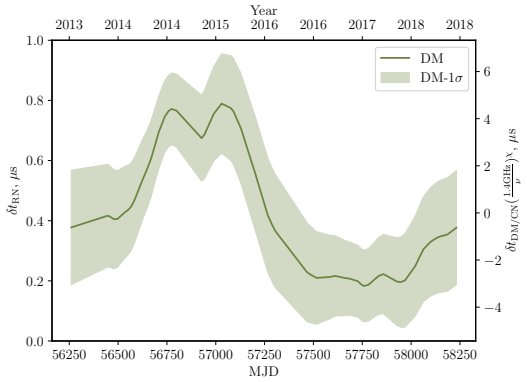

(p) J1857+0943

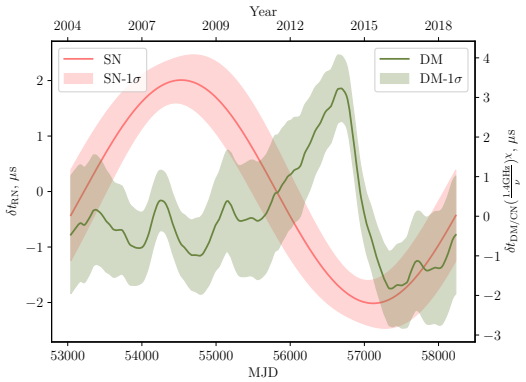

(q) J1909−3744

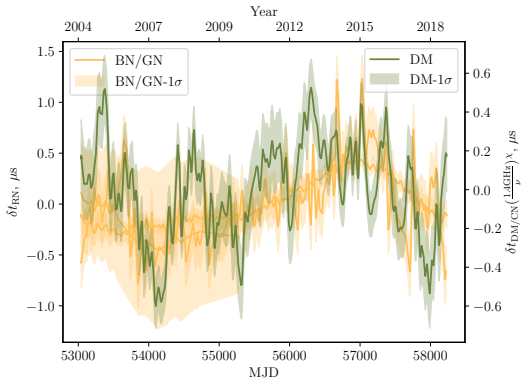

(r) J2124−3358

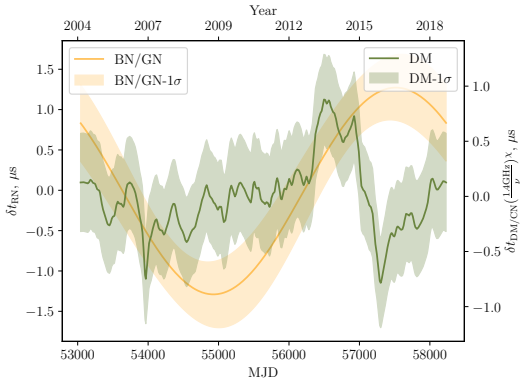

(s) J2129−5721

(t) J2145−0750

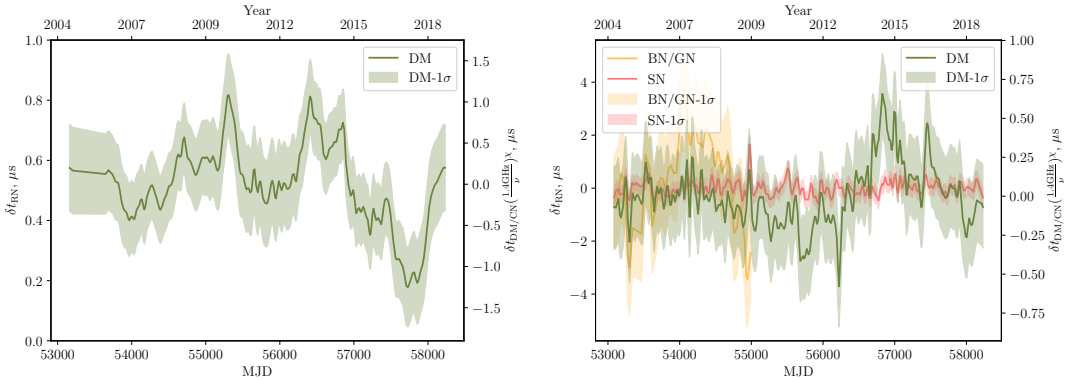

(u) J2241−5236

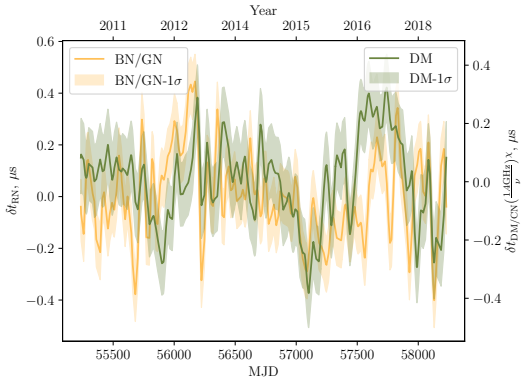

FIGURE A.2. Maximum-likelihood realizations of time-correlated stochastic noise in pulsars. SN is the spin noise, BN is the band noise, GN is the system noise (group noise), DM is the stochastic dispersion measure variations, and CN is the chromatic noise. Horizontal axes determine pulse arrival time in years (top) and MJD (bottom), vertical axes determine timing residuals in μs (left) with reference to 1400 MHz (right).

BIBLIOGRAPHY

J Aasi, BP Abbott, Robert Abbott, T Abbott, MR Abernathy, T Accadia, F Acernese, K Ackley, C Adams, Thomas Adams, et al.
Improved upper limits on the stochastic gravitational-wave background from 2009–2010 ligo and virgo data.
Physical Review Letters, 113(23):231101, 2014.

J Abadie, BP Abbott, R Abbott, M Abernathy, T Accadia, F Acernese, C Adams, R Adhikari, P Ajith, B Allen, et al.
Directional limits on persistent gravitational waves using ligo s5 science data.
Physical Review Letters, 107(27):271102, 2011.

J Abadie, BP Abbott, R Abbott, TD Abbott, M Abernathy, T Accadia, F Acernese, C Adams, R Adhikari, C Affeldt, et al.
Upper limits on a stochastic gravitational-wave background using ligo and virgo interferometers at 600–1000 hz.
Physical Review D, 85(12):122001, 2012.

B Abbott, R Abbott, R Adhikari, A Ageev, Bruce Allen, R Amin, SB Anderson, WG Anderson, M Araya, H Armandula, et al.
Analysis of first ligo science data for stochastic gravitational waves.
Physical Review D, 69(12):122004, 2004.

B Abbott, Robert Abbott, Rana Adhikari, J Agresti, P Ajith, B Allen, R Amin, SB Anderson, WG Anderson, M Araya, et al.
Searching for a stochastic background of gravitational waves with the laser interferometer gravitational-wave observatory.
The Astrophysical Journal, 659(2):918, 2007a.

B Abbott, Robert Abbott, Rana Adhikari, Juri Agresti, P Ajith, Bruce Allen, R Amin, SB Anderson, WG Anderson, M Arain, et al.
Upper limits on gravitational wave emission from 78 radio pulsars.
Physical Review D, 76(4):042001, 2007b.

B Abbott, Robert Abbott, Rana Adhikari, Juri Agresti, P Ajith, Bruce Allen, R Amin, SB Anderson, WG Anderson, M Arain, et al.
Upper limit map of a background of gravitational waves.
Physical Review D, 76(8):082003, 2007c.

B Abbott, Robert Abbott, Rana Adhikari, Juri Agresti, P Ajith, Bruce Allen, R Amin, SB Anderson, WG Anderson, M Arain, et al.
Upper limit map of a background of gravitational waves.
Physical Review D, 76(8):082003, 2007d.

Benjamin P Abbott, R Abbott, TD Abbott, MR Abernathy, F Acernese, K Ackley, C Adams, T Adams, P Addesso, RX Adhikari, et al.
Gw151226: observation of gravitational waves from a 22-solar-mass binary black hole coalescence.
Physical review letters, 116(24):241103, 2016a.

Benjamin P Abbott, Richard Abbott, TD Abbott, MR Abernathy, Fausto Acernese, Kendall Ackley, Carl Adams, Thomas Adams, Paolo Addesso, RX Adhikari, et al.
Observation of gravitational waves from a binary black hole merger.
Physical review letters, 116(6):061102, 2016b.

Benjamin P Abbott, R Abbott, TD Abbott, MR Abernathy, F Acernese, K Ackley, C Adams, T Adams, P Addesso, RX Adhikari, et al.
First search for gravitational waves from known pulsars with advanced ligo.
The Astrophysical Journal, 839(1):12, 2017a.

Benjamin P Abbott, R Abbott, TD Abbott, MR Abernathy, F Acernese, K Ackley, C Adams, T Adams, P Addesso, RX Adhikari, et al.
Directional limits on persistent gravitational waves from advanced ligo's first observing run.
Physical review letters, 118(12):121102, 2017b.

Benjamin P Abbott, R Abbott, TD Abbott, MR Abernathy, F Acernese, K Ackley, C Adams, T Adams, P Addesso, RX Adhikari, et al.
Upper limits on the stochastic gravitational-wave background from advanced ligo's first observing run.
Physical review letters, 118(12):121101, 2017c.

Benjamin P Abbott, R Abbott, TD Abbott, F Acernese, K Ackley, C Adams, T Adams, P Addesso, RX Adhikari, VB Adya, et al.
Gw170814: A three-detector observation of gravitational waves from a binary black hole coalescence.
Physical review letters, 119(14):141101, 2017d.

Benjamin P Abbott, R Abbott, TD Abbott, F Acernese, K Ackley, C Adams, T Adams, P Addesso, RX Adhikari, VB Adya, et al.
Gw170817: observation of gravitational waves from a binary neutron star inspiral.
Physical Review Letters, 119(16):161101, 2017e.

Benjamin P Abbott, Rich Abbott, TD Abbott, Fausto Acernese, Kendall Ackley, Carl Adams, Thomas Adams, Paolo Addesso, RX Adhikari, VB Adya, et al.
All-sky search for periodic gravitational waves in the o1 ligo data.
Physical Review D, 96(6):062002, 2017f.

BP Abbott, R Abbott, R Adhikari, P Ajith, B Allen, G Allen, RS Amin, SB Anderson, WG Anderson, MA Arain, et al.
Einstein@ home search for periodic gravitational waves in early s5 ligo data.
Physical review d, 80(4):042003, 2009.

BP Abbott, R Abbott, TD Abbott, F Acernese, K Ackley, C Adams, T Adams, P Addesso, RX Adhikari, VB Adya, et al.
Gw170608: Observation of a 19 solar-mass binary black hole coalescence.
The Astrophysical Journal Letters, 851(2):L35, 2017g.

BP Abbott, R Abbott, TD Abbott, F Acernese, K Ackley, C Adams, T Adams, P Addesso, RX Adhikari, et al.
Gw170104: observation of a 50-solar-mass binary black hole coalescence at redshift 0.2.
Physical Review Letters, 118(22):221101, 2017h.

BP Abbott, R Abbott, TD Abbott, S Abraham, F Acernese, K Ackley, C Adams, RX Adhikari, VB Adya, C Affeldt, et al.
Directional limits on persistent gravitational waves using data from advanced ligo's first two observing runs.
Physical Review D, 100(6):062001, 2019.

F Acernese, M Agathos, K Agatsuma, D Aisa, N Allemandou, A Allocca, J Amarni, P Astone, G Balestri, G Ballardin, et al.
Advanced virgo: a second-generation interferometric gravitational wave detector.
Classical and Quantum Gravity, 32(2):024001, 2014.

Anirban Ain, Prathamesh Dalvi, and Sanjit Mitra.
Fast gravitational wave radiometry using data folding.
Physical Review D, 92(2):022003, 2015.

Anirban Ain, Jishnu Suresh, and Sanjit Mitra.
Very fast stochastic gravitational wave background map making using folded data.
Physical Review D, 98(2):024001, 2018.

M Ali Alpar and David Pines.
Gravitational radiation from a solid-crust neutron star.
Nature, 314(6009):334–336, 1985.

M Ali Alpar, Radha Nandkumar, and David Pines.
Vortex creep and the internal temperature of neutron stars timing noise in pulsars.
The Astrophysical Journal, 311:197–213, 1986.

MA Alpar, PW Anderson, D Pines, and J Shaham.
Giant glitches and pinned vorticity in the vela and other pulsars.
The Astrophysical Journal, 249:L29–L33, 1981.

Pau Amaro-Seoane, Sofiane Aoudia, Stanislav Babak, Pierre Binetruy, Emanuele Berti, Alejandro Bohé, Chiara Caprini, Monica Colpi, Neil J Cornish, Karsten Danzmann, et al.
elisa: Astrophysics and cosmology in the millihertz regime.
arXiv preprint arXiv:1201.3621, 2012.

PW Anderson and N Itoh.
Pulsar glitches and restlessness as a hard superfluidity phenomenon.
Nature, 256(5512):25–27, 1975.

Theodore W Anderson and Donald A Darling.
Asymptotic theory of certain" goodness of fit" criteria based on stochastic processes.
The annals of mathematical statistics, pages 193–212, 1952.

Wilhelm Anderson.
Über die grenzdichte der materie und der energie.
Zeitschrift für Physik, 56(11-12):851–856, 1929.

Nils Andersson and Kostas D Kokkotas.
The r-mode instability in rotating neutron stars.
International Journal of Modern Physics D, 10(04):381–441, 2001.

F Antonucci, P Astone, S D'Antonio, S Frasca, and C Palomba.
Detection of periodic gravitational wave sources by hough transform in the f versus plane.
Classical and Quantum Gravity, 25(18):184015, 2008.

Zaven Arzoumanian, Adam Brazier, Sarah Burke-Spolaor, Sydney Chamberlin, Shami Chatterjee, Brian Christy, James M Cordes, Neil Cornish, Kathryn Crowter, Paul B Demorest, et al.
The nanograv nine-year data set: observations, arrival time measurements, and analysis of 37 millisecond pulsars.
The Astrophysical Journal, 813(1):65, 2015a.

Zaven Arzoumanian, Adam Brazier, Sarah Burke-Spolaor, Sydney Chamberlin, Shami Chatterjee, Brian Christy, James M Cordes, Neil Cornish, Kathryn Crowter, Paul B Demorest, et al.
The nanograv nine-year data set: observations, arrival time measurements, and analysis of 37 millisecond pulsars.
The Astrophysical Journal, 813(1):65, 2015b.

Zaven Arzoumanian, PT Baker, Adam Brazier, Sarah Burke-Spolaor, SJ Chamberlin, Shami Chatterjee, Brian Christy, James M Cordes, Neil J Cornish, Fronefield Crawford, et al.
The nanograv 11 year data set: pulsar-timing constraints on the stochastic gravitational-wave background.
The Astrophysical Journal, 859(1):47, 2018a.

Zaven Arzoumanian, Adam Brazier, Sarah Burke-Spolaor, Sydney Chamberlin, Shami Chatterjee, Brian Christy, James M Cordes, Neil J Cornish, Fronefield Crawford, H Thankful Cromartie, et al.
The nanograv 11-year data set: high-precision timing of 45 millisecond pulsars.
The Astrophysical Journal Supplement Series, 235(2):37, 2018b.

Gregory Ashton, Reinhard Prix, and David Ian Jones.
Statistical characterization of pulsar glitches and their potential impact on searches for continuous gravitational waves.
Physical Review D, 96(6):063004, 2017.

Gregory Ashton, Moritz Hübner, Paul D Lasky, Colm Talbot, Kendall Ackley, Sylvia Biscoveanu, Qi Chu, Atul Divakarla, Paul J Easter, Boris Goncharov, et al.
Bilby: A user-friendly bayesian inference library for gravitational-wave astronomy.
The Astrophysical Journal Supplement Series, 241(2):27, 2019a.

Gregory Ashton, Paul D Lasky, Vanessa Graber, and Jim Palfreyman.
Rotational evolution of the vela pulsar during the 2016 glitch.
Nature Astronomy, 3(12):1143–1148, 2019b.

Pia Astone, Sabrina D'Antonio, Sergio Frasca, and Cristiano Palomba.
A method for detection of known sources of continuous gravitational wave signals in non-stationary data.
Classical and Quantum Gravity, 27(19):194016, 2010.

Walter Baade and Fritz Zwicky.
Remarks on super-novae and cosmic rays.
Physical Review, 46(1):76, 1934.

D C Backer, Shrinivas R Kulkarni, Carl Heiles, MM Davis, and WM Goss.

A millisecond pulsar.
Nature, 300(5893):615, 1982.

DC Backer.
Pulsar nulling phenomena.
Nature, 228(5266):42–43, 1970.

Stefan W Ballmer.
A radiometer for stochastic gravitational waves.
Classical and Quantum Gravity, 23(8):S179, 2006.

CG Bassa, GH Janssen, BW Stappers, TM Tauris, T Wevers, PG Jonker, L Lentati, JPW Verbiest, G Desvignes, E Graikou, et al.
A millisecond pulsar in an extremely wide binary system.
Monthly Notices of the Royal Astronomical Society, 460(2):2207–2222, 2016.

Werner Becker et al.
Neutron stars and pulsars.
2009.

Lars Bildsten.
Gravitational radiation and rotation of accreting neutron stars.
The Astrophysical Journal Letters, 501(1):L89, 1998.

GS Bisnovatyi-Kogan and BV Komberg.
Pulsars and close binary systems.
Soviet Astronomy, 18:217, 1974.

Patrick R Brady, Teviet Creighton, Curt Cutler, and Bernard F Schutz.
Searching for periodic sources with ligo.
Physical Review D, 57(4):2101, 1998.

Ashley Bransgrove, Yuri Levin, and Andrei Beloborodov.
Magnetic field evolution of neutron stars–i. basic formalism, numerical techniques and first results.
Monthly Notices of the Royal Astronomical Society, 473(2):2771–2790, 2018.

Trevor S Breusch and Adrian R Pagan.
A simple test for heteroscedasticity and random coefficient variation.
Econometrica: Journal of the Econometric Society, pages 1287–1294, 1979.

Richard Brito, Shrobana Ghosh, Enrico Barausse, Emanuele Berti, Vitor Cardoso, Irina Dvorkin, Antoine Klein, and Paolo Pani.

Gravitational wave searches for ultralight bosons with ligo and lisa.
Physical Review D, 96(6):064050, 2017.

PR Brook, A Karastergiou, MA McLaughlin, MT Lam, Z Arzoumanian, S Chatterjee, JM Cordes, K Crowter, M DeCesar, PB Demorest, et al.
The nanograv 11-year data set: Pulse profile variability.
The Astrophysical Journal, 868(2):122, 2018.

RN Caballero, KJ Lee, L Lentati, Grégory Desvignes, DJ Champion, JPW Verbiest, GH Janssen, BW Stappers, M Kramer, P Lazarus, et al.
The noise properties of 42 millisecond pulsars from the european pulsar timing array and their impact on gravitational-wave searches.
Monthly Notices of the Royal Astronomical Society, 457(4):4421–4440, 2016.

RN Caballero, YJ Guo, KJ Lee, P Lazarus, DJ Champion, G Desvignes, M Kramer, K Plant, Z Arzoumanian, M Bailes, et al.
Studying the solar system with the international pulsar timing array.
Monthly Notices of the Royal Astronomical Society, 481(4):5501–5516, 2018.

Max Camenzind.
Compact objects in astrophysics.
Springer, 2007.

AG Cameron.
Neutron star models.
The Astrophysical Journal, 130:884, 1959.

Alastair GW Cameron.
Neutron stars.
Annual Review of Astronomy and Astrophysics, 8(1):179–208, 1970.

Bradley P Carlin and Siddhartha Chib.
Bayesian model choice via markov chain monte carlo methods.
Journal of the Royal Statistical Society: Series B (Methodological), 57(3):473–484, 1995.

James Chadwick.
Possible existence of a neutron.
Nature, 129(3252):312–312, 1932.

Deepto Chakrabarty, Edward H Morgan, Michael P Muno, Duncan K Galloway, Rudy Wijnands, Michiel van der Klis, and Craig B Markwardt.
Nuclear-powered millisecond pulsars and the maximum spin frequency of neutron stars.
Nature, 424(6944):42–44, 2003.

DJ Champion, GB Hobbs, RN Manchester, RT Edwards, DC Backer, M Bailes, NDR Bhat, S Burke-Spolaor, W Coles, PB Demorest, et al.
Measuring the mass of solar system planets using pulsar timing.
The Astrophysical Journal Letters, 720(2):L201, 2010.

Subrahmanyan Chandrasekhar.
The maximum mass of ideal white dwarfs.
The Astrophysical Journal, 74:81, 1931.

W Coles, G Hobbs, DJ Champion, RN Manchester, and JPW Verbiest.
Pulsar timing analysis in the presence of correlated noise.
Monthly Notices of the Royal Astronomical Society, 418(1):561–570, 2011.

WA Coles, M Kerr, RM Shannon, GB Hobbs, RN Manchester, X-P You, M Bailes, NDR Bhat, S Burke-Spolaor, S Dai, et al.
Pulsar observations of extreme scattering events.
The Astrophysical Journal, 808(2):113, 2015.

William A Coles, Barney J Rickett, JJ Gao, George Hobbs, and JPW Verbiest.
Scattering of pulsar radio emission by the interstellar plasma.
The Astrophysical Journal, 717(2):1206, 2010.

James M Cordes.
The detectability of planetary companions to radio pulsars.
In *Planets around pulsars*, volume 36, pages 43–60, 1993.

James M Cordes, Ryan M Shannon, and Daniel R Stinebring.
Frequency-dependent dispersion measures and implications for pulsar timing.
The Astrophysical Journal, 817(1):16, 2016.

JM Cordes and GS Downs.
Jpl pulsar timing observations. iii-pulsar rotation fluctuations.
The Astrophysical Journal Supplement Series, 59:343–382, 1985.

JM Cordes and RM Shannon.
A measurement model for precision pulsar timing.
arXiv preprint arXiv:1010.3785, 2010.

S Dai, G Hobbs, Richard Norman Manchester, M Kerr, Ryan M Shannon, Willem van Straten, A Mata, M Bailes, NDR Bhat, Sarah Burke-Spolaor, et al.
A study of multifrequency polarization pulse profiles of millisecond pulsars.
Monthly Notices of the Royal Astronomical Society, 449(3):3223–3262, 2015.

F D'Alessandro, PM McCulloch, PA Hamilton, and AA Deshpande.
The timing noise of 45 southern pulsars.
Monthly Notices of the Royal Astronomical Society, 277(3):1033–1046, 1995.

Paul B Demorest, Robert D Ferdman, ME Gonzalez, D Nice, S Ransom, IH Stairs, Z Arzoumanian, A Brazier, S Burke-Spolaor, SJ Chamberlin, et al.
Limits on the stochastic gravitational wave background from the north american nanohertz observatory for gravitational waves.
The Astrophysical Journal, 762(2):94, 2012.

Vladimir Dergachev.
On blind searches for noise dominated signals: a loosely coherent approach.
Classical and Quantum Gravity, 27(20):205017, 2010.

G Desvignes, RN Caballero, L Lentati, JPW Verbiest, DJ Champion, BW Stappers, GH Janssen, P Lazarus, S Osłowski, S Babak, et al.
High-precision timing of 42 millisecond pulsars with the european pulsar timing array.
Monthly Notices of the Royal Astronomical Society, 458(3):3341–3380, 2016.

Steven Detweiler.
Pulsar timing measurements and the search for gravitational waves.
The Astrophysical Journal, 234:1100–1104, 1979.

Sanjeev Dhurandhar, Badri Krishnan, Himan Mukhopadhyay, and John T Whelan.
Cross-correlation search for periodic gravitational waves.
Physical Review D, 77(8):082001, 2008.

Sanjeev V Dhurandhar and Alberto Vecchio.
Searching for continuous gravitational wave sources in binary systems.
Physical Review D, 63(12):122001, 2001.

RG Dodson, PM McCulloch, and DR Lewis.
High time resolution observations of the january 2000 glitch in the vela pulsar.
The Astrophysical Journal Letters, 564(2):L85, 2001.

Robert C Duncan and Christopher Thompson.
Formation of very strongly magnetized neutron stars-implications for gamma-ray bursts.
The Astrophysical Journal, 392:L9–L13, 1992.

Réjean J Dupuis and Graham Woan.
Bayesian estimation of pulsar parameters from gravitational wave data.
Physical Review D, 72(10):102002, 2005.

William E East and Frans Pretorius.
Superradiant instability and backreaction of massive vector fields around kerr black holes.
Physical review letters, 119(4):041101, 2017.

Russell T Edwards, GB Hobbs, and RN Manchester.
Tempo2, a new pulsar timing package–ii. the timing model and precision estimates.
Monthly Notices of the Royal Astronomical Society, 372(4):1549–1574, 2006.

Justin Ellis and Rutger van Haasteren.
jellis18/ptmcmcsampler: Official release, October 2017.

Justin A. Ellis, Michele Vallisneri, Stephen R. Taylor, and Paul T. Baker.
ENTERPRISE: Enhanced Numerical Toolbox Enabling a Robust PulsaR Inference SuitE, Dec 2019.

Cristobal M Espinoza, Andrew G Lyne, Ben W Stappers, and Michael Kramer.
A study of 315 glitches in the rotation of 102 pulsars.
Monthly Notices of the Royal Astronomical Society, 414(2):1679–1704, 2011.

Roger Sherman Foster and DC Backer.
Constructing a pulsar timing array.
The Astrophysical Journal, 361:300–308, 1990a.

Roger Sherman Foster and DC Backer.
Constructing a pulsar timing array.
The Astrophysical Journal, 361:300–308, 1990b.

Duncan K Galloway, Sammanani Premachandra, Danny Steeghs, Tom Marsh, Jorge Casares, and Rémon Cornelisse.
Precision ephemerides for gravitational-wave searches. i. sco x-1.
The Astrophysical Journal, 781(1):14, 2013.

P Ghosh and FK Lamb.
Accretion by rotating magnetic neutron stars. iii-accretion torques and period changes in pulsating x-ray sources.
The Astrophysical Journal, 234:296–316, 1979.

Riccardo Giacconi, Herbert Gursky, Frank R Paolini, and Bruno B Rossi.
Evidence for x rays from sources outside the solar system.
Physical Review Letters, 9(11):439, 1962.

K Glampedakis, DI Jones, and Lars Samuelsson.
Gravitational waves from color-magnetic “mountains” in neutron stars.
Physical review letters, 109(8):081103, 2012.

E Goetz and K Riles.
An all-sky search algorithm for continuous gravitational waves from spinning neutron stars in binary systems.
Classical and quantum gravity, 28(21):215006, 2011.

T Gold.
Rotating neutron stars as the origin of the pulsating radio sources.
Nature, 218(5143):731–732, 1968.

Boris Goncharov, Xing-Jiang Zhu, and Eric Thrane.
Is there a spectral turnover in spin noise of millisecond pulsars?
arXiv preprint arXiv:1910.05961, 2019.

YJ Guo, GY Li, KJ Lee, and RN Caballero.
Studying the solar system dynamics using pulsar timing arrays and the linimoss dynamical model.
Monthly Notices of the Royal Astronomical Society, 489(4):5573–5581, 2019.

P Haensel, JP Lasota, and JL Zdunik.
On the minimum period of uniformly rotating neutron stars.
Astronomy and Astrophysics, 344:151–153, 1999.

William W Hager.
Updating the inverse of a matrix.
SIAM review, 31(2):221–239, 1989.

WJ Handley, MP Hobson, and AN Lasenby.
Polychord: nested sampling for cosmology.
Monthly Notices of the Royal Astronomical Society: Letters, 450(1):L61–L65, 2015a.

WJ Handley, MP Hobson, and AN Lasenby.
Polychord: next-generation nested sampling.
Monthly Notices of the Royal Astronomical Society, 453(4):4384–4398, 2015b.

Gregory M Harry, LIGO Scientific Collaboration, et al.
Advanced ligo: the next generation of gravitational wave detectors.
Classical and Quantum Gravity, 27(8):084006, 2010.

Brynmor Haskell, Lars Samuelsson, Kostas Glampedakis, and Nils Andersson.
Modelling magnetically deformed neutron stars.
Monthly Notices of the Royal Astronomical Society, 385(1):531–542, 2008.

Stephen W Hawking and Werner Israel.

Three hundred years of gravitation.
Cambridge University Press, 1989.

JS Hazboun, J Simon, SR Taylor, MT Lam, SJ Vigeland, K Islo, JS Key, Z Arzoumanian, PT Baker, A Brazier, et al.
The nanograv 11 yr data set: Evolution of gravitational-wave background statistics.
The Astrophysical Journal, 890(2):108, 2020.

Sonke Hee, WJ Handley, Mike P Hobson, and Anthony N Lasenby.
Bayesian model selection without evidences: application to the dark energy equation-of-state.
Monthly Notices of the Royal Astronomical Society, 455(3):2461–2473, 2015.

RW Hellings and GS Downs.
Upper limits on the isotropic gravitational radiation background from pulsar timing analysis.
The Astrophysical Journal, 265:L39–L42, 1983.

Jason WT Hessels, Scott M Ransom, Ingrid H Stairs, Paulo CC Freire, Victoria M Kaspi, and Fernando Camilo.
A radio pulsar spinning at 716 hz.
Science, 311(5769):1901–1904, 2006.

Antony Hewish, S Jocelyn Bell, John DH Pilkington, Paul Frederick Scott, and Robin Ashley Collins.
Observation of a rapidly pulsating radio source.
Nature, 217(5130):709–713, 1968.

S. R. Hinton.
ChainConsumer.
The Journal of Open Source Software, 1:00045, August 2016.
doi: 10.21105/joss.00045.

G Hobbs, A Archibald, Zaven Arzoumanian, D Backer, M Bailes, NDR Bhat, M Burgay, Sarah Burke-Spolaor, D Champion, I Cognard, et al.
The international pulsar timing array project: using pulsars as a gravitational wave detector.
Classical and Quantum Gravity, 27(8):084013, 2010a.

G Hobbs, AG Lyne, and M Kramer.
An analysis of the timing irregularities for 366 pulsars.
Monthly Notices of the Royal Astronomical Society, 402(2):1027–1048, 2010b.

G Hobbs, L Guo, RN Caballero, W Coles, KJ Lee, RN Manchester, DJ Reardon, D Matsakis, ML Tong, Z Arzoumanian, et al.
A pulsar-based time-scale from the international pulsar timing array.

Monthly Notices of the Royal Astronomical Society, 491(4):5951–5965, 2020a.

GB Hobbs, RT Edwards, and RN Manchester.
Tempo2, a new pulsar-timing package–i. an overview.
Monthly Notices of the Royal Astronomical Society, 369(2):655–672, 2006.

George Hobbs, William Coles, RN Manchester, MJ Keith, Ryan M Shannon, D Chen, M Bailes, NDR Bhat, Sarah Burke-Spolaor, D Champion, et al.
Development of a pulsar-based time-scale.
Monthly Notices of the Royal Astronomical Society, 427(4):2780–2787, 2012.

George Hobbs, Richard N Manchester, Alex Dunning, Andrew Jameson, Paul Roberts, Daniel George, JA Green, John Tuthill, Lawrence Toomey, Jane F Kaczmarek, et al.
An ultra-wide bandwidth (704 to 4 032 mhz) receiver for the parkes radio telescope.
Publications of the Astronomical Society of Australia, 37, 2020b.

PV Hough.
Proceedings of the international conference on high energy accelerators and instrumentation.
1959.

Russell A Hulse and Joseph H Taylor.
Discovery of a pulsar in a binary system.
The Astrophysical Journal, 195:L51–L53, 1975.

Piotr Jaranowski.
P. jaranowski, a. królak, and bf schutz, phys. rev. d 58, 063001 (1998).
Phys. Rev. D, 58:063001, 1998.

Henrik Jeldtoft Jensen.
Self-organized criticality: emergent complex behavior in physical and biological systems, volume 10.
Cambridge university press, 1998.

Simon Johnston and David Galloway.
Pulsar braking indices revisited.
Monthly Notices of the Royal Astronomical Society, 306(4):L50–L54, 1999a.

Simon Johnston and David Galloway.
Pulsar braking indices revisited.
Monthly Notices of the Royal Astronomical Society, 306(4):L50–L54, 1999b.

DI Jones.
Gravitational wave emission from rotating superfluid neutron stars.
Monthly Notices of the Royal Astronomical Society, 402(4):2503–2519, 2010.

Megan L Jones, Maura A McLaughlin, Michael T Lam, James M Cordes, Lina Levin, Shami Chatterjee, Zaven Arzoumanian, Kathryn Crowter, Paul B Demorest, Timothy Dolch, et al.
The nanograv nine-year data set: measurement and analysis of variations in dispersion measures.
The Astrophysical Journal, 841(2):125, 2017.

PB Jones.
The generation of timing noise by superfluid rotation in pulsars.
Monthly Notices of the Royal Astronomical Society, 246:364, 1990.

David L Kaplan, Thomas Kupfer, David J Nice, Andreas Irrgang, Ulrich Heber, Zaven Arzoumanian, Elif Beklen, Kathryn Crowter, Megan E DeCesar, Paul B Demorest, et al.
Psr j1024–0719: a millisecond pulsar in an unusual long-period orbit.
The Astrophysical Journal, 826(1):86, 2016.

Robert E Kass and Adrian E Raftery.
Bayes factors.
Journal of the american statistical association, 90(430):773–795, 1995.

MJ Keith, W Coles, RM Shannon, GB Hobbs, RN Manchester, M Bailes, NDR Bhat, S Burke-Spolaor, DJ Champion, A Chaudhary, et al.
Measurement and correction of variations in interstellar dispersion in high-precision pulsar timing.
Monthly Notices of the Royal Astronomical Society, 429(3):2161–2174, 2013.

M. Kerr, D. J. Reardon, G. Hobbs, R. M. Shannon, R. N. Manchester, S Dai, CJ Russell, S-B Zhang, W van Straten, S Osłowski, et al.
The parkes pulsar timing array project: Second data release.
arXiv preprint arXiv:2003.09780, 2020.

D Klochkov, G Pühlhofer, V Suleimanov, S Simon, K Werner, and A Santangelo.
A non-pulsating neutron star in the supernova remnant hess j1731- 347/g353. 6- 0.7 with a carbon atmosphere.
Astronomy & Astrophysics, 556:A41, 2013.

Michael Kramer and David J Champion.
The european pulsar timing array and the large european array for pulsars.
Classical and Quantum Gravity, 30(22):224009, 2013.

Michael Kramer, Kiriaki M Xilouris, Fernando Camilo, David J Nice, Donald C Backer, Christoph Lange, Duncan R Lorimer, Oleg Doroshenko, and Shauna Sallmen.
Profile instabilities of the millisecond pulsar psr j1022+1001.
The Astrophysical Journal, 520(1):324, 1999.

Badri Krishnan, Alicia M Sintes, Maria Alessandra Papa, Bernard F Schutz, Sergio Frasca, and Cristiano Palomba.
Hough transform search for continuous gravitational waves.
Physical Review D, 70(8):082001, 2004.

V Venkatraman Krishnan, M Bailes, W Van Straten, N Wex, PCC Freire, EF Keane, TM Tauris, PA Rosado, NDR Bhat, C Flynn, et al.
Lense–thirring frame dragging induced by a fast-rotating white dwarf in a binary pulsar system.
Science, 367(6477):577–580, 2020.

MT Lam, JM Cordes, S Chatterjee, Z Arzoumanian, K Crowter, PB Demorest, T Dolch, JA Ellis, RD Ferdman, EF Fonseca, et al.
The nanograv nine-year data set: Noise budget for pulsar arrival times on intraday timescales.
The Astrophysical Journal, 819(2):155, 2016.

MT Lam, JA Ellis, G Grillo, ML Jones, JS Hazboun, PR Brook, JE Turner, S Chatterjee, JM Cordes, TJW Lazio, et al.
A second chromatic timing event of interstellar origin toward psr j1713+ 0747.
The Astrophysical Journal, 861(2):132, 2018.

Lev Davidovich Landau.
On the theory of stars.
Phys. Z. Sowjetunion, 1(285):152, 1932.

Paul D Lasky.
Gravitational waves from neutron stars: a review.
Publications of the Astronomical Society of Australia, 32, 2015.

Paul D Lasky, Andrew Melatos, Vikram Ravi, and George Hobbs.
Pulsar timing noise and the minimum observation time to detect gravitational waves with pulsar timing arrays.
Monthly Notices of the Royal Astronomical Society, 449(3):3293–3300, 2015.

L Lentati, M Kerr, S Dai, MP Hobson, Ryan M Shannon, G Hobbs, M Bailes, ND Ramesh Bhat, Sarah Burke-Spolaor, W Coles, et al.
Wide-band profile domain pulsar timing analysis.
Monthly Notices of the Royal Astronomical Society, 466(3):3706–3727, 2017.

Lindley Lentati, Paul Alexander, Michael P Hobson, Stephen Taylor, Jonathon Gair, Sreekumar T Balan, and Rutger van Haasteren.
Hyper-efficient model-independent bayesian method for the analysis of pulsar timing data.
Physical Review D, 87(10):104021, 2013.

Lindley Lentati, Paul Alexander, Michael P Hobson, Farhan Feroz, Rutger van Haasteren, KJ Lee, and Ryan M Shannon.
Temponest: a bayesian approach to pulsar timing analysis.
Monthly Notices of the Royal Astronomical Society, 437(3):3004–3023, 2014.

Lindley Lentati, Ryan M Shannon, William A Coles, Joris PW Verbiest, Rutger van Haasteren, JA Ellis, RN Caballero, Richard Norman Manchester, Z Arzoumanian, Stanislav Babak, et al.
From spin noise to systematics: stochastic processes in the first international pulsar timing array data release.
Monthly Notices of the Royal Astronomical Society, 458(2):2161–2187, 2016.

Lina Levin, Maura A McLaughlin, Glenn Jones, James M Cordes, Daniel R Stinebring, Shami Chatterjee, Timothy Dolch, Michael T Lam, T Joseph W Lazio, Nipuni Palliyaguru, et al.
The nanograv nine-year data set: Monitoring interstellar scattering delays.
The Astrophysical Journal, 818(2):166, 2016.

Greta M Ljung and George EP Box.
On a measure of lack of fit in time series models.
Biometrika, 65(2):297–303, 1978.

Duncan Ross Lorimer and Michael Kramer.
Handbook of pulsar astronomy.
Handbook of pulsar astronomy, by DR Lorimer and M. Kramer. Cambridge observing handbooks for research astronomers, Vol. 4. Cambridge, UK: Cambridge University Press, 2004, 4, 2004.

Andrew Lyne and Francis Graham-Smith.
Pulsar astronomy.
Number 48. Cambridge University Press, 2012.

Andrew Lyne, George Hobbs, Michael Kramer, Ingrid Stairs, and Ben Stappers.
Switched magnetospheric regulation of pulsar spin-down.
Science, 329(5990):408–412, 2010.

David JC MacKay.
Information theory, inference and learning algorithms.
Cambridge university press, 2003.

DR Madison, JM Cordes, Z Arzoumanian, S Chatterjee, K Crowter, ME DeCesar, PB Demorest, T Dolch, JA Ellis, RD Ferdman, et al.
The nanograv 11 yr data set: Solar wind sounding through pulsar timing.
The Astrophysical Journal, 872(2):150, 2019.

R N Manchester, G B Hobbs, A Teoh, and M Hobbs.
The australia telescope national facility pulsar catalogue.
The Astronomical Journal, 129(4):1993, 2005.
URL http://www.atnf.csiro.au/research/pulsar/psrcat/.

RN Manchester, G Hobbs, M Bailes, WA Coles, W van Straten, MJ Keith, RM Shannon, NDR Bhat, A Brown, SG Burke-Spolaor, et al.
The parkes pulsar timing array project.
Publications of the Astronomical Society of Australia, 30, 2013.

PM McCulloch, PA Hamilton, GWR Royle, and RN Manchester.
Daily observations of a large period jump of the vela pulsar.
Nature, 302(5906):319–321, 1983.

Maura A McLaughlin.
The north american nanohertz observatory for gravitational waves.
Classical and Quantum Gravity, 30(22):224008, 2013a.

Maura A McLaughlin.
The north american nanohertz observatory for gravitational waves.
Classical and Quantum Gravity, 30(22):224008, 2013b.

A Melatos and DJB Payne.
Gravitational radiation from an accreting millisecond pulsar with a magnetically confined mountain.
The Astrophysical Journal, 623(2):1044, 2005a.

A Melatos, Carlos Peralta, and JSB Wyithe.
Avalanche dynamics of radio pulsar glitches.
The Astrophysical Journal, 672(2):1103, 2008.

Andrew Melatos and Bennett Link.
Pulsar timing noise from superfluid turbulence.
Monthly Notices of the Royal Astronomical Society, 437(1):21–31, 2013.

Andrew Melatos and DJB Payne.
Gravitational radiation from an accreting millisecond pulsar with a magnetically confined mountain.
The Astrophysical Journal, 623(2):1044, 2005b.

C Messenger.
Understanding the sensitivity of the stochastic radiometer analysis in terms of the strain tensor amplitude.

LIGO Document T1000195-v1, 2010.

C Messenger, HJ Bulten, SG Crowder, V Dergachev, DK Galloway, E Goetz, RJG Jonker, PD Lasky, GD Meadors, A Melatos, et al.
Gravitational waves from scorpius x-1: A comparison of search methods and prospects for detection with advanced detectors.
Physical Review D, 92(2):023006, 2015.

J Robert Oppenheimer and George M Volkoff.
On massive neutron cores.
Physical Review, 55(4):374, 1939.

S Osłowski, Willem van Straten, GB Hobbs, Matthew Bailes, and Paul Demorest.
High signal-to-noise ratio observations and the ultimate limits of precision pulsar timing.
Monthly Notices of the Royal Astronomical Society, 418(2):1258–1271, 2011a.

S Osłowski, Willem van Straten, GB Hobbs, Matthew Bailes, and Paul Demorest.
High signal-to-noise ratio observations and the ultimate limits of precision pulsar timing.
Monthly Notices of the Royal Astronomical Society, 418(2):1258–1271, 2011b.

F Pacini.
Energy emission from a neutron star.
Nature, 216(5115):567–568, 1967.

A Parthasarathy, RM Shannon, S Johnston, L Lentati, M Bailes, S Dai, M Kerr, RN Manchester, S Osłowski, C Sobey, et al.
Timing of young radio pulsars–i. timing noise, periodic modulation, and proper motion.
Monthly Notices of the Royal Astronomical Society, 489(3):3810–3826, 2019.

Alessandro Patruno and AL Watts.
Accreting millisecond x-ray pulsars.
arXiv preprint arXiv:1206.2727, 2012.

BBP Perera, ME DeCesar, PB Demorest, M Kerr, L Lentati, DJ Nice, S Oslowski, SM Ransom, MJ Keith, Z Arzoumanian, et al.
The international pulsar timing array: Second data release.
Monthly Notices of the Royal Astronomical Society, 490(4):4666–4687, 2019.

Philip C Peters and Jon Mathews.
Gravitational radiation from point masses in a keplerian orbit.
Physical Review, 131(1):435, 1963.

JA Phillips and Alexander Wolszczan.

Time variability of pulsar dispersion measures.
The Astrophysical Journal, 382:L27–L30, 1991.

M. Pitkin.
psrqpy: a python interface for querying the ATNF pulsar catalogue.
Journal of Open Source Software, 3(22):538, February 2018.
doi: 10.21105/joss.00538.
URL https://doi.org/10.21105/joss.00538.

Nataliya K Porayko, Xingjiang Zhu, Yuri Levin, Lam Hui, George Hobbs, Aleksandra Grudskaya, Konstantin Postnov, Matthew Bailes, ND Ramesh Bhat, William Coles, et al.
Parkes pulsar timing array constraints on ultralight scalar-field dark matter.
Physical Review D, 98(10):102002, 2018.

William H Press and Kip S Thorne.
Gravitational-wave astronomy.
Annual Review of Astronomy and Astrophysics, 10(1):335–374, 1972.

Mohan Rajagopal and Roger W Romani.
Ultra-low frequency gravitational radiation from massive black hole binaries.
arXiv preprint astro-ph/9412038, 1994.

Rajagopalan Ramachandran, P Demorest, DC Backer, I Cognard, and A Lommen.
Interstellar plasma weather effects in long-term multifrequency timing of pulsar b1937+ 21.
The Astrophysical Journal, 645(1):303, 2006.

D. J. Reardon, G. Hobbs, W. A. Coles, Y. Levin, M. J. Keith, M Bailes, NDR Bhat, S Burke-Spolaor, S Dai, M Kerr, et al.
Timing analysis for 20 millisecond pulsars in the parkes pulsar timing array.
Monthly Notices of the Royal Astronomical Society, 455(2):1751–1769, 2016.

Andreas Reisenegger and Axel Bonačić.
Millisecond pulsars with r-modes as steady gravitational radiators.
Physical review letters, 91(20):201103, 2003.

BJ Rickett.
Radio propagation through the turbulent interstellar plasma.
Annual review of astronomy and astrophysics, 28(1):561–605, 1990.

Keith Riles.
Recent searches for continuous gravitational waves.
Modern Physics Letters A, 32(39):1730035, 2017.

RT Ritchings.
Pulsar single pulse intensity measurements and pulse nulling.
Monthly Notices of the Royal Astronomical Society, 176(2):249–263, 1976.

R. W. Romani.
Timing a millisecond pulsar array.
In H. Ögelman and E. P. J. van den Heuvel, editors, *NATO Advanced Science Institutes (ASI) Series C*, volume 262 of *NATO Advanced Science Institutes (ASI) Series C*, page 113, 1989.

Roger W Romani, Ramesh Narayan, and Roger Blandford.
Refractive effects in pulsar scintillation.
Monthly Notices of the Royal Astronomical Society, 220(1):19–49, 1986.

Pablo A Rosado, Alberto Sesana, and Jonathan Gair.
Expected properties of the first gravitational wave signal detected with pulsar timing arrays.
Monthly Notices of the Royal Astronomical Society, 451(3):2417–2433, 2015.

Malvin Ruderman, Tianhua Zhu, and Kaiyou Chen.
Neutron star magnetic field evolution, crust movement, and glitches.
The Astrophysical Journal, 492(1):267, 1998.

MV Sazhin.
Opportunities for detecting ultralong gravitational waves.
Sov. Astron, 22:36–38, 1978.

RM Shannon and JM Cordes.
Modelling and mitigating refractive propagation effects in precision pulsar timing observations.
Monthly Notices of the Royal Astronomical Society, 464(2):2075–2089, 2017.

RM Shannon, JM Cordes, TS Metcalfe, TJW Lazio, Ismaël Cognard, G Desvignes, GH Janssen, A Jessner, M Kramer, K Lazaridis, et al.
An asteroid belt interpretation for the timing variations of the millisecond pulsar b1937+ 21.
The Astrophysical Journal, 766(1):5, 2013.

Ryan M Shannon and James M Cordes.
Assessing the role of spin noise in the precision timing of millisecond pulsars.
The Astrophysical Journal, 725(2):1607, 2010.

Ryan M Shannon, S Osłowski, S Dai, Matthew Bailes, G Hobbs, Richard Norman Manchester, Willem van Straten, Carolyn A Raithel, Vikram Ravi, L Toomey, et al.
Limitations in timing precision due to single-pulse shape variability in millisecond pulsars.
Monthly Notices of the Royal Astronomical Society, 443(2):1463–1481, 2014.

Ryan M Shannon, Vikram Ravi, LT Lentati, Paul Daniel Lasky, G Hobbs, Matthew Kerr, Richard Norman Manchester, William A Coles, Yuri Levin, Matthew Bailes, et al.
Gravitational waves from binary supermassive black holes missing in pulsar observations.
Science, 349(6255):1522–1525, 2015.

Ryan M Shannon, LT Lentati, Matthew Kerr, Matthew Bailes, NDR Bhat, William A Coles, Shi Dai, James Dempsey, G Hobbs, MJ Keith, et al.
The disturbance of a millisecond pulsar magnetosphere.
The Astrophysical Journal Letters, 828(1):L1, 2016.

IS Shklovsky.
On the nature of the source of x-ray emission of sco xr-1.
The Astrophysical Journal, 148:L1, 1967.

Magdalena Sieniawska and Michał Bejger.
Continuous gravitational waves from neutron stars: current status and prospects.
Universe, 5(11):217, 2019.

John Skilling.
Nested sampling.
In *AIP Conference Proceedings*, volume 735, pages 395–405. AIP, 2004.

John Skilling et al.
Nested sampling for general bayesian computation.
Bayesian analysis, 1(4):833–859, 2006.

Josh Speagle and Kyle Barbary.
dynesty: Dynamic nested sampling package.
Astrophysics Source Code Library, 2018.

Michael A Stephens.
Edf statistics for goodness of fit and some comparisons.
Journal of the American statistical Association, 69(347):730–737, 1974.

Edmund C Stoner.
Lxxxvii. the equilibrium of dense stars.
The London, Edinburgh, and Dublin Philosophical Magazine and Journal of Science, 9(60): 944–963, 1930.

S Suvorova, L Sun, A Melatos, W Moran, and RJ Evans.
Hidden markov model tracking of continuous gravitational waves from a neutron star with wandering spin.
Physical Review D, 93(12):123009, 2016.

Joseph H Taylor and Joel M Weisberg.
A new test of general relativity-gravitational radiation and the binary pulsar psr 1913+ 16.
The Astrophysical Journal, 253:908–920, 1982.

SR Taylor, Michele Vallisneri, JA Ellis, CMF Mingarelli, TJW Lazio, and Rutger van Haasteren.
Are we there yet? time to detection of nanohertz gravitational waves based on pulsar-timing array limits.
The Astrophysical Journal Letters, 819(1):L6, 2016.

Eric Thrane, Stefan Ballmer, Joseph D Romano, Sanjit Mitra, Dipongkar Talukder, Sukanta Bose, and Vuk Mandic.
Probing the anisotropies of a stochastic gravitational-wave background using a network of ground-based laser interferometers.
Physical Review D, 80(12):122002, 2009.

Eric Thrane, Vuk Mandic, and Nelson Christensen.
Detecting very long-lived gravitational-wave transients lasting hours to weeks.
Physical Review D, 91(10):104021, 2015a.

Eric Thrane, Sanjit Mitra, Nelson Christensen, Vuk Mandic, and Anirban Ain.
All-sky, narrowband, gravitational-wave radiometry with folded data.
Physical Review D, 91(12):124012, 2015b.

Caterina Tiburzi, George Hobbs, Matthew Kerr, WA Coles, Shi Dai, RN Manchester, Andrea Possenti, RM Shannon, and XP You.
A study of spatial correlations in pulsar timing array data.
Monthly Notices of The Royal Astronomical Society, 455(4):4339–4350, 2016.

Caterina Tiburzi, JPW Verbiest, GM Shaifullah, GH Janssen, JM Anderson, A Horneffer, Jörn Künsemöller, S Osłowski, JY Donner, M Kramer, et al.
On the usefulness of existing solar wind models for pulsar timing corrections.
Monthly Notices of the Royal Astronomical Society, 487(1):394–408, 2019.

AN Timokhin.
Time-dependent pair cascades in magnetospheres of neutron stars–i. dynamics of the polar cap cascade with no particle supply from the neutron star surface.
Monthly Notices of the Royal Astronomical Society, 408(4):2092–2114, 2010.

Richard C Tolman.
Static solutions of einstein's field equations for spheres of fluid.
Physical Review, 55(4):364, 1939.

Greg Ushomirsky.
R-modes in accreting and young neutron stars.
In *AIP Conference Proceedings*, volume 575, pages 284–295. American Institute of Physics, 2001.

M. Vallisneri.
Libstempo.
https://github.com/vallis/libstempo/, 2013.

M Vallisneri, SR Taylor, J Simon, WM Folkner, RS Park, C Cutler, JA Ellis, TJW Lazio, SJ Vigeland, K Aggarwal, et al.
Modeling the uncertainties of solar-system ephemerides for robust gravitational-wave searches with pulsar timing arrays.
arXiv preprint arXiv:2001.00595, 2020.

S van der Putten, HJ Bulten, JFJ van den Brand, and M Holtrop.
Searching for gravitational waves from pulsars in binary systems: An all-sky search.
In *Journal of Physics: Conference Series*, volume 228, page 012005. IOP Publishing, 2010.

CA Van Eysden and A Melatos.
Pulsar glitch recovery and the superfluidity coefficients of bulk nuclear matter.
Monthly Notices of the Royal Astronomical Society, 409(3):1253–1268, 2010.

Rutger van Haasteren and Yuri Levin.
Understanding and analysing time-correlated stochastic signals in pulsar timing.
Monthly Notices of the Royal Astronomical Society, 428(2):1147–1159, 2013.

Rutger van Haasteren and Michele Vallisneri.
New advances in the gaussian-process approach to pulsar-timing data analysis.
Physical Review D, 90(10):104012, 2014.

Rutger Van Haasteren, Yuri Levin, Patrick McDonald, and Tingting Lu.
On measuring the gravitational-wave background using pulsar timing arrays.
Monthly Notices of the Royal Astronomical Society, 395(2):1005–1014, 2009.

W Van Straten.
High-fidelity radio astronomical polarimetry using a millisecond pulsar as a polarized reference source.
The Astrophysical Journal Supplement Series, 204(1):13, 2013.

JPW Verbiest, L Lentati, G Hobbs, Rutger van Haasteren, Paul B Demorest, GH Janssen, J-B Wang, G Desvignes, RN Caballero, MJ Keith, et al.
The international pulsar timing array: first data release.

Monthly Notices of the Royal Astronomical Society, 458(2):1267–1288, 2016.

Daniele Viganò and Jose A Pons.
Central compact objects and the hidden magnetic field scenario.
Monthly Notices of the Royal Astronomical Society, 425(4):2487–2492, 2012.

M Vigelius and A Melatos.
Improved estimate of the detectability of gravitational radiation from a magnetically confined mountain on an accreting neutron star.
Monthly Notices of the Royal Astronomical Society, 395(4):1972–1984, 2009.

Alexander Vilenkin, Yuri Levin, and Andrei Gruzinov.
Cosmic strings and primordial black holes.
Journal of Cosmology and Astroparticle Physics, 2018(11):008, 2018.

Robert V Wagoner.
Gravitational radiation from accreting neutron stars.
The Astrophysical Journal, 278:345–348, 1984.

Karl Wette.
Parameter-space metric for all-sky semicoherent searches for gravitational-wave pulsars.
Physical Review D, 92(8):082003, 2015.

Karl Wette, BJ Owen, B Allen, Michael Ashley, J Betzwieser, N Christensen, TD Creighton, V Dergachev, I Gholami, E Goetz, et al.
Searching for gravitational waves from cassiopeia a with ligo.
Classical and Quantum Gravity, 25(23):235011, 2008.

L Woltjer.
X-rays and type i supernova remnants.
The Astrophysical Journal, 140:1309–1313, 1964.

XP You, GB Hobbs, WA Coles, RN Manchester, and JL Han.
An improved solar wind electron density model for pulsar timing.
The Astrophysical Journal, 671(1):907, 2007.

Bing Zhang, Alice K Harding, and Alexander G Muslimov.
Radio pulsar death line revisited: Is psr j2144–3933 anomalous?
The Astrophysical Journal Letters, 531(2):L135, 2000.

WW Zhu, IH Stairs, PB Demorest, David J Nice, JA Ellis, SM Ransom, Z Arzoumanian, K Crowter, T Dolch, RD Ferdman, et al.
Testing theories of gravitation using 21-year timing of pulsar binary j1713+ 0747.
The Astrophysical Journal, 809(1):41, 2015.

Xing-Jiang Zhu, Weiguang Cui, and Eric Thrane.
The minimum and maximum gravitational-wave background from supermassive binary black holes.
Monthly Notices of the Royal Astronomical Society, 482(2):2588–2596, 2019.

Aaron Zimmerman, Carl-Johan Haster, and Katerina Chatziioannou.
On combining information from multiple gravitational wave sources.
Physical Review D, 99(12):124044, 2019.